INTRODUCTION TO CRITICAL STRAIN AND A NEW METHOD FOR THE ASSESSMENT OF MECHANICAL DAMAGE IN STEEL LINE PIPE

A Thesis

by

RYAN DANIEL MILLIGAN

Submitted to the Office of Graduate Studies of
Texas A&M University
in partial fulfillment of the requirements for the degree of

MASTER OF SCIENCE

Chair of Committee,	Peter B. Keating
Committee Members,	Gary Fry
	Alan B. Palazzolo
Head of Department,	Robin Autenrieth

August 2013

Major Subject: Civil Engineering

ABSTRACT

The pipeline industry has conducted a vast amount of research on the subject of mechanical damage. Mechanical damage makes up a large portion of the total amount of pipeline failures that occur each year. The current methods rely on engineering judgment and experience rather than scientific theory. The method for the assessment of mechanical damage introduced in this study uses a material property called critical strain to predict the onset of cracking within the pipe wall. The critical strain is compared to the strain within a dent using a ductile failure damage indicator (DFDI).

To investigate the use of the DFDI to indicate the onset of cracking within a dent, the study attempted to accomplish three tasks. The first was to investigate the use of various techniques to locate the critical strain from the stress-strain curve. Five samples taken from the pipe material was used to generate both engineering and true stress-strain curves. A sensitivity analysis was conducted to show the effects of different variables on the critical strain value.

The DFDI compares the critical strain value to the calculated strain at the deepest depth location within a dent. The strain calculations use the curvature of the dent and thus require a dent profile. A high resolution laser scanner was used to extract dent profiles from a pipe. The second task of the study was to investigate the reliability of the laser scanner equipment used for this study. The results from the investigation showed that the laser scanner could be used to scan the inside of the pipe despite its design for external scanning. The results also showed that the scans should be 1 mm in length along the axis of the pipe at a resolution of 0.5 mm and 360 degrees around the pipe.

The final task was to conduct the denting test. The test used a spherical indenter to dent the pipe at increments of 3% of the outside diameter. The results from the test showed that a visible crack did not form on the inside pipe surface as expected from the DFDI method. This does not mean a crack did not form. During the denting test distinct popping sounds were observed possibly indicating cracks forming within the pipe wall.

DEDICATION

I would like to dedicate this thesis to my family. Without which I never would have succeeded. It was with their support and dedication that made all that I have accomplished possible. I dedicate this thesis to my mother, whose love and persistence kept me focused on my studies, to my father, whose advice and guidance always directed me on the right path, and to my sister, whose love and humor always brightened my days. I also dedicate this thesis to my Nana and Aunt Pappy, for whom words cannot express the amount of gratitude for their unconditional love and support. This thesis is also dedicated to the memory of my Great Grandmother Lanorma Richardson, my Grandmother Phillis Milligan, my Aunt Jean Rouget, and my Uncles Mike Milligan, Charlie Rouget, and Jimmy Rouget.

ACKNOWLEDGMENTS

It is with immense gratitude that I acknowledge my Professor Dr. Peter Keating for all his help and support provided during graduate school. I am also grateful for the opportunity to work in the High Bay Laboratory, a very unique and rewarding experience. I would also like to thank Matt Potter and Ramiro Vonoye for all their assistance and guidance. I learned a great deal while working under their supervision. Finally, I would like to thank the engineers at Blade Energy Partners for the opportunity to work on their project. I would like to give special thanks to Udayasankar Arumugam who provided guidance and direction while writing this thesis

.

TABLE OF CONTENTS

LIST OF FIGURES

Page

LIST OF TABLES

Page

1 INTRODUCTION

1.1 Background

Mechanical damage is one of the major causes of delayed failures in gas transmission pipelines. Current methods used to analyze and assess the structural integrity of damaged pipelines are based primarily on engineering judgment rather than scientific theory. These methods make it possible to improperly assess a damaged pipe, possibly resulting in failure. The pipeline industry can benefit from an integrity assessment method that is easily applied and accurate. Such a method could save money from unnecessary repairs and save lives from delayed failures.

In 2009, a report compiled by Baker was submitted to the DOT Research and Special Programs Administration on mechanical damage of oil and gas pipelines (Baker 2009). The goal of the research was to compile data from various resources in an effort to summarize current assessment, analysis, prevention, and repair techniques for transmission pipelines. The report compiled failure data from 1988 to 2008. Figures 1-3 show the distribution of causes that led to a significant incident in various types of pipelines.

According to Baker, a significant incident is one that results in injury requiring hospitalization or loss of life. The figures show that excavation damage was typically the number one cause of significant incidents from 2000 to 2008. This type of damage is typically caused by the equipment used for excavation, such as the tooth from an excavation bucket. The resulting damage is an unconstrained plain dent similar to that shown in Figure 4. The only category to have a higher percentage was “Other Causes” which includes all incidents caused by unknown factors. Due to the significance of mechanical damage to pipeline failures, much research has been conducted to better assess the influence of dents as it pertains to the burst strength of pipes. This study will focus primarily on dents caused by indentors such as rocks or excavators.

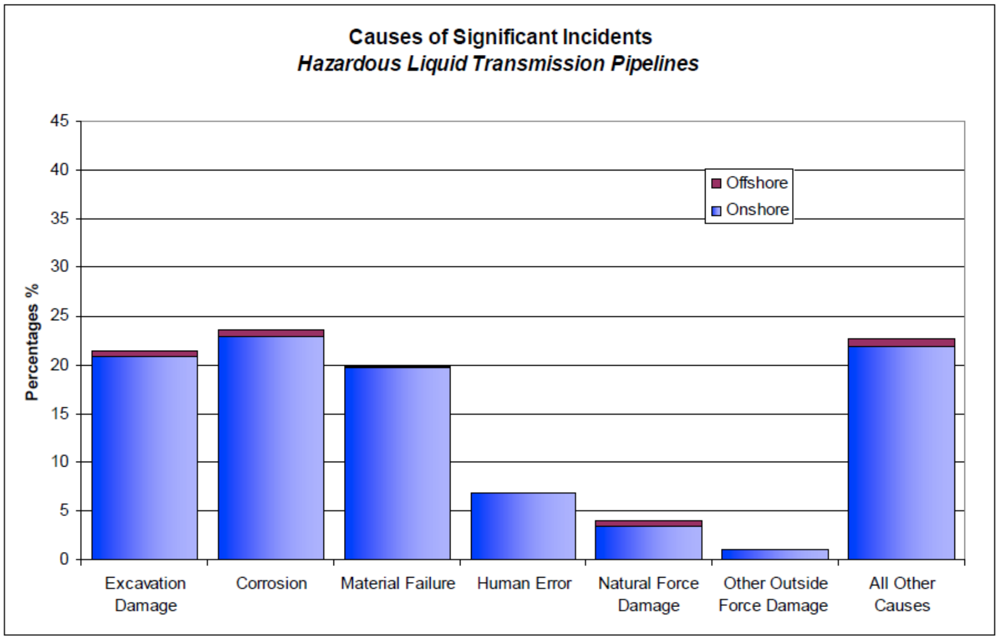

Figure 1: Causes of Significant Pipeline Incidents on Hazardous Liquid Transmission Pipelines from 1988-2008 (Baker 2009)

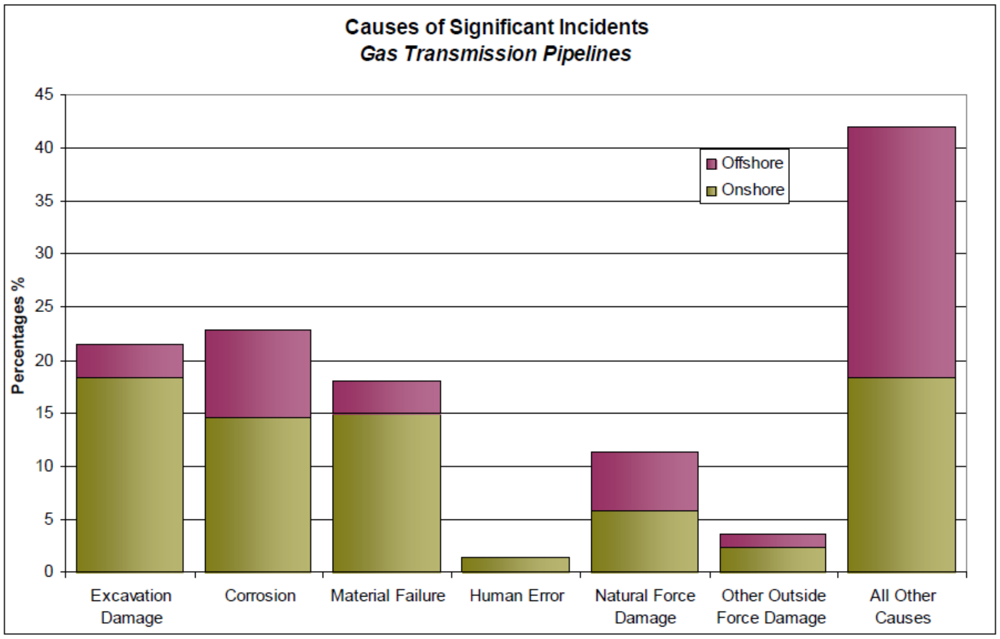

Figure 2: Causes of Significant Pipeline Incident on Hazardous Gas Transmission Pipelines from 1988-2008 (Baker 2009)

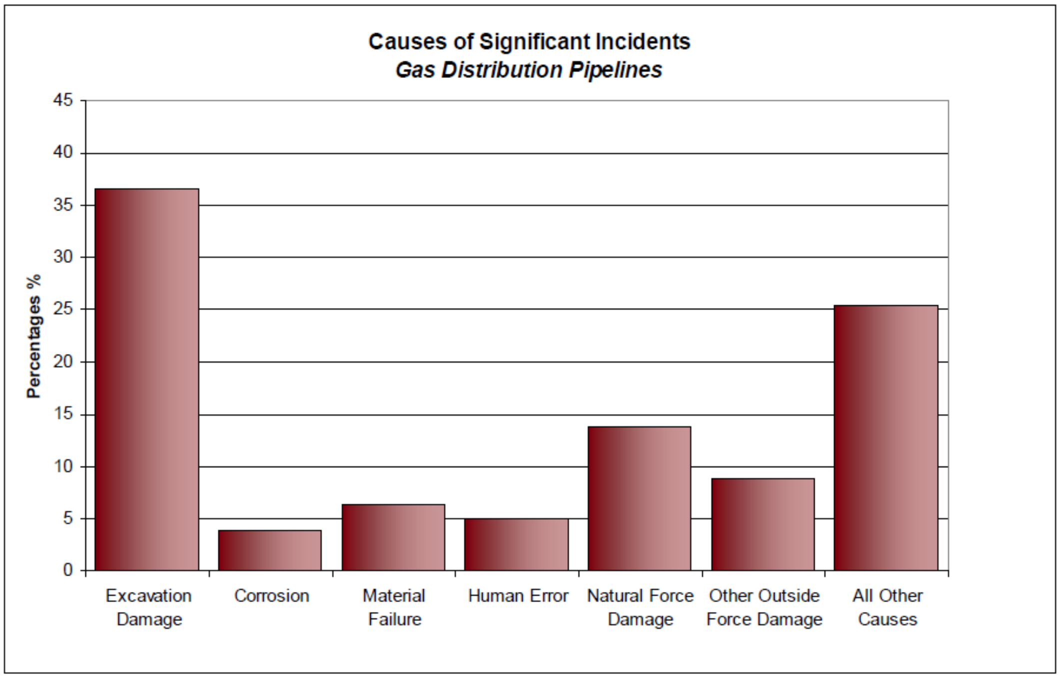

Figure 3: Causes of Significant Pipeline Incident on Hazardous Gas Distribution Pipelines from 1988-2008 (Baker 2009)

Figure 4: Plain dent

Table 1 shows the categories typically used to describe mechanical damage. Rerounding or spring back is the effect describing what happens after an indenter, such as a backhoe tooth, is removed. It can be observed that the pipe will attempt to return to its original shape. There are several methods used by different organizations to assess the severity of the damage. Table 2 is a list of the current methods used for assessment. Due to the complexities of gouges and secondary defects, the focus of this research is on plain dents. Figure 5 is an image of a dent with a gouge. This type of damage occurs when equipment impacts a pipe and scrapes across the surface causing plastic flow and a localized reduced wall thickness.

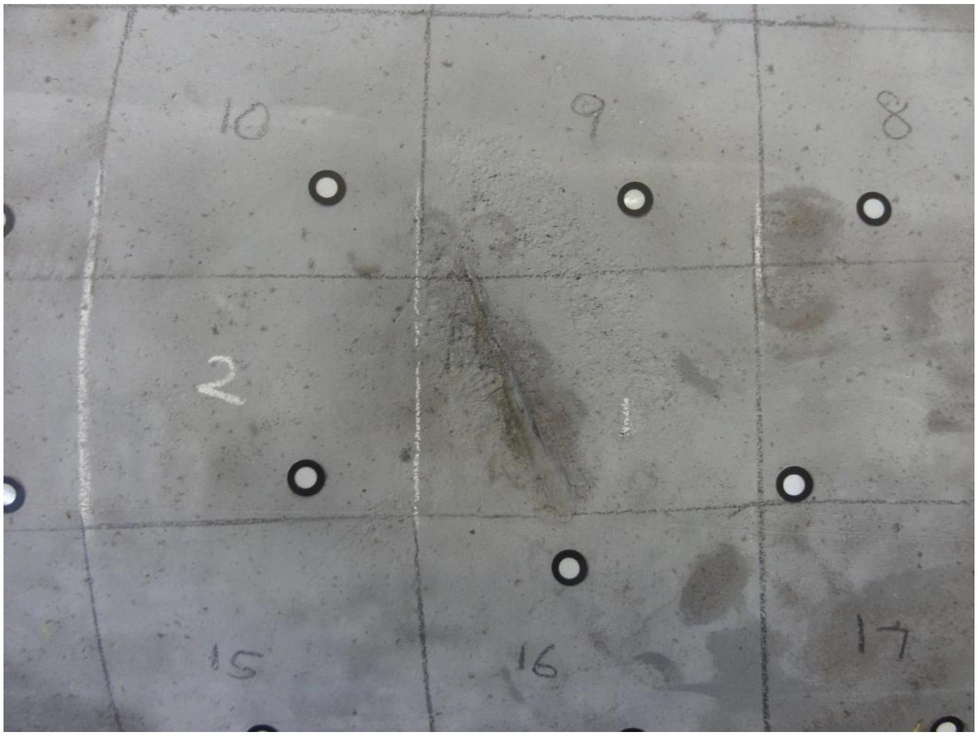

Figure 5: Dent with a Gouge

Table 1: Dent Categories

Dent Category	Description
Smooth or Plain	Dent which causes a smooth change in curvature
Unconstrained	Dent that is allowed to reround
Constrained	Dent is restrained from rerounding
Complex	Dent with a gauge, groove, stress riser, or other secondary defect

Table 2: Recommended Methods for Assessing the Burst Strength and Fatigue Life of Mechanical Damage Defects (Cosham and Hopkins 2003)

Damage Type	Internal pressure (static) longitudinally oriented	Internal pressure (fatigue)
Gouges	NG-18 equations, PAFFC; BS 7910 or API 579	BS 7910 or API 579
Plain dents	Dent depth less than 7 or 10 percent of pipe diameter (empirical limit)	EPRG
Kinked dents	No method	
Smooth dents on welds	No method	No method (empirical limits)
Smooth dents and gouges	Dent-gouge fracture model	No method (empirical limits)
Smooth dents and other types of defect	Dent-gouge fracture model	No method

Table 2 shows that the criteria for plain dent assessments are based on empirical limits. These limits come from the idea that plain dents have no effect on burst strength unless they are significantly deep. Tests compiled from various agencies from 1958 to 2004 verify this assumption (Cosham and Hopkins 2003). Figure 6 shows the results of the burst tests. Of the 75 tests conducted, only 4 failed at the location of the dent. Dents as deep as 15% of the outside diameter experienced little effect on burst strength. Organizations such as ASME, EPRG, PDMA, and British Gas have come up with different depth limits based on this data. The discrepancy between each organization on depth limits is an indication as to the validity of the current damage assessment method.

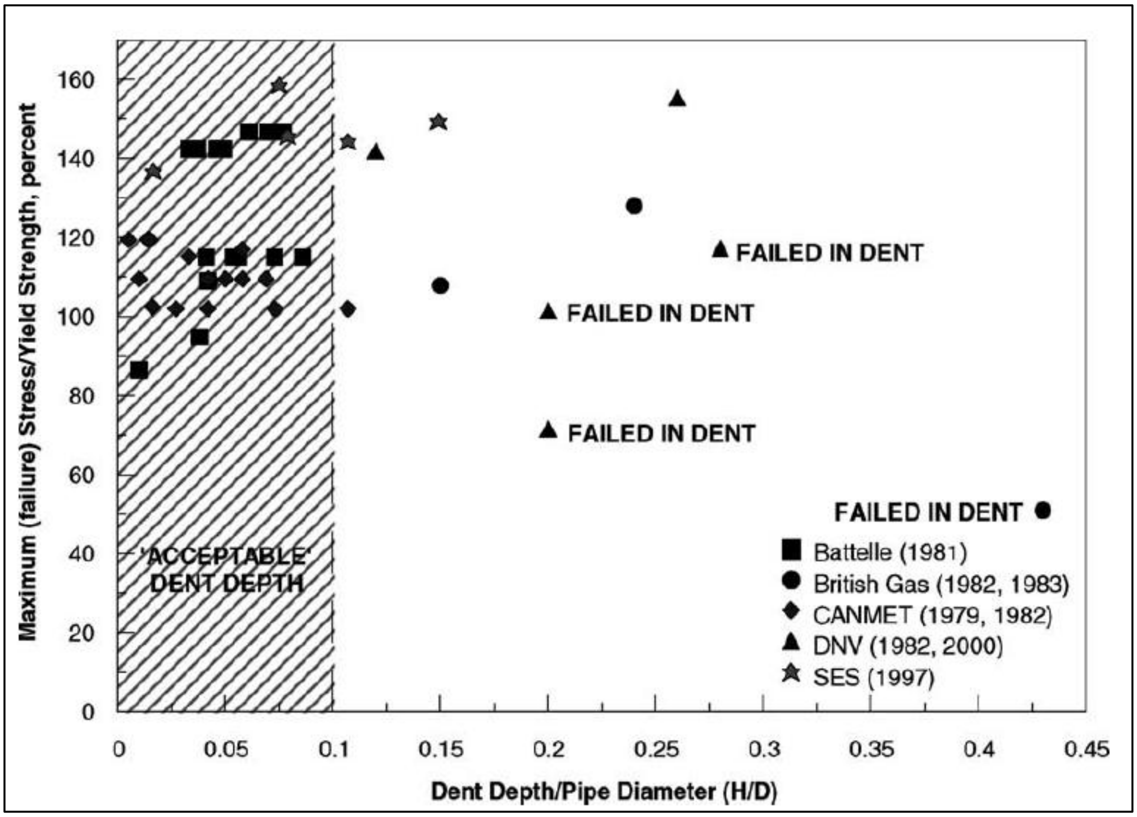

Figure 6: Maximum Stress of Plain Dents (Cosham and Hopkins 2003)

Depth is not the only factor that characterizes the degree of mechanical damage within a dent. The geometry of the dent has a significant effect on the dent strain. For example, a short dent experiences higher strains than a long dent with a similar depth. This is why organizations such as ASME have developed strain based equations for integrity assessment. ASME B31.8 uses a 6% strain limit based on limited data and engineering judgement. ASME B31.8 also offers non-mandatory equations for strain (Noronha et al. 2010). Due to the complexity of dents, no standard strain equations exist (Gao et al. 2008). Equations 1-4 are the current equations used by ASME to calculate strain. ε_1, ε_2, and ε_3 correspond to the circumferential bending strain, longitudinal bending strain, and extensional strain respectively.

$$\epsilon_1 = \frac{t}{2}\left(\frac{1}{R_o} - \frac{1}{R_1}\right) \qquad 1$$

$$\epsilon_2 = -\frac{t}{2R_2} \qquad 2$$

$$\epsilon_3 = \frac{1}{2}\left(\frac{d}{L}\right)^2 \qquad 3$$

$$\epsilon_{eff} = \sqrt{\epsilon_x^2 - \epsilon_x\epsilon_y + \epsilon_y^2} \qquad 4$$

Equations 1-3 were developed using the results from a strain analysis on a thin plate and empirically established from a limited number of tests. There is no record in the public domain explaining how the equation for effective strain was established (Gao et al. 2008). By substituting equations 1-3 into equation 4 leads to the equations for strain in the interior and exterior walls of the pipe. Equations 5 and 6 are the results for the interior and exterior strains after substitution.

$$\epsilon_{\mathrm{i}} = \sqrt{\epsilon_1^2 - \epsilon_1(\epsilon_2 + \epsilon_3) + (\epsilon_2 + \epsilon_3)^2} \tag*{5}$$

$$\epsilon_{\mathrm{o}} = \sqrt{\epsilon_1^2 + \epsilon_1(-\epsilon_2 + \epsilon_3) + (-\epsilon_2 + \epsilon_3)^2} \tag*{6}$$

As seen in the above equations, dent strain depends on dent depth, length, wall thickness, and radius of curvature. Of these variables, radius of curvature is the most difficult to calculate from a dent profile. There has been much development in the techniques and equations used to calculate the radius of curvature. The methods have been incorporated into the current systems used to inspect pipelines. Pipeline operators use a tool called a pipeline inspection gauge (PIG) to inspect the pipeline geometry. Figure 7 is an image of a typical PIG. PIGs have caliper-like devices that run along the circumference of the tool. The PIG is placed into a pipeline and advanced by gas pressure. As the device moves along the pipe it reads any deviation of the pipe wall from the undeformed wall location. GPS units on the PIGs allow operators to locate detected dents.

Data from a PIG along with interpolation techniques are used to find the radius of curvature within a dent. Various papers offer different methods of interpolating the data such as B-Splines (Noronha et al. 2010) and the oscillating circle method (Rosenfeld 1998). The interpolation techniques are used to find the derivatives of the displacement data. These derivatives are then used to find the radius of curvature by substituting into Equation 7.

$$\mathrm{R} = \frac{\left(\left(\frac{\mathrm{dx}}{\mathrm{dy}}\right)^2 + \left(\frac{\mathrm{dy}}{\mathrm{dt}}\right)^2\right)^{\frac{3}{2}}}{\frac{\mathrm{dx}}{\mathrm{dy}}\frac{\mathrm{d}^2\mathrm{y}}{\mathrm{dt}^2} - \frac{\mathrm{dy}}{\mathrm{dt}}\,\frac{\mathrm{d}^2\mathrm{x}}{\mathrm{dt}^2}} \tag*{7}$$

Figure 7: Pipeline Inspect Gauge (PIG) (Scott 2011)

Once the radius of curvature is known the strains are calculated using equations 1-4 from ASME B31.8. The calculated strains are then compared to the strain limit provided by the governing agency. This research introduces a new method of mechanical damage assessment proposed by Blade Energy Partners. The method attempts to use a damage indicator to predict the onset of cracking within the pipe wall. At this point the pipe is declared unacceptable and is either repaired or removed from service. The damage indicator is based on a material property called critical strain.

1.2 Research Objectives

Since the review of the pipeline industry written by Baker, much research has been done on the subject of mechanical damage. More specifically, research on plain dents. This has led to the research organized by Blade Energy Partners regarding the subject of critical strain and the mechanical damage indicator. A denting test has been designed to validate the new method. The main objectives of this research are to review the sensitivity of the critical strain calculations and validate the use of laser equipment for the denting test procedure. The scope of this research will also include an introduction to the denting test. The research will attempt to complete three tasks. The first is to assess the method used to calculate critical strain within line pipe. This includes an assessment of sensitivity of the critical strain value to the amount of data trimming and to different calculation techniques. The second goal is to review the laser equipment used to obtain dent profiles. This includes the effects of resolution selection and amount of scanning to the maximum depth value. The final goal is to review the denting test and validate the findings.

2 FRACTURE MECHANICS

2.1 Introduction

During World War II, the United States supplied ships and airplanes to Great Britain. The German Navy was destroying the British cargo ships at a substantial rate. To meet the high demand of cargo ships, a United States construction engineer named Henry Kaiser developed a new ship-building procedure. The process used welded rather than riveted construction, a popular method at that time. The ships were given the name Liberty ships. In 1943, one of the ships broke completely in two while sailing between Siberia and Alaska. Additional fractures later occurred in other Liberty ships.

The Liberty ship program constructed around 2,700 vessels. Approximately 400 sustained fractures, of which 90 were considered serious. 20 vessels experienced total failure while around half of those were ships that broke in two halves. The failures occurred due to the propagation of a crack that began at a corner of a square deck opening. This event sparked the naval Research Laboratory in Washington D.C. to study this particular problem. This marked the beginning of a more aggressive study in the field of fracture mechanics. (Anderson 1995)

Fracture mechanics is formally defined as the study of the formation of cracks in materials. These cracks can potentially lead to failure at a stress lower than the materials ultimate strength. Like the Liberty ships, this type of failure can be unexpected and catastrophic. Failure is typically classified as brittle or ductile. Brittle fracture is characterized as low energy absorption and small deformation prior to failure. Ductile fracture is capable of absorbing more energy and sustains significant deformation prior to failure. Metals that experience ductile fracture fail due to the nucleation, growth and coalescence of micro voids.

2.2 Ductile Failure

Constance Tipper was the lead investigator of the Liberty ships. She was also the first to suggest that fracture of single-phase ductile metals originates from non-metallic inclusions within the microstructure. It is well establish from previous research that ductile fracture occurs by the nucleation, growth, and coalescence of voids within the microstructure (Argon et al. 1975; Goods and Brown 1978; McClintock et al. 1966; Puttick 1959; Rogers 1960).

The significance of second phase particles and inclusions was studied by Rosenfield (1968) and Broek (1973). Rosenfield (1968) concluded that the source of void nucleation was at the matrix/particle interface at second phase particles. He determined that flaws, like those suggested by Griffith (1921), were the exception rather than the norm regarding the initiation site of voids. Similarly, Broek used electron microscopical examination procedures to study the micro-structure of thirteen different aluminum alloys. Broek (1973) observed that large inclusions influenced the strain of the micro-structure, but was not essential to the fracture process. Figure 8 is an image of void nucleation at large inclusions shown under an optical microscope. He suggested that small inclusions were the main factor based on comparisons between measurements of inclusion spacing and dimple size. It has been shown that large inclusions form voids by cracking of the inclusion particle, whereas small inclusions form voids by particle-matrix decohesion.

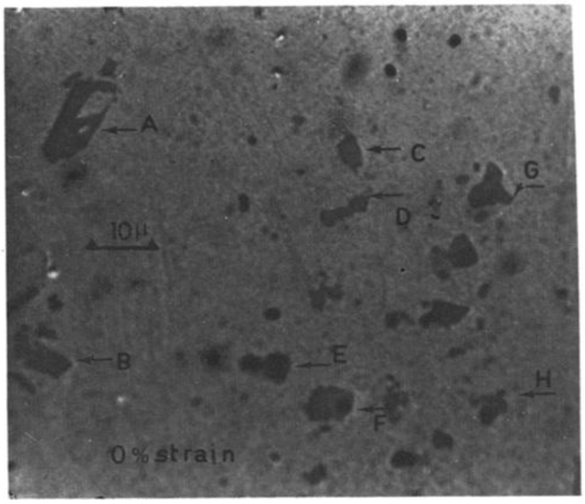

Figure 8: Void Nucleation at Large Particles (Broek 1973)

Rogers (1960) attempted to consolidate previous research to provide a more unified understanding of tensile fracture in metals. He varied different variables associated with ductile fracture to observe the effect on the microstructure of metals. Rogers observed that voids nucleated on boundaries both parallel and normal to the tensile axis. The voids in the transverse direction began at much smaller strain levels. These voids would grow due to the tensile stress. The growth of the voids caused stress concentrations near the tip of the larger voids. This would nucleate more voids near the stress concentration and eventually grow into the larger void, thus perpetuating the extension of the crack.

Rogers (1960) also noticed severe shear deformation, shown in Figure 9, at angles 30 to 40 degrees to the tensile axis. He suggested that the shear bands he observed caused a large amount of voids to nucleate. These “void sheets” weakened the local area until one of the bands failed. This would extend the crack a finite amount outside the plane of minimum cross section. The crack, now static, would form more void sheets. The sheets would fail again but rather than away from the minimum cross section, it would propagate back into the minimum cross section. This explains the typical chevron pattern seen on failure surfaces.

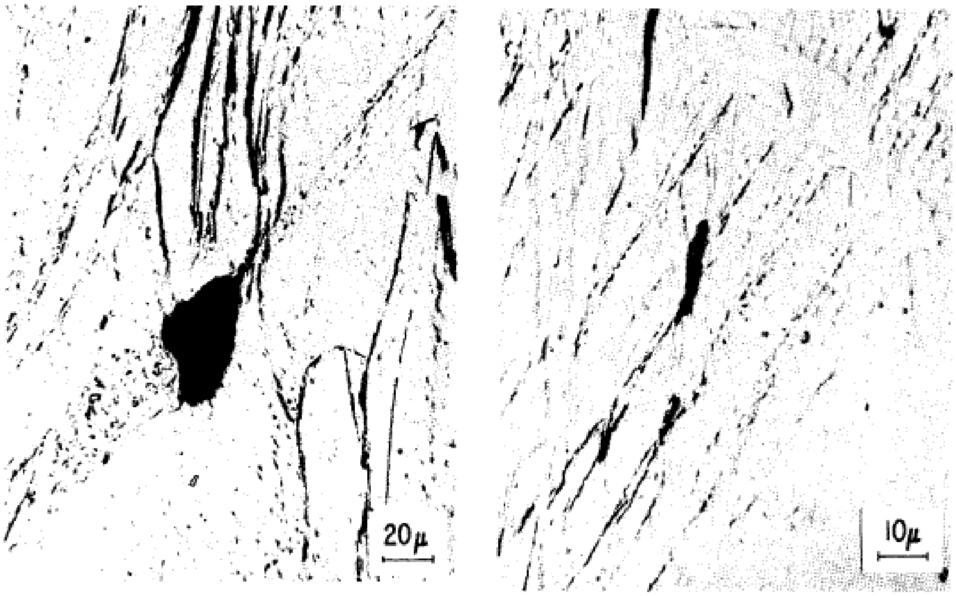

Figure 9: Examples of Shear Bands (Rogers 1960)

This particular mechanism of fracture is only one part of the final failure in ductile materials. The second part is described by Rogers as “alternating slip” or by Crussard as “ductile cleavage”. The process is not fracture by definition, but rather a slipping off of the material due to large plastic deformation. Bridgman (1964), in a series of experiments testing the effect of hydrostatic pressure on tensile tests, found that the specimens could nearly reach 100 percent reduction in cross sectional area if high hydrostatic pressures were applied. It has been suggested that the mechanism of failure is a balance between slip and fracture. The hydrostatic pressure reduces the growth of voids and thus shifts the failure mechanism from void nucleation and growth to slip.

Research conducted by Hancock and Mackenzie (1975) found that ductility depends markedly on both the orientation of the stress system with respect to rolling direction and the tri-axiality of the stress-state. Hancock and Mackenzie tested notched specimens taken from a rolled plate. These specimens were taken from the long transverse and short transverse direction as shown in Figure 10. They found that failure initiation in the short transverse direction was caused by the connection of large voids by microcracks as seen in Figure 11. However, in the long transvers direction failure was initiated by the coalescence of large voids as shown in Figure 12. The most important observation made by Hancock and Mackenzie is that the tri-axiality of the stress state increases as the ductility decreases.

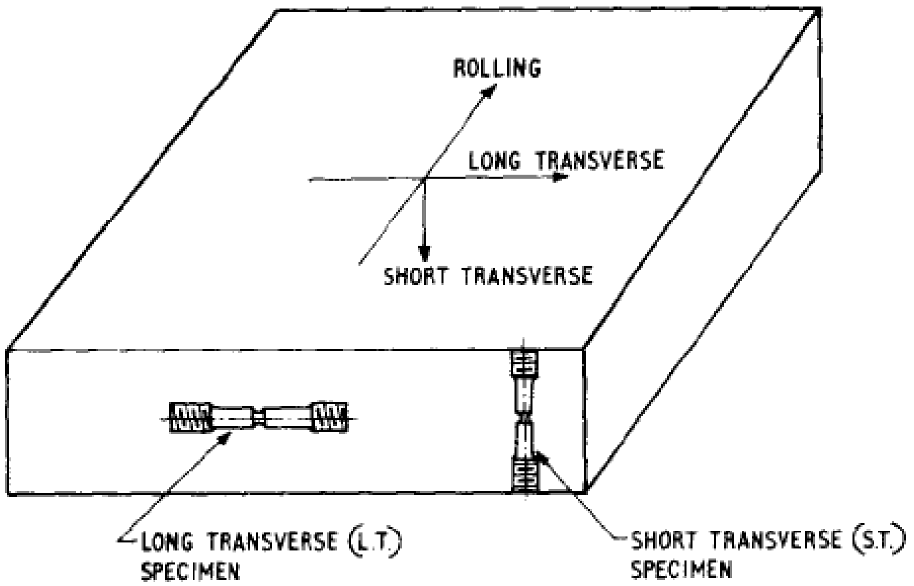

Figure 10: Test Specimen Locations for Hancock and Mackenzie Experiments

The ultimate goal for many researchers is to develop a viable model for ductile failure. This model should include failure criteria that are based on a global parameter such as stress or strain. Hancock and Mackenzie suggest using a failure strain as the limiting criteria for ductile fracture. This critical strain can then be used to assess the damage created in dented pipelines. Based on the previous discussion, failure is initiated once a crack has formed within the material. From that point on, the crack will propagate until total failure occurs. The formation of a crack is evidence of incipient failure and is a good criterion for integrity assessment of pipelines. The challenge is to develop a mathematical model that incorporates material properties and complicated stress states.

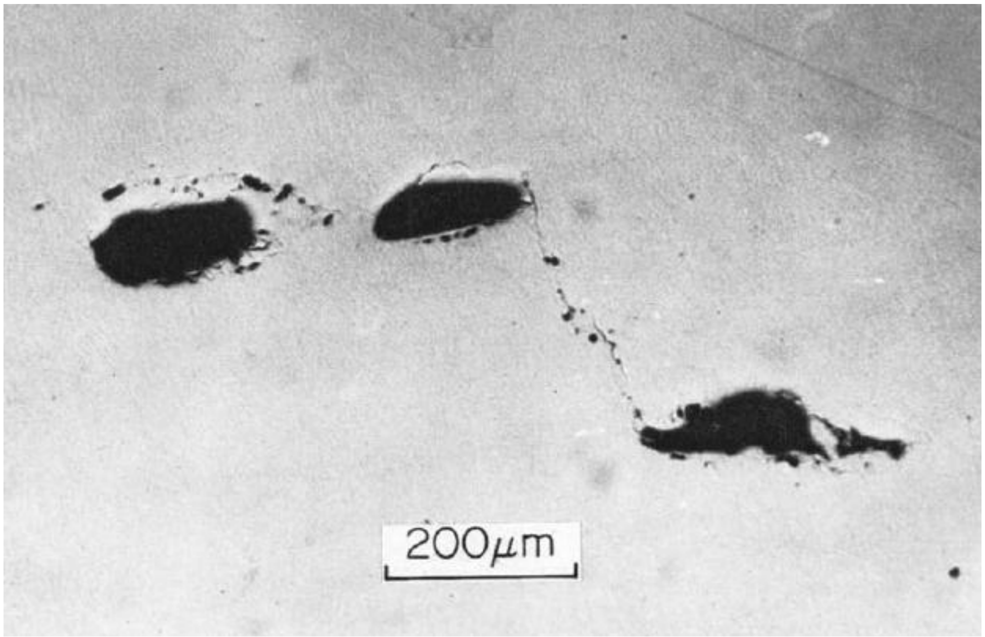

Figure 11: Failure Initiation in the Short Transverse Direction (Hancock and Mackenzie 1975)

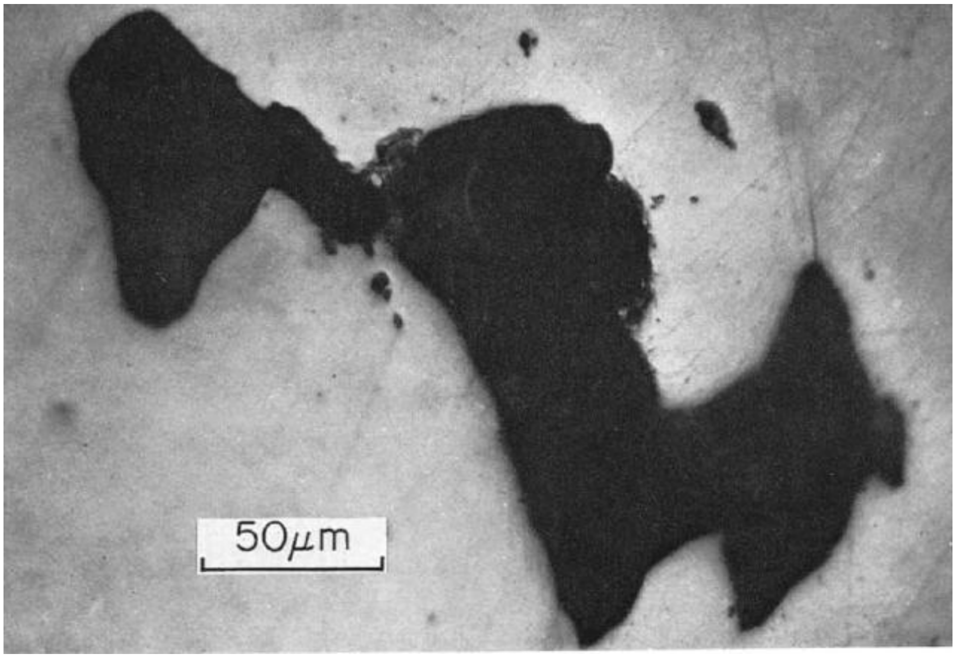

Figure 12: Failure Initiation in the Long Transverse Direction (Hancock and Mackenzie 1975)

2.3 Fracture Models

It is well established that ductile fracture occurs by the nucleation, growth, and coalescence of voids as discussed in the previous section. This has led to the development of several mathematical models describing the failure of ductile materials. These models include the work done by McClintock (1968) as well as Rice and Tracey (1969). These models have been used extensively in the study of ductile fractures. They are also utilized in the research conducted by Blade on pipeline dent assessments.

2.3.1 McClintock (1968)

Research conducted by Rhine showed similarities between the growth of voids in copper and plasticine. Rhine used polystyrene spheres to simulate the effects of inclusions. Fracture occurred between voids when the inclusion density was high. The similarities between the void growth of plasticine and copper convinced McClintock that ductile fracture was a continuum mechanics problem. Other theories on ductile failure existed at the time but many neglected the effects of triaxiality.

McClintock's model consisted of an elliptical hole in a cylindrical cell. The cell dimensions were on the order of the mean spacing of the holes. The holes were assumed not to interact and thus were analyzed as if in an infinite medium. Ductile failure was assumed to occur when one of the axes of the hole grew to a pair of cell walls. McClintock first developed equations for the fractional increment in hole diameter for circular holes in both a Mises and Tresca material. He then used known solutions for elliptical holes in a viscous material to develop equations for eccentricity and mean radius. Finally, he extrapolated the equations for elliptical holes in a plastic material and accounted for the possibility of strain hardening. The results are shown in equations 8 and 9.

$$\ln\frac{R}{R_0}=\frac{\bar{\epsilon}\sqrt{3}}{2(1-n)}\sinh\left(\frac{\sqrt{3}(1-n)}{2}\frac{(\sigma_a+\sigma_b)}{\bar{\sigma}}\ \frac{(\epsilon_a+\ \epsilon_b)}{2}\right) \tag{8}$$

$$m=\frac{(\sigma_a-\sigma_b)}{(\sigma_a+\sigma_b)}+\left(m^0-\frac{(\sigma_a-\sigma_b)}{(\sigma_a+\sigma_b)}\right)e^{\frac{\sqrt{3}\bar{\epsilon}}{(1-n)}\sinh\left(\frac{\sqrt{3}(1-n)}{2}\frac{(\sigma_a+\sigma_b)}{\bar{\sigma}}\right)} \tag{9}$$

2.3.2 *Rice and Tracey (1969)*

Rice and Tracey noted the work done by McClintock but sought out to develop a more realistic model. Their model consisted of a spherical void in a remotely uniform stress and strain field. The model approximates the solution for cavity expansion in an infinite rigid-plastic medium by employing a Rayleigh-Ritz procedure. The results showed that moderate and high stress triaxiality leads to an amplification of relative void growth rates over imposed strain rates by a factor depending exponentially on the mean normal stress (Rice and Tracey 1969). The results used for the dent damage model is shown below.

$$\frac{dR}{R}=0.28d\bar{\epsilon}^{p}\exp\left(\frac{3\sigma_m}{2\bar{\sigma}}\right) \tag{10}$$

2.4 Damage Mechanics

Damage mechanics attempts to simplify the complexities of modeling nucleation and growth of microvoids by taking a macroscopic approach to ductile fracture. A damage variable relates the density of defects such as microcracks and cavities to a failure criterion. Kachanov (1958) was the first to introduce a continuous variable related to the density of defects. Ductile failure by the process of void nucleation and growth is a discontinuous process. The use of damage variables provides a method of creating a process that is continuous. Damage is classified into three main types: ductile damage, fatigue damage, and creep damage. Similar to fracture mechanics models, damage mechanics assumes the material is isotropic. (Voyiadjis 2005)

Damage variables exist in two categories. The first category describes the amount of damage by the value of the variable. This category is typically defined in terms of stress, strain, or plastic strain energy. The second category describes the physical effects of damage. These are defined in terms of porosity, radius of cavities, or the relative area of micro-cracks and intersections of cavities. Many different damage indicators have been proposed in the past. The difficulty associated with fracture mechanics models and some damage models is that they are coupled. This has led to the implementation of “damage indicators” as defined by Fischer et al. (1995). Fischer notes that the evaluation of damage is performed for each increment of the elastic-plastic analysis of a structure. The uncoupling of the damage indicator allows for the analysis of a perfect structure. This also has the effect of limiting the prediction of the model to the initiation of a macrocrack.

3 CRITICAL STRAIN

3.1 Theory

Fischer et al. (1995) developed a method for calibrating a damage indicator to a standard tensile test, based on micromechanics models. Hancock and Mackenzie used work done by Rice and Tracey (spherical void) as well as McClintock (cylindrical void) to establish an equation defining a reference failure strain, ε_f. Hancock and Mackenzie suggest the use of Rice and Tracey's equation for the rate-of-change of the mean void radius R of a spherical hole in a rigid/non-hardening matrix (Equation 10). They assume that the failure strain is inversely proportional to hole growth-rate leading to Equation 11, where α is a material constant. The equation is calibrated using critical strain, ε_0, taken from a uniaxial tension test. Substituting values for σ_m and $\overline{\sigma}$ and solving for alpha gives $\alpha = 1.65\epsilon_0$. Substituting α into Equation 11 gives Equation 12.

$$\epsilon_f = \alpha \exp\left(-\frac{3\sigma_m}{2\overline{\sigma}}\right) \tag{11}$$

$$\epsilon_f = 1.65\epsilon_0 \exp\left(-\frac{3\sigma_m}{2\overline{\sigma}}\right) \tag{12}$$

The damage is now defined according to the above failure strain by

$$dD_i = \frac{d\epsilon_{pv}}{\epsilon_f} \tag{13}$$

And,

$$D_i = \int_0^{\epsilon_{pv}} \frac{\exp\left(\frac{3\sigma_m}{2\overline{\sigma}}\right)}{1.65\epsilon_0} d\epsilon_{pv} \tag{14}$$

When the above damage indicator is equal to or greater than 1 a crack has initiated in the material. An indicator less than 1 represents a crack free specimen. The important parameter in the above equations is critical strain, ε_0, which represents the point at which a crack forms in the necked region of a tensile specimen. This property represents the damage limit of the material and the transition from nucleation and growth of voids to crack propagation within a ductile material. Relating this property to a damage variable provides an effective and convenient method of modeling ductile fracture. Fischer et al. (1995) provides a method to calibrate critical strain using a load-displacement diagram of the material. As noted in the previous section, equation 5 is a simplified model used to describe ductile damage. Other models have been developed to improve the analyses in order to better correlate with experimental results. Fisher et al. (1995) suggest that the simplified model proposed by Hancock and Mackenzie is sufficient for most applications.

Various researchers have conducted experiments showing the strain at which the onset of cracking occurs. The difficulty with the research lies in the amount of data and effort required to find the strain associated with crack initiation. Research done by Tvergaard and Needlemen (1984) suggested that the point of crack initiation occurs at the sharp knee of the load-displacement curve shown in Figure 13 (Fischer et al. 1995). In some cases the load-displacement curve is smooth and does not contain a sharp knee. To study the smooth load-displacement curve, Fisher et. al. (1995) developed a simulation of a round bar tensile test. The numerical analysis, performed using ABAQUS, resulted in a numerical load-displacement curve and corresponding inclination curve as shown in Figure 14 and Figure 15 respectively. They concluded that the onset of a crack can be diagnosed either by the sharp knee in the load-displacement curve or by a second knee in the slope-displacement curve. The same knee can also be found in an engineering stress-strain curve based on the fact that both curves have the same shape. Once the critical strain is found from the engineer stress-strain curve or slope-strain curve, the true strain is calculated using the instantaneous diameter of the tensile specimen.

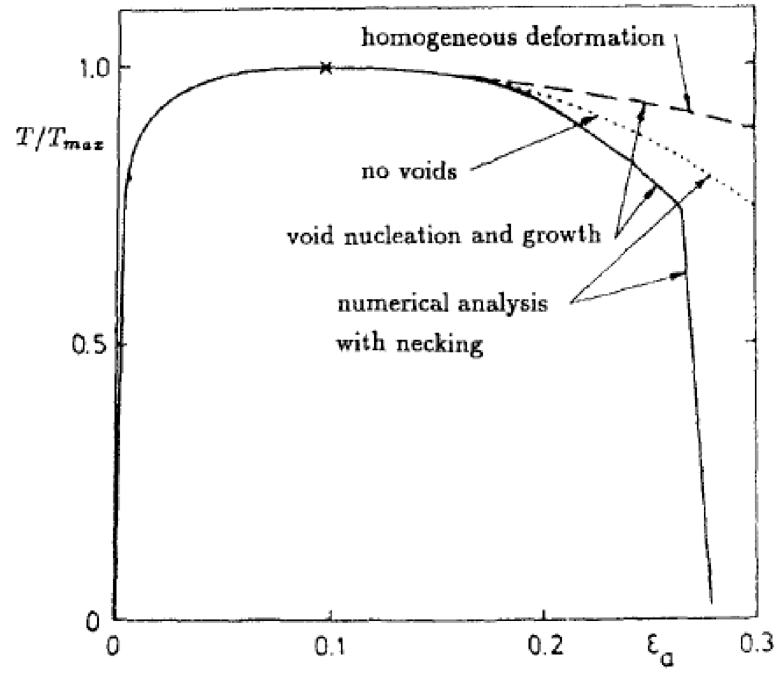

Figure 13: Relative Load-T/T_{max} vs. Logarithmic Strain ε_a (Tvergaard and Needleman 1984)

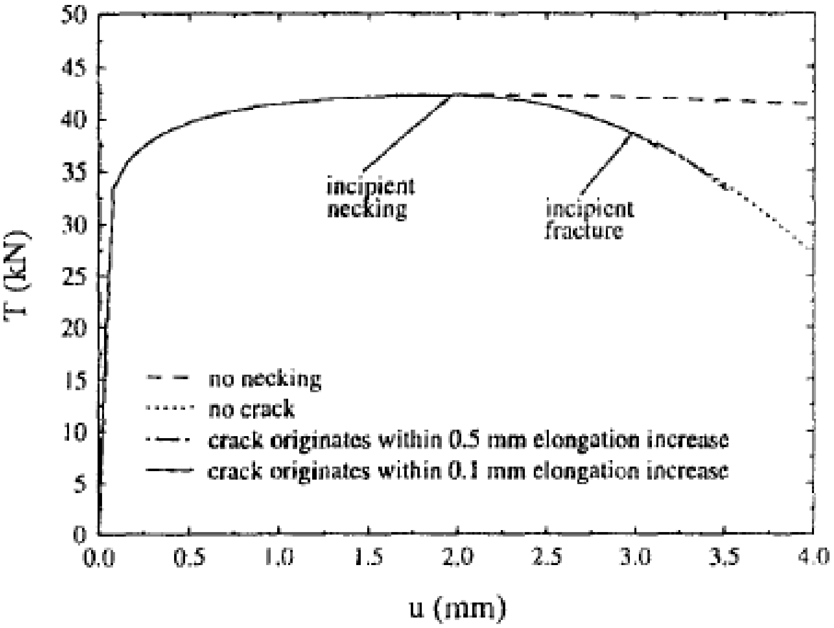

Figure 14: Load-Displacement Curve (Fischer et al. 1995)

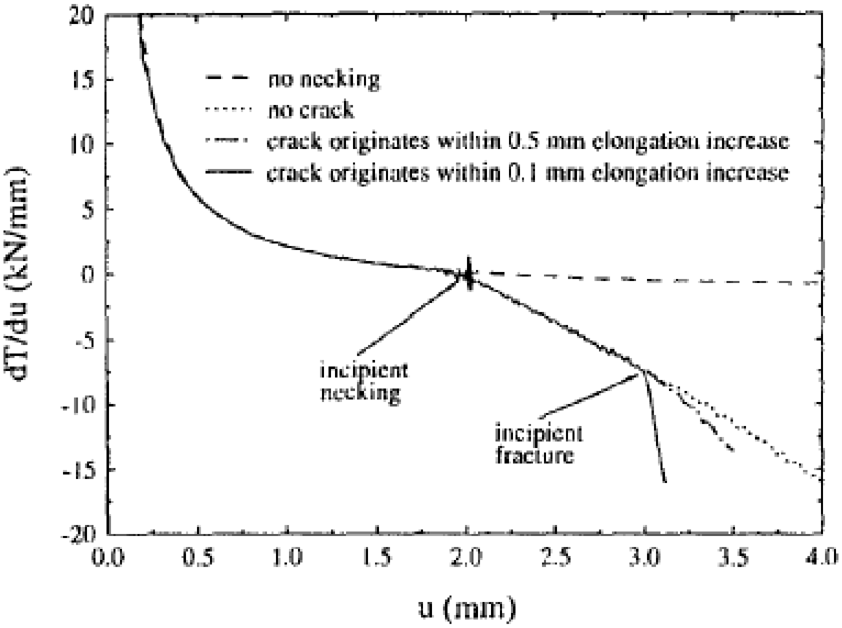

Figure 15 : Slope-Displacement Curve (Fischer et al. 1995)

3.2 Critical Strain Evaluation Process

The research done by Fischer et. al. (1995) has theoretically shown how to find critical strain from load-displacement or stress-strain data. How to locate the point programmatically and consistently is a different matter. The theory offers two ways to find the critical strain location. The first is by locating the change in the parabolic shape of the stress-strain curve. The second is by finding the knee in the slope-strain curve. This section will look into the various methods used to find critical strain.

3.2.1 Critical Strain from Stress-Strain Curve

A typical stress-strain curve from the test specimens is shown in Figure 16. The data taken after the ultimate tensile stress should indicate a change in the path of the parabola similar to that shown in Figure 13. The result is essentially two parabolas meeting at the critical strain point. Figure 17 is a closer look at the data beginning at the ultimate tensile stress location. It is clear from the figure that there are two distinct parabolas within the curve. This provides the first process at which to find the critical strain. Fit two parabolas to the data and find where they intersect. The intersection point is the critical strain of the material. The algorithm involves incrementally stepping through the data points and fitting two parabolas through each side of the current data point. The correct parabolas are identified when the minimum error between the data and fitted parabola is found using a least squares approach. The MATLAB code developed for the study can be found in APPENDIX A.

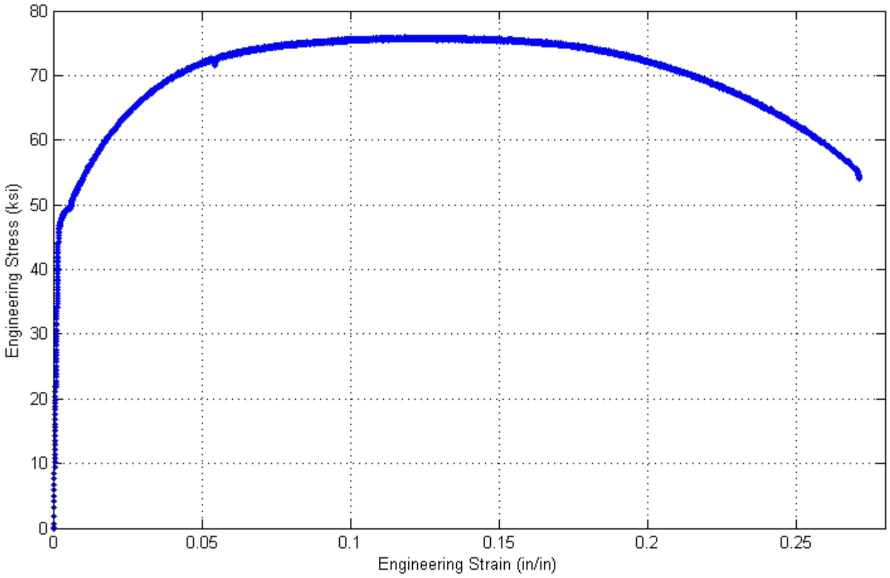

Figure 16: Engineering Stress-Strain Curve

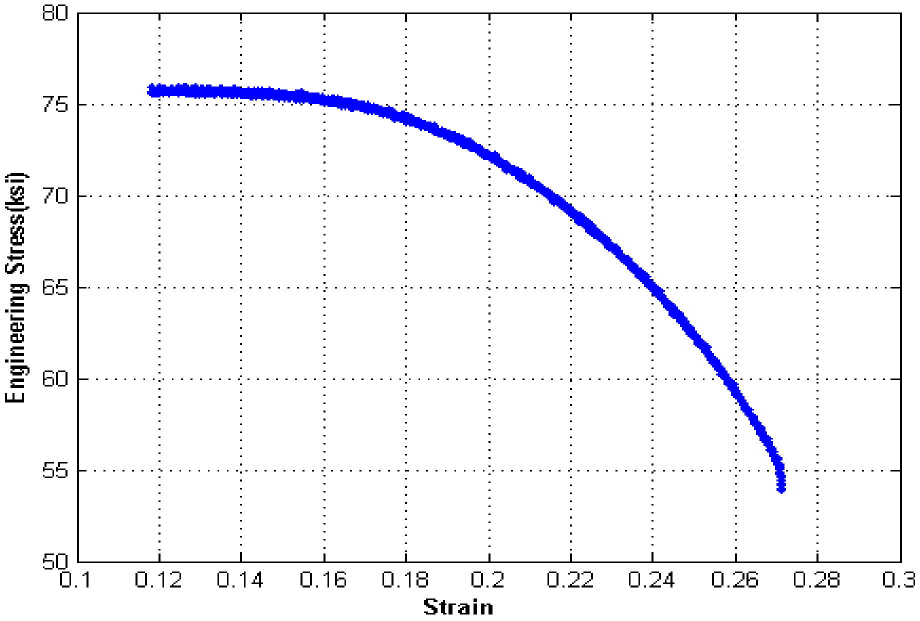

Figure 17: Critical Stress-Strain Data

3.2.2 Critical Strain from Slope-Displacement Curve

Figure 18 is a plot of the derivative of the stress-strain curve shown in Figure 17. The second method considered for calculating critical strain is fitting two lines to the slope-strain curve. The two lines will intersect at the critical strain value. This is similar to what Fischer et. al. (1995) shows in Figure 15. The difficulty with this method lies in the numerical differentiation required to calculate the first derivative of the stress-strain curve. Figure 19 is an example of the results for the critical strain using the slope-displacement curve. Many different numerical methods exist each with a unique parameter used for fitting or smoothing. The goal of this research is to see how these parameters affect the critical strain value and what the optimum values are for each parameter. Numerical differentiation is covered in the next section.

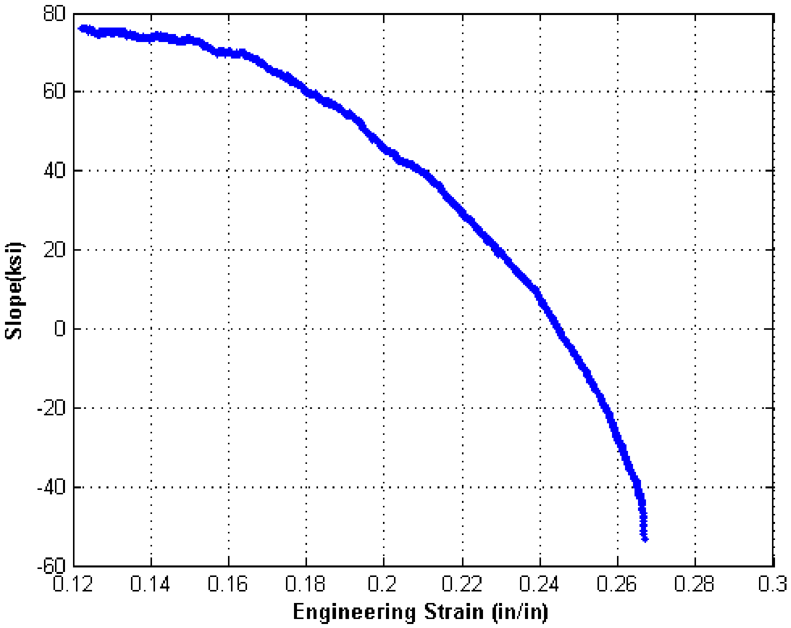

Figure 18: Typical Slope Strain Curve

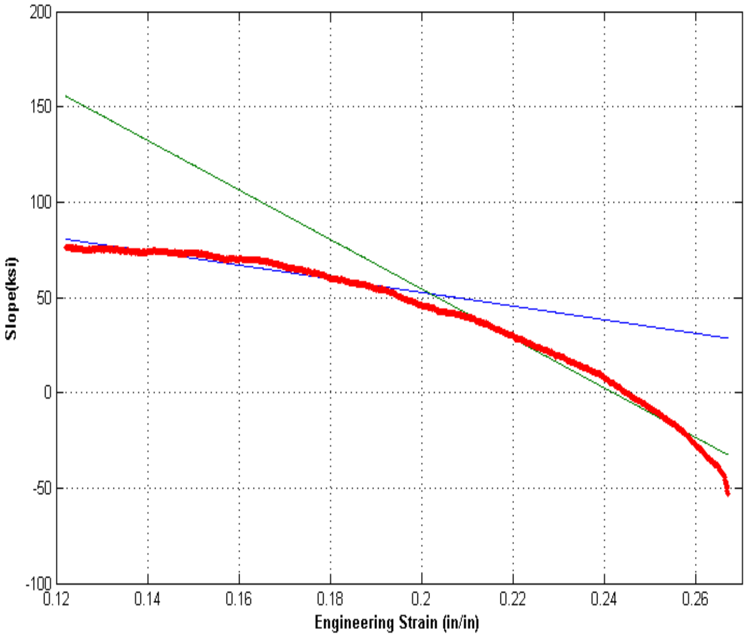

Figure 19: Critical Strain Results

3.3 Numerical Differentiation Techniques

The research conducted by Fischer et. al. (1995) has shown the critical strain is located at the knee of the stress-strain curve or at the second knee in the derivative of the stress-strain curve. Figure 15 shows that after incipient necking, a straight line occurs on the slope-displacement curve beginning at necking and ending at failure. When a microcrack forms, the straight line is bent and a knee is formed. The knee is indicative of a change in the failure process. Before the knee, the primary source of deformation is the growth and coalescence of microvoids. After the knee, the deformation process changes to the propagation of the microcrack that has formed in the center of the specimen.

Figure 16 shows the stress-strain curve from a typical tensile test. Only the data after the ultimate tensile stress is required for the critical strain analysis. This comes from the fact that the theory states the knee will occur after incipient necking which begins at the ultimate tensile stress. Figure 17 is a plot of the data from the ultimate tensile stress to the failure stress. The curve is parabolic in shape which will become a straight line when differentiated or in the case of this research, two lines similar to that shown in Figure 15.

Analysis of experimental data most often uses numerical methods to approximate operations such as differentiation and integration. Data is considered an unknown function thus eliminating the possibility of using closed form solutions for differentiation. As discussed previously, the stress-strain curve does not always show a clear and distinct knee. Under these circumstances the slope-strain curve is examined for a second knee signaling the onset of a microcrack. To examine the slope-strain curve, an approximation of the derivative is developed using numerical differentiation techniques.

The problem of numerical differentiation is known to be ill posed in the sense that small perturbations of the function to be differentiated may lead to large errors in the computed derivative. Figure 20 is a close up view of the engineering stress-strain curve. The figure shows some inherent noise associated with the data. The techniques used for numerical differentiation fall into three categories: difference methods, interpolation methods and regularization methods (Ramm 2001). These methods are also classified into two broad categories: local and global (Ahnert 2007). Local methods work by fitting or interpolating data on a subinterval of the domain. Global methods estimate the derivative based on the entire interval or domain.

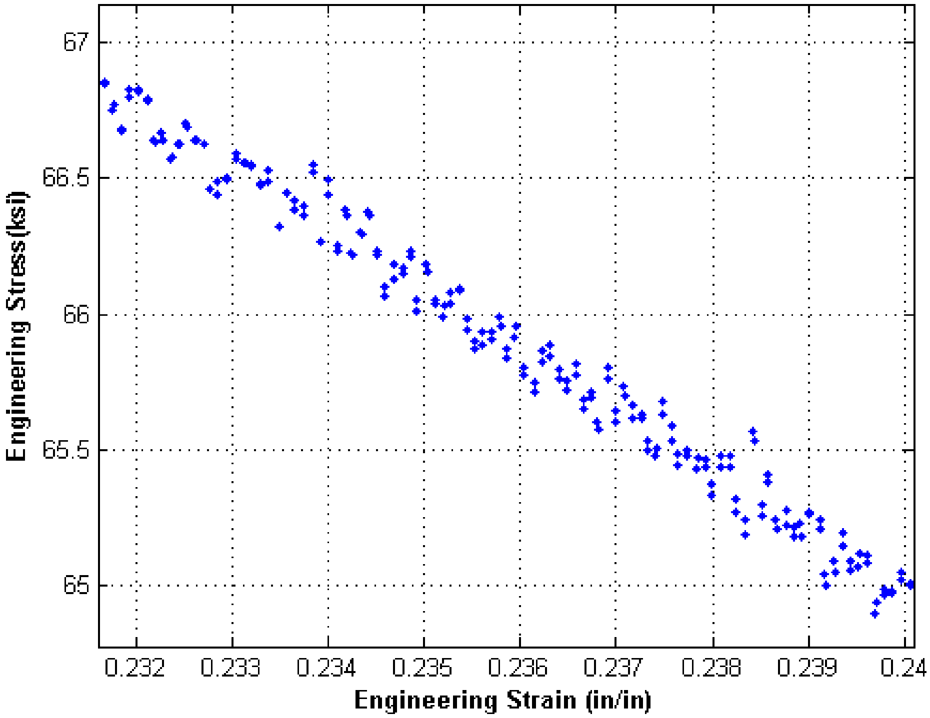

Figure 20: Close Up View of Stress-Strain Curve

3.3.1 *Finite Difference Methods*

Finite difference formulas are local methods easily derived from Taylor series expansions shown as Equation 15. Any continuous differentiable function $\Phi(x)$ can, in the vicinity of x_i, be expressed as a Taylor series. By replacing x by x_{i+1} or x_{i-1} in the expansion, one obtains expressions for the variable values at these points in terms of the variable and its derivatives at x_i. Rearranging the Taylor series expansion leads to

Equation 16. The first term in Equation 16 is a finite difference approximation and is typically referred to as the first-order forward difference method. The second term is the error term. Similarly, the first-order backward difference is obtained by expanding f'_{j-1} about x_j and is shown in Equation 17. One of the most commonly used finite difference methods is the central difference method shown in Equation 18. This method is obtained by subtraction of two Taylor series expanded at x_{i+1} and x_{i-1}. (Ferziger 2002; Moin 2010)

$$f\left(x_{j+1}\right) = f\left(x_j\right) + \left(x_{j+1} - x_j\right)f'\left(x_j\right) + \frac{\left(x_{j+1} - x_j\right)^2}{2} f''\left(x_j\right) + \cdots \tag{15}$$

$$f'\left(x_j\right) = \frac{f\left(x_{j+1}\right) - f\left(x_j\right)}{\Delta x_j} - \frac{\Delta x_j}{2} f''\left(x_j\right) + \cdots \tag{16}$$

$$f'_j = \frac{f_j - f_{j-1}}{\mathrm{h}} + O(h) \tag{17}$$

$$f'_j = \frac{f_{j+1} - f_{j-1}}{2\mathrm{h}} - \frac{h^2}{6} f'''_j + \cdots \tag{18}$$

Higher accuracy is obtained when a uniform spacing is used with the finite difference approximations. When used with non-uniform step sizes, such as the data collected for this research, the degree of accuracy is decreased due to fewer cancellations in the Taylor series expansion. Assuming the step sizes are more or less equal, the results of the differentiation of Figure 17 using finite differences are shown in Figure 21. As can be seen in Figure 21, the forward difference method amplifies noise in the data and obscures the true shape of the derivative.

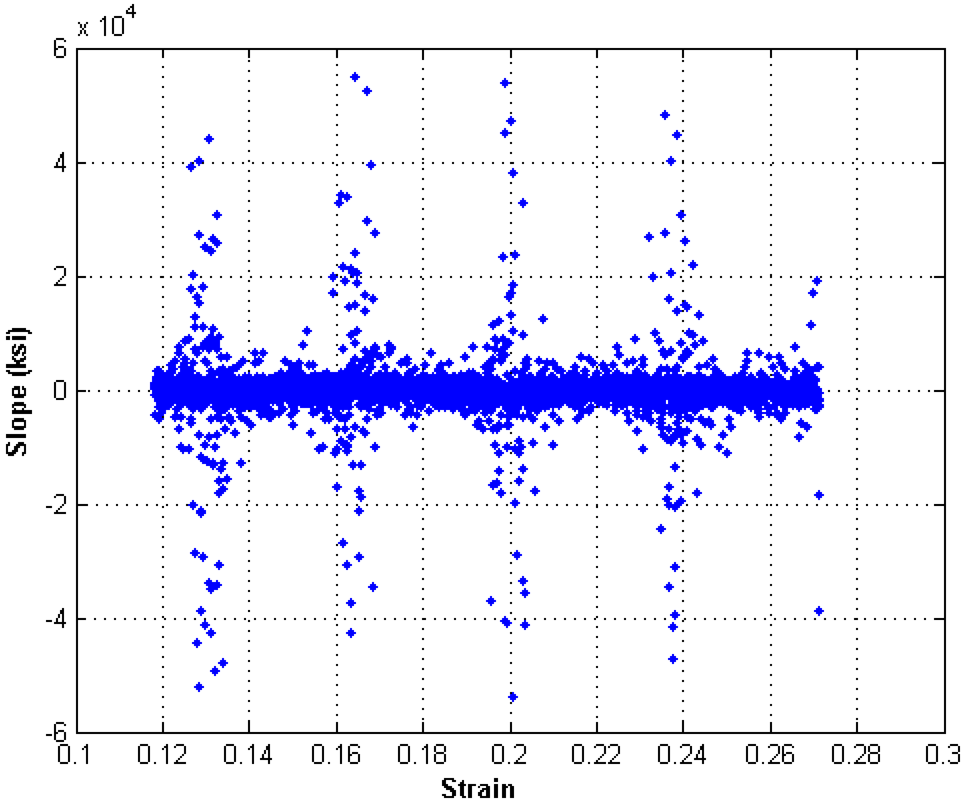

Figure 21: First-Order Backward Difference Method

Research conducted by Singh (2009) developed a method for using finite differences with unequal subintervals. The paper discusses how finite differences have developed over the years to include closed form solutions that can give approximations of arbitrary order. These formulas were developed using equally spaced grid points. The case of unequal grid points is examined due to the nature of experimental data. Much of the experiments involve an independent variable that is difficult to control during the experiment, thus leading to unequal data intervals. In the case of this research, the unequal data points are the strain values. This is due to the displacement control of the test frame. The load actuator is set to move at a specific strain rate, but the data points are not exactly equal strain intervals because of the strain associated with the test frame itself. The clip gauge used to calculate strain will read different strain steps than the displacement of the test frame. Equations 19-21 are the closed form solution for the three point finite difference formula. The results of the three and four point finite difference method for unequally spaced intervals are shown in Figure 22 and Figure 23 respectively.

$$f'(x_0) = \frac{2h_1 + h_2}{h_1(h_1 + h_2)} f_0 + \frac{h_1 + h_2}{h_1 h_2} f_1 - \frac{h_1}{(h_1 + h_2)h_2} f_2 \tag{19}$$

$$f'(x_1) = \frac{h_2}{h_1(h_1 + h_2)} f_0 - \frac{h_1 - h_2}{h_1 h_2} f_1 + \frac{h_1}{(h_1 + h_2)h_2} f_2 \tag{20}$$

$$f'(x_2) = \frac{h_2}{h_1(h_1 + h_2)} f_0 - \frac{h_1 + h_2}{h_1 h_2} f_1 + \frac{h_1 + 2h_2}{(h_1 + h_2)h_2} f_2 \tag{21}$$

The true derivative of the function is hidden within the amplified noise caused by the numerical differentiation. This is unacceptable for the critical strain analysis as it will cause unreliable results. Assuming equally spaced grid points and using the previous formula provides a more reasonable look at the derivative. This method is used in this research as one of the methods for calculating critical strain.

Research done by Chartrand (2011), Ahnert (2007) and Ramm (2001) discourage the use of finite differences as a differentiation technique. The advantages of finite differences are in the simplicity of the method and ease of implementation. The scheme is most commonly used when the function is smooth and well known. In cases where there is noise in the data, the finite differences method amplifies the noise. In the study done by Anhert (2007), finite difference is described as orders of magnitude off from other methods and is only used in the research as a worst case demonstration. Similarly, finite difference is used as a worst case demonstration for calculating critical strain.

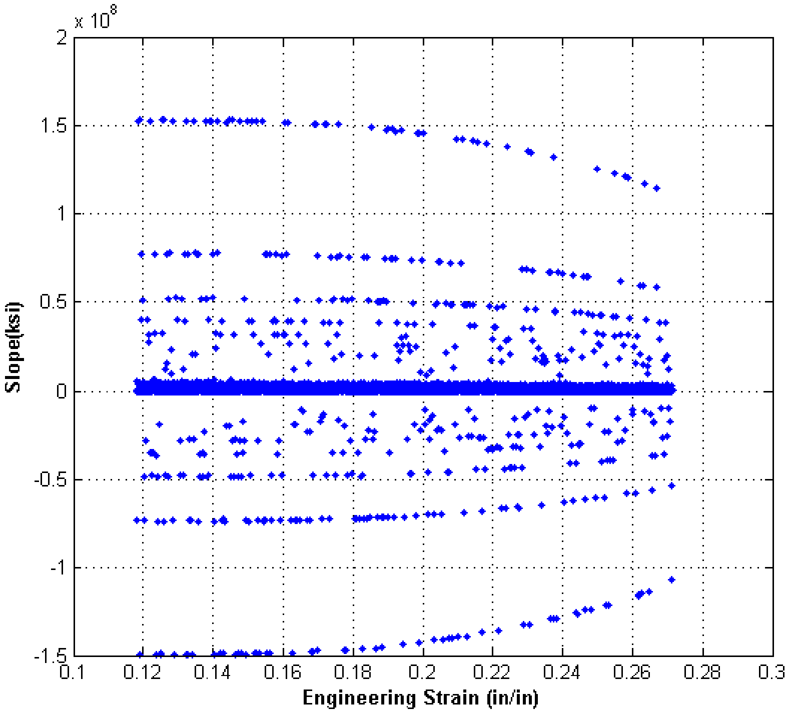

Figure 22: 3 Point Finite Difference Method with Lagrange Polynomials

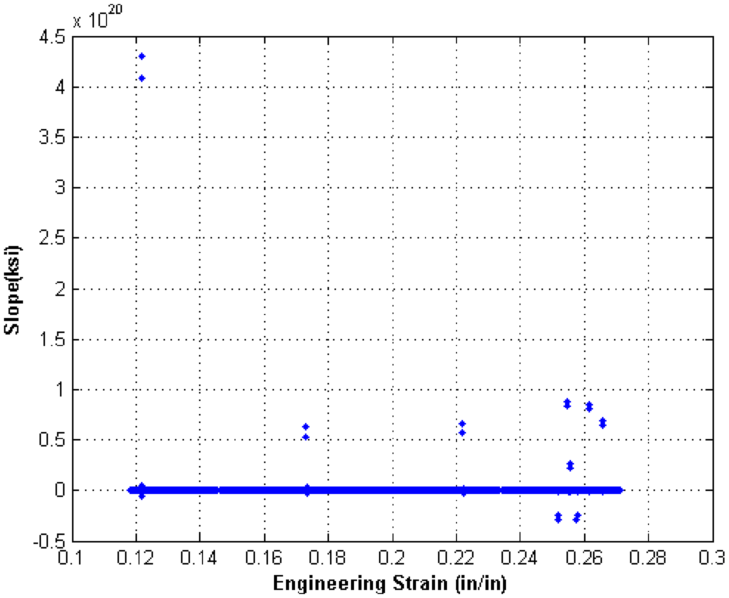

Figure 23: 4 Point Finite Difference Method with Lagrange Polynomials

3.3.2 Savitzky-Golay-Filtering Method

Savitzky and Golay (1964) wrote a paper describing a new method for filtering digital signals or test data. The goal of any filtering algorithm is to eliminate noise while preserving the integrity of the original signal or curve. The Savitzky-Golay filtering method is similar to the moving average method. A subset of the data is selected around the target point. A best fit approximation is made of the function using a least squares method. The fit is made to a polynomial appropriate for the selected curve. The derivative at the target point is the derivative of the best fit polynomial. The “window” is then shifted over by one data point and the process is repeated.

This procedure is considered very effective and is used often for numerical differentiation. The key idea of Savitzky–Golay filtering is the conservation of higher statistical moments. A simple moving average always reduces the height of a local extremum. Due to the mentioned conservation property, the Savitzky–Golay filter shows this reduction to a much less extent. Smoothness, however, is not guaranteed and the derivative can be discontinuous, which is not desirable for an estimate useful in physical problems where the function is typically required to be smooth. (Ahnert 2007)

Juliano et al. used a numerical analysis technique to take the derivative of the load-displacement curve in an effort to find certain events during the loading and unloading of fused silica. The numerical first derivative at a depth of h_x was taken to be the slope of the least-squares fit between load-displacement data points and is given in Equation 22. A closer examination of the equation reveals that it is simply the Savitzky-Golay filtering method using a linear best fit. A simplified version for easier computation presented in the paper is given as Equation 23 which is simply the central difference method described in section 3.3.1. (Juliano et al. 2004)

$$\left(\frac{dP}{dh}\right)_{h_x} = \frac{y\left(\sum_{P_{x-\left(\frac{y-1}{2}\right)}, h_{x-\left(\frac{y-1}{2}\right)}}^{P_{x+\left(\frac{y-1}{2}\right)}, h_{x+\left(\frac{y-1}{2}\right)}} Ph\right) - \left(\sum_{h_{x-\left(\frac{y-1}{2}\right)}}^{h_{x+\left(\frac{y-1}{2}\right)}} h\right)\left(\sum_{P_{x-\left(\frac{y-1}{2}\right)}}^{P_{x+\left(\frac{y-1}{2}\right)}} P\right)}{y\left(\sum_{h_{x-\left(\frac{y-1}{2}\right)}}^{h_{x+\left(\frac{y-1}{2}\right)}} h^2\right) - \left(\sum_{h_{x-\left(\frac{y-1}{2}\right)}}^{h_{x+\left(\frac{y-1}{2}\right)}} h\right)} \qquad 22$$

$$\left(\frac{dP}{dh}\right)_{h_x} = \frac{P_{x+\left(\frac{y-1}{2}\right)} - P_{x-\left(\frac{y-1}{2}\right)}}{h_{x+\left(\frac{y-1}{2}\right)} - h_{x-\left(\frac{y-1}{2}\right)}} \qquad 23$$

The size of the window used acts like a smoothing parameter. The larger the window used for the least squares fit the smoother the derivative. Figure 24 is the derivative calculated using a window size of 25 points. This window was moved point by point taking the slope of a parabola fitted through the points of the window. The same was done for Figure 25 with the exception that the window size was 207 points wide. Notice the increased amount of smoothing shown in Figure 25. This smoothing parameter should be optimized so that the critical strain value calculated is consistent and reliable.

3.3.3 Regularization Methods

Typical finite difference approximations will greatly amplify any noise present in test data. Denoising the data before or after differentiating does not generally give satisfactory results. The example below (Figure 26), taken from Chartrand (2011), shows how finite difference (top right) amplifies the noise and does not accurately reflect the true derivative. Even after denoising the data before using finite differences (bottom left), the data is still inaccurate and noisy. The regularization technique (bottom right) accurately shows the derivative, including the jump, with very little associated noise.

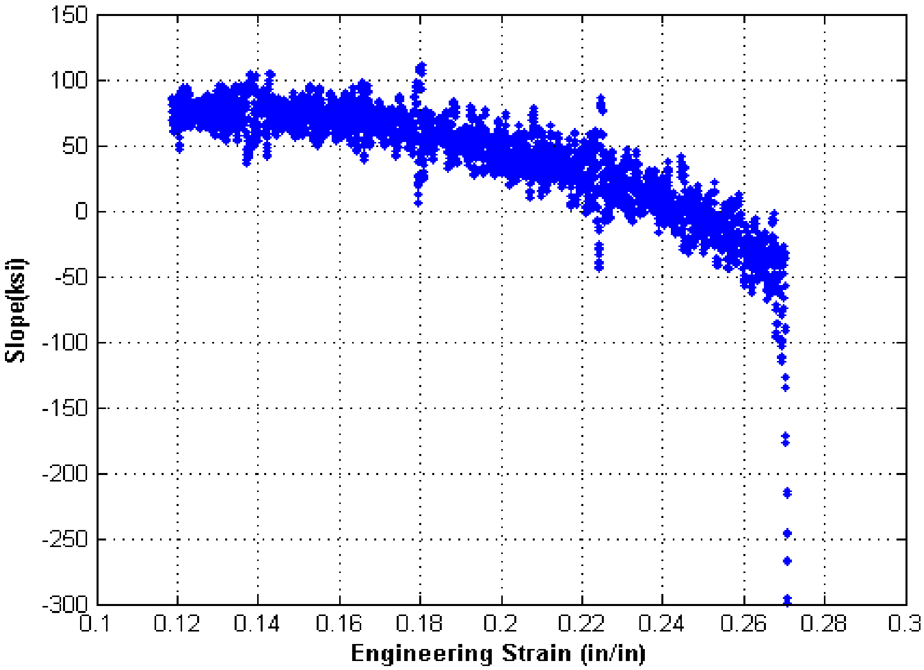

Figure 24: Savitzky-Golay Method n = 25

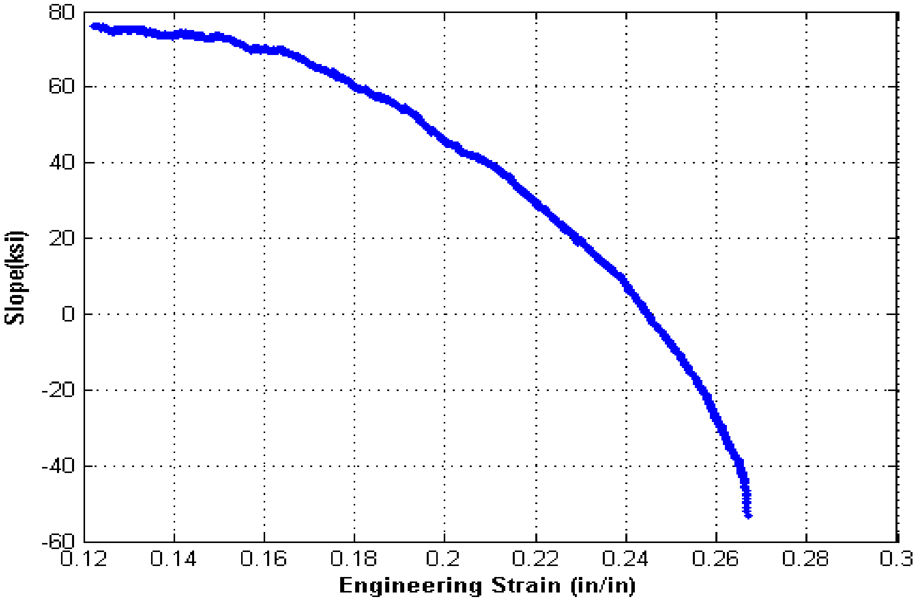

Figure 25: Savitzky-Golay Method n = 207

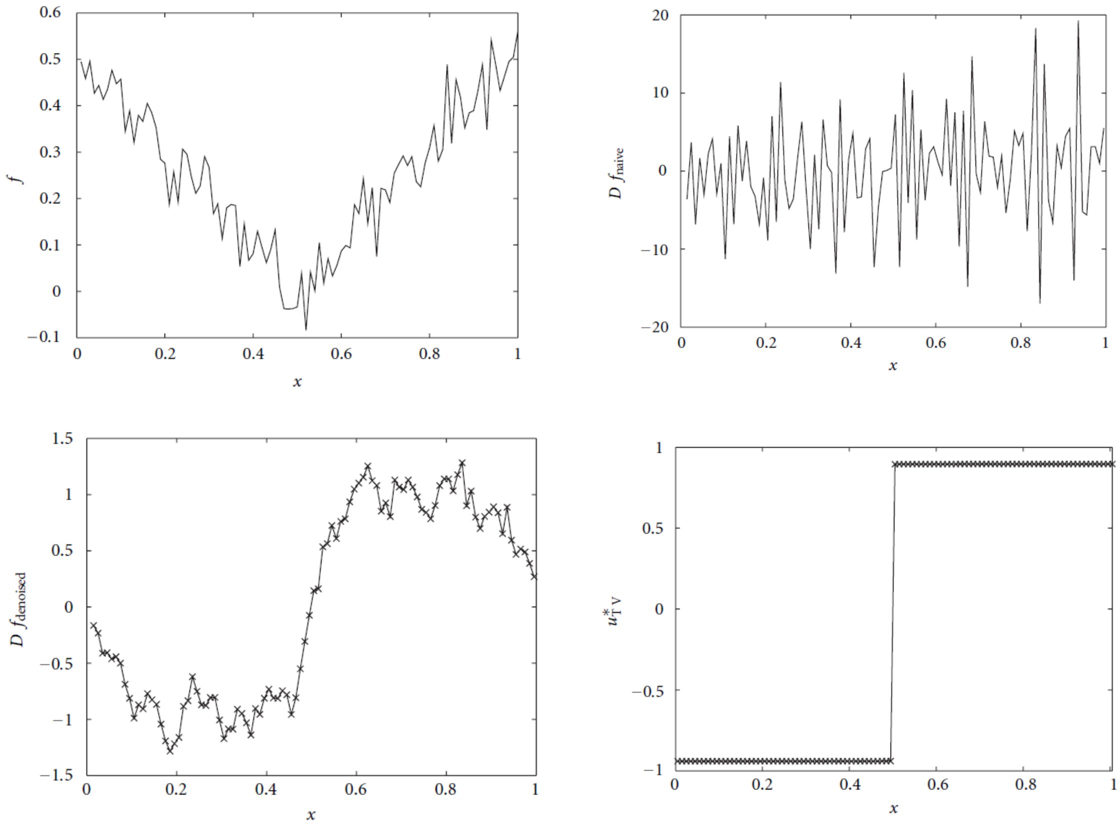

Figure 26: Regularization Example (Chartrand 2011)

Regularization is a technique implemented in mathematics and statistics to solve ill-posed problems or to prevent overfitting. The computed derivative will have some degree of regularity based on the chosen parameters. The most common regularization technique used is the Tikhonov regularization. The derivative is the minimizer of the functional shown in Equation 24. This method is essentially a penalized least squares method. The penalty function acts with a smoothing parameter to penalize the least squares fit. For example, by using the curvature as a measure of smoothness, one can penalize a least squares fit for roughness. A great advantage to the regularization technique is it can be solved using matrix arithmetic rather than loops. (Eilers 2003)

$$\mathrm{F(u) = \alpha R(u) + DF(Au - f)} \tag{24}$$

In the paper by Strickel (2010) the theory of regularization is explained in detail. As previously noted, the functional has a goodness-of-fit term defined in Equation 25 and a “roughness” term given by Equation 26. The derivative in Equation 26 is of order-d. The correct order for the purpose of this research is three. Stickel (2010) recommends using two orders higher than your required order. Therefore, since the first order derivative is required for critical strain, a third order derivative is used in the functional. Since both of the terms below cannot be minimized simultaneously a compromise is needed. This is done with the introduction of a weighting parameter λ. The final form of the functional is shown in Equation 27. One of the major advantages to this technique is the use of matrices to evaluate the function that minimizes the functional $\mathrm{Q(\hat{y})}$. Equation 27 can be expressed in matrix notation and is shown in Equation 28. For implementing the method in MATLAB, the reader is referred to the work done by Eilers (2003).

$$\int_{x_1}^{x_N} |\hat{y}(x) - y(x)|^2 dx \tag{25}$$

$$\int_{x_1}^{x_N} \left|\hat{y}^d(x)\right|^2 dx \tag{26}$$

$$Q(\hat{y}) = \int_{x_1}^{x_N} |\hat{y}(x) - y(x)|^2 dx + \lambda \int_{x_1}^{x_N} \left|\hat{y}^d(x)\right|^2 dx \tag{27}$$

$$Q = (\hat{y} - y)^T B(\hat{y} - y) + \lambda (D\hat{y})^T B(D\hat{y}) \tag{28}$$

4 PROPOSED NEW DAMAGE ASSESSMENT METHOD

The new damage assessment method proposed by Blade Energy Partners is an attempt to simplify and expedite the evaluation of mechanical damage severity. Currently, engineers rely on FE analysis to evaluate severe dents. A report from an in line inspection tool could have thousands of detected dents. There is a need for a system that can quickly and accurately prioritize and flag severe damage. FEA is time costly and requires specialized and experienced engineers to use. This proposed method could provide a simplified means for delegating the use of such a time costly tool.

The strain equations used for dent assessment have been reviewed and modified do to errors with various assumptions. Equations 1-3 are the ASME B31.8 (2003) equations. Because of possible complications in dent profile, other formulas in the open literature or those derived by qualified engineers are also allowed by the ASME code. The majority of the information in this section was found in the comprehensive review of strain-based models for dent assessment compiled by Gao et. al. (2008). For more information regarding strain-based dent assessment, readers are referred to the above resource.

Noronha et. al. (2010) identified that ASME B31.8 (2003) overestimates the circumferential and longitudinal bending strains by a factor of 2. Noronha et. al. (2010) identified the error as a failure to divide the wall thickness in half. This has since been remediated in the 2007 version of ASME B31.8. In addition to errors associated with the bending strain, Noronha et. al. (2010) found that the combined strain equations (Equations 5 and 6) were derived using incorrect plane strain assumptions leading to inaccurate results. Noronha et. al. (2010) suggests modifications to correct this error.

The first modification is to use the von Mises strain shown in Equation 29. The elastic strains are assumed negligible within the dent profile thus assuming all strain within the dent region is plastic. Plastic flow is characterized as incompressible or no volume change. This allows poisons ratio to take on the value of 0.5, the value for zero volume change. Substitution of $\nu = 0.5$ into Equation 29 gives Equation 30. ε_I, ε_{II}, and ε_{III}

are the principal strains which are assumed to act in the circumferential and longitudinal directions of the pipe. ε_{III} is assumed zero. The principal strains are then found by combining ε_1, ε_2, and ε_3 which are calculated as before. The principal strains are substituted into the equivalent strain equation leading to Equations 31 and 32 . These give the strain on the inside and outside faces of the pipe. They are nearly identical to Equations 5 and 6 except for the 2/3 coefficient in front of the square root.

$$\epsilon_{\mathrm{eqv}} = \frac{1}{1+\nu}\sqrt{\frac{1}{2}\left[(\epsilon_{\mathrm{I}} - \epsilon_{\mathrm{II}})^2 + (\epsilon_{\mathrm{II}} - \epsilon_{\mathrm{III}})^2 + (\epsilon_{\mathrm{III}} - \epsilon_{\mathrm{I}})^2\right]} \qquad 29$$

$$\epsilon_{\mathrm{eqv}} = \frac{\sqrt{2}}{3}\sqrt{(\epsilon_{\mathrm{I}} - \epsilon_{\mathrm{II}})^2 + (\epsilon_{\mathrm{II}} - \epsilon_{\mathrm{III}})^2 + (\epsilon_{\mathrm{III}} - \epsilon_{\mathrm{I}})^2} \qquad 30$$

$$\epsilon_{\mathrm{i}} = \frac{2}{3}\sqrt{\epsilon_1^2 - \epsilon_1(\epsilon_2 + \epsilon_3) + (\epsilon_2 + \epsilon_3)^2} \qquad 31$$

$$\epsilon_{\mathrm{o}} = \frac{2}{3}\sqrt{\epsilon_1^2 + \epsilon_1(-\epsilon_2 + \epsilon_3) + (-\epsilon_2 + \epsilon_3)^2} \qquad 32$$

The second modification is to assume that the strains within the dent region are mostly plastic. This means that the incompressibility condition of plasticity applies. Equation 33 shows the incompressibility condition. In the previous equations, plane strain was assumed and ε_{III} was set equal to zero. Using the incompressibility condition, the value for ε_{III} is dependent upon the values of ε_I and ε_{II}. Substitution of ε_{III} into Equation 30 gives Equation 34, the new equivalent strain. By substituting ε_1, ε_2, and ε_3 as done before, the new equations for the inside and outside surface strains are obtained. These are shown as Equations 35 and 36.

$$\epsilon_{\mathrm{I}} + \epsilon_{\mathrm{II}} + \epsilon_{\mathrm{III}} = 0 \quad 33$$

$$\epsilon_{\mathrm{eqv}} = \frac{2}{\sqrt{3}}\sqrt{\epsilon_{\mathrm{I}}^2 + \epsilon_{\mathrm{I}}\epsilon_{\mathrm{II}} + \epsilon_{\mathrm{II}}^2} \quad 34$$

$$\epsilon_{\mathrm{i}} = \frac{2}{\sqrt{3}}\sqrt{\epsilon_1^2 + \epsilon_1(\epsilon_2 + \epsilon_3) + (\epsilon_2 + \epsilon_3)^2} \quad 35$$

$$\epsilon_{\mathrm{o}} = \frac{2}{\sqrt{3}}\sqrt{\epsilon_1^2 - \epsilon_1(-\epsilon_2 + \epsilon_3) + (-\epsilon_2 + \epsilon_3)^2} \quad 36$$

Noronha et. al. (2010) compared the different modified equations to the results from an FE analysis to show the influence of the various assumptions. The results are reproduced in Table 3 and Table 4 for inner and outer surfaces respectively. The results show that the ASME and von Mises equations severely underestimate the strain within the dent. The equations incorporating the incompressibility condition slightly overestimate the strain on the inner surface and slightly underestimate the strain in the outer surface. Despite the improvements to the strain equations, they still differ from FE results. The current ASME equations appear inaccurate.

Table 3: Combined Strain Versus FE von Mises Strain, Inner Surface (Noronha et al. 2010)

d/OD (%)	ASME B31.8 (%)	Plane Strain (%)	Radial Components (%)	FE (%)
6	6.41	4.27	12.18	10.69
12	6.41	4.27	12.67	10.37
18	6.16	4.10	12.20	10.15

Table 4: Combined Strain Versus FE von Mises Strain, Outer Surface (Noronha et al. 2010)

d/OD (%)	ASME B31.8 (%)	Plane Strain (%)	Radial Components (%)	FE (%)
6	6.33	4.22	10.54	11.88
12	6.26	4.18	9.08	11.76
18	6.09	4.06	8.40	11.03

Czyz et al. (2008) described an alternative method that combines mathematical algorithms and FEA tools for dent strain calculations. The authors suggest that generic FEA programs designed to solve equations are inaccurate for pipe damage with a known deflected profile. Their approach uses a shell model with two degrees of freedom in the middle of the pipe wall. The FE analysis provides the deflections, u and v, in the xy plane. The deflections, w, in the radial direction are given by the high resolution in line inspection (ILI) tool. The results from the two analyses are used to solve equations 37-45 to find the equivalent strain. Strains in a pipe wall consist of longitudinal and circumferential components. Each component can be further broken down to bending and membrane strains.

Figure 28 shows the strain components in a pipe wall proposed by the authors. Equations 37 and 38 are the bending strain in the longitudinal and axial directions respectively. The bending strains are a function of the distance from the neutral axis of the pipe wall, Z. The maximum bending strain occurs at the wall surfaces half the thickness away from the neutral axis. Equations 39, 40 and 41 are the equations for the membrane strain in the longitudinal, axial and shear strains in the xy plane. The membrane strain requires the displacement data from the FE results. The membrane and bending strains are combined in the x and y directions as shown in Equations 42 and 43. The x and y strains are then used in Equations 44 and 45 to calculate equivalent strain. The equations for equivalent strain are derived directly from plastic strain theory with an incompressibility condition. As noted previously from the work done by Noronha et. al. (2010), the pipe wall is considered a thin plate and therefore is considered a plane stress and not a plane strain condition. Gao et. al. (2008) compared the ASME B31.8 and the Lukasievicz and Czyz et. al. methods and found two major differences.

The first major difference was the effective strain. ASME B31.8 equates the shear strain to zero and has a sign difference in the mid-term $\epsilon_x\epsilon_y$. Czyz et. al. demonstrated that the difference in effective strain can be more than 50% with the assumption that the shear strain term is equal to zero. Gao et. al. (2008) compared the two equations using data from the dent study reported by Baker (2009). The results are reproduced in Table 5. The ASME equations underestimated the effective strain by a factor of 2.0 and 1.8 for the inner and external surfaces respectively.

Table 5: Difference in the Calculated Effective Strain Between Eq. 4 and 44 (Gao et al. 2008)

			Case 1	**Case 2**	**Case 3**
Strain Component	ε_1, Circumferential Bending		2.3%	2.3%	2.3%
	ε_2, Longitudinal Bending		1.1%	1.5%	2.2%
	ε_3, Longitudinal Membrane		0.59%	0.8%	1.0%
Effective Strain	Inner Surface	ASME B31.8	2.10%	2.29%	2.92%
		Lukasievicz	4.06%	4.58%	5.64%
		Difference	193.8%	199.9%	193.1%
	External Surface	ASME B31.8	2.13%	2.08%	2.03%
		Lukasievicz	3.05%	3.18%	3.59%
		Difference	143.4%	153.1%	177.2%

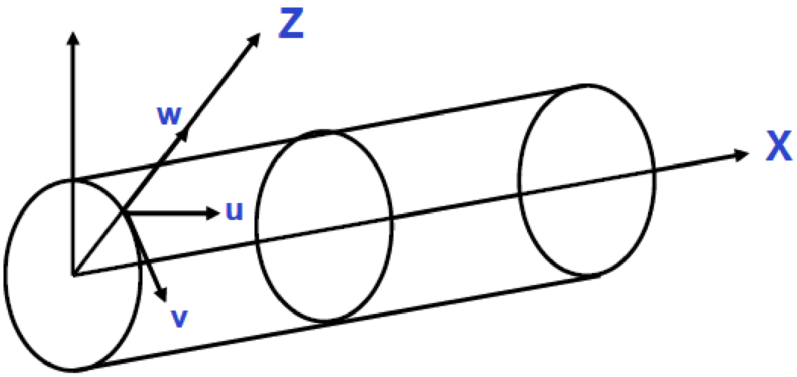

Figure 27: Coordinate System of the Pipe and Displacement Components (Gao et al. 2008)

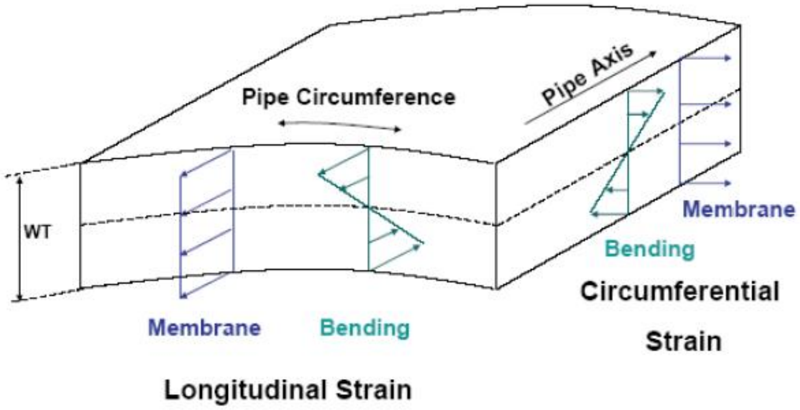

Figure 28: Strain Components in a Pipe Wall (Gao et al. 2008)

$$\epsilon_x^b = \frac{t}{2}\frac{\partial^2 w}{\partial x^2} \tag{37}$$

$$\epsilon_y^b = \frac{t}{2}\frac{\partial^2 w}{\partial y^2} \tag{38}$$

$$\epsilon_x^m = \frac{\partial u}{\partial x} + \frac{1}{2}\left(\frac{\partial w}{\partial x}\right)^2 + \epsilon_x^0 \tag{39}$$

$$\epsilon_y^m = \frac{\partial u}{\partial y} + \frac{w}{R} + \frac{1}{2}\left(\frac{\partial w}{\partial y}\right)^2 + \epsilon_y^0 \tag{40}$$

$$\gamma_{yx} = \frac{\partial u}{\partial y} + \frac{\partial v}{\partial x} + \left[\frac{\partial w}{\partial x}\right]\left[\frac{\partial w}{\partial y}\right] \tag{41}$$

$$\epsilon_x = \epsilon_x^m \pm \epsilon_x^{-b} \tag{42}$$

$$\epsilon_y = \epsilon_y^m \pm \epsilon_y^{-b} \tag{43}$$

$$\epsilon_{eq} = \frac{2}{\sqrt{3}} \sqrt{\epsilon_x^2 + \epsilon_x \epsilon_y + \epsilon_y^2} \tag{44}$$

$$\epsilon_{eq} = \frac{2}{\sqrt{3}} \sqrt{\epsilon_x^2 + \epsilon_x \epsilon_y + \epsilon_y^2 + \frac{\gamma_{xy}^2}{2}} \tag{45}$$

The second major difference was with the membrane strains. ASME B31.8 uses equation 3 to calculate longitudinal membrane strain. The equation uses dent length and depth and does not require the dent profile. Rosenfeld (1998) introduced a method for calculating longitudinal membrane strain. The method assumes the membrane strain distribution is approximately the same as the radial (in-plane) displacements of a circular plate subject to point loading. This method accounts for the displacements on the pipe surface seen in FE analyses. Equation 46 is the strain distribution given the above assumption. Using various assumptions the membrane strain is calculated using equation 47 with the arc length calculated using equation 48. Both ASME B31.8 and Rosenfeld (1998) ignore the membrane strain in the circumferential direction. Lukasievicz and Czyz et. al. noted that Rosenfeld’s formula is not based on shell theory and is simplistic and inaccurate. They also go on to show that the circumferential membrane and shear strains can have similar magnitudes to the longitudinal strain. Gao et. al. (2008) suggested improvements to the ASME B31.8 methods including adopting the strain formula suggested by Lukasiewcz and Czyz et. al. for total strain, improve the longitudinal strain calculations, and consider circumferential strain.

$$\frac{du}{dr} + v\frac{u}{r} = -\left(\frac{dw}{dr}\right)^2 \tag{46}$$

$$\epsilon_{xi} = \frac{(L_s - L_i)}{L_i} \qquad 47$$

$$L_s = \sqrt{((z+u)_i - (z+u)_i)^2 + (w_{i+1} - w_i)^2} \qquad 48$$

Arumugam et. al. (2012) conducted a case study of a 30 inch natural gas pipeline segment. The pipe had been inspected by TransCanada Pipeline Limited (TCPL) with a Combo tool. A combo tool is similar to a PIG with the exception that the tool also detects gouges, cracks and metal loss. The tool uses an additional sensor that detects the magnetic flus leakage (MFL) caused by these types of defects. The tool found a 2.7%OD dent at the bottom of the pipe. The MFL detected by the tool reported 76% metal loss. Based on the depth and MFL information it was determined that the metal loss feature was most likely associated with a crack. An extensive study was conducted including strain calculations using the modified equations noted above and FEA results. Strains were calculated using ILI, laser scan, and hand profiles. The goal of the study was to find the root cause of the cracking found when the damage was uncovered. The dent was caused by a rock found during excavation. The pipe experienced spring-back causing differences in the reported profiles and depths. The laser profile was scaled to match the ILI data eliminating the effects of the spring-back.

The new assessment method uses a ductile failure damage indicator (DFDI) to assess the severity of the dent. The DFDI is based on the tri-axial stress field, equivalent Von Mise’s stress and critical strain. The DFDI was calculated using the results from an FE analysis. The results are reproduced in Table 6. Arumugam et. al. (2012) showed that the DFDI had a value greater than 1 and that the geometric strain and FEA strains were in good agreement (< 8%). The results showed that according to the DFDI the internal surface was susceptible to cracking. The principal stress contour plots and the actual crack path are reproduced below in Figure 29. The crack paths showed good agreement with the predicted crack paths from the FE results thus validating the DFDI model.

Table 6: Maximum Eqv. Strain DFDI (Arumugam et al. 2012)

Profile	Geometric Strain	FEA PEEQ Strain	Max. DFDI
LaserScan Internal	32.3%	35.0%	1.1

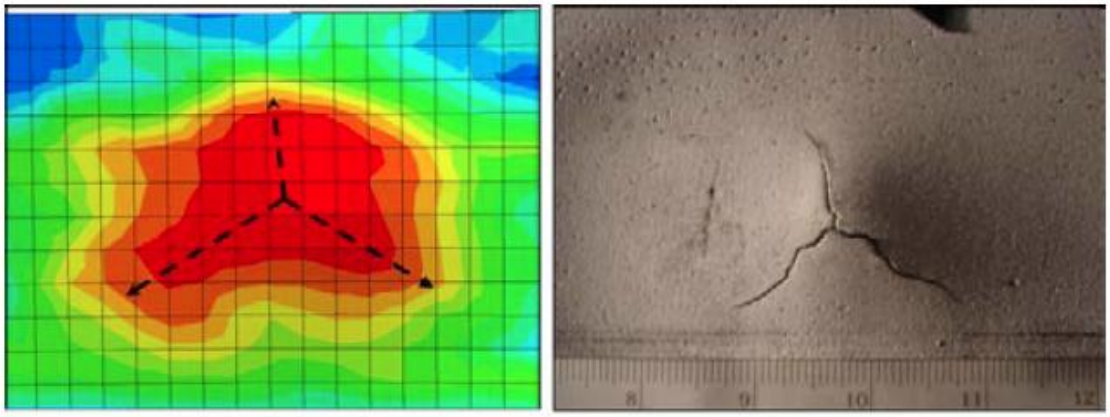

Figure 29: Maximum Principal Stress Plot and Actual Crack Path (Arumugam et al. 2012)

It has been shown in the previous discussion that many of the methods depend on FEA results for implementation. The strains calculated using the methods proposed by Lukasievicz and Czyz et. al. requires FEA to calculate longitudinal displacements for membrane strain and even the DFDI method uses the principal stress from an FE model. FEA has proven to be an effective tool for the damage assessment of pipelines. FEA is specialized and time consuming making it costly to use for many dents. It is for this reason that Arumugam et. al. (2012) has proposed a simplified DFDI approach that does not require the use of FE models. The method is designed to provide a tool for rapidly assessing and prioritizing pipeline damage.

The geometric strain using modified equations does not require FEA results and shows good agreement with the strains calculated using FEA. Arumugam et. al. (2012)

proposed using two extreme conditions to develop an upper and lower bound for DFDI. The first condition is bi-axial loading ($\sigma_1 \neq 0, \sigma_2 = \sigma_1, \sigma_3 = 0$) and the second is uni-axial loading ($\sigma_1 \neq 0, \sigma_2 = \sigma_3 = 0$). For a thin-wall pipe under internal pressure the DFDI equation reduces to equations 49 and 50. Using the simplified equations the study found that the upper bound of 1.0 was in good agreement with the value of 1.1 found using FEA results. The study validated the results and justified the progression to the current study which has the final goal of validating and implementing the simplified DFDI approach as a viable method for dent assessment.

$$DFDI_{upperbound} = \frac{\epsilon_{eqv}}{\left(\frac{\epsilon_0}{1.65}\right)} \qquad 49$$

$$DFDI_{lowerbound} = \frac{\epsilon_{eqv}}{\epsilon_0} \qquad 50$$

The current denting test was conducted to validate the DFDI approach and verify the need for additional testing. For this study, the results from the test are still under review and therefore a clear conclusion cannot be made regarding the validity of the simplified DFDI approach. The purpose of this study was to evaluate the denting process and its ability to accurately confirm the effectiveness of the DFDI. A detailed description of the procedures and parameters used for the critical strain, laser evaluation and denting test can be found in the following section.

5 TESTING PARAMETERS AND PROCEDURES

5.1 Critical Strain

The critical strain phase of this research required finding the material property known as critical strain. To accomplish this, the true stress and true strain curves were required. A machine vision system was used to assist in the tracking of the sample diameter as the specimen was loaded. The combined data from the test frame and camera system was used to analyze and calculate the critical strain for the pipe material. Testing for all phases of the research was performed in the Zachary Department of Civil Engineering, Structural and Materials Testing Laboratory at Texas A&M University, College Station, TX.

5.1.1 Specimen

The critical stain section of the project involved investigating the most accurate means of calculating a materials critical strain value. The investigation was conducted using sample material salvaged from the scrap end of the dented pipe. Five specimens were cut in the axial direction from the pipe section shown in Figure 30. The specimens had grip sections 1.25 inches long with a diameter of 0.325 inches. The gauge section was 1.25 inches long with a 0.252 inch diameter. The transition from the grip locations to the gauge length was made with a radius of 0.1875 inches. The specimen dimensions are shown below in Figure 31. An image of a typical sample can be seen in Figure 32. The pipe material was X52 steel.

Figure 30: Material from Denting Pipe

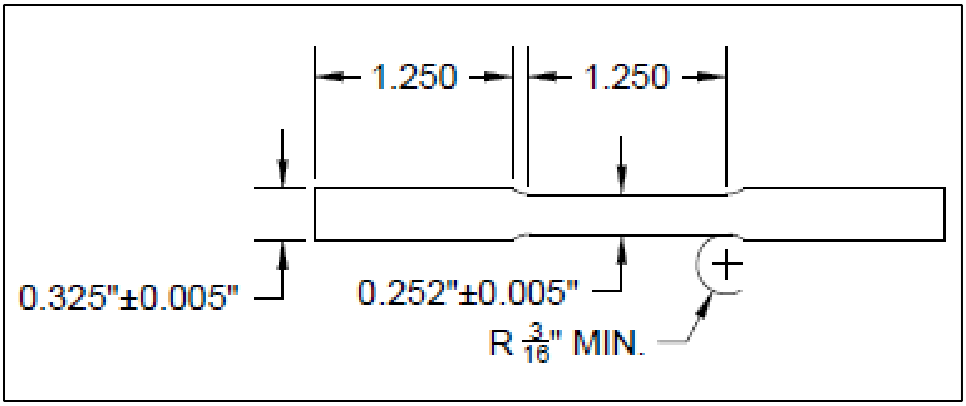

Figure 31: Sample Dimensions

Figure 32: Typical Critical Strain Sample

5.1.2 Equipment

Machine vision systems are used in a multitude of applications and environments. The most common application seen today is in quality control during the manufacturing of products. The advantages of machine vision systems are speed and accuracy. Cameras have the ability to do the redundant task of inspecting products with a high degree of accuracy and speed. These systems are designed for various working environments that are unfit for human workers. For this experiment, the machine vision system was selected for its ability to constantly track the diameter of a necking specimen during a tension test.

A common problem associated with standard tension tests is the omission of the circumferential strain. The circumferential stress causes a decrease in the diameter of the specimen or “necking”. The machine vision system is capable of measuring the change in diameter by capturing profile images of the sample as shown in Figure 33. The system consists of a GigE camera, telecentric lens, and a LED backlight as shown in Figure 34.

The telecentric lenses used for the backlight and camera polarize the light in a direction parallel to the axis of the camera and perpendicular to the axis of the specimen. The parallel light reduces the amount of diffraction as it passes by the sample. Diffraction causes the edges of an object to blur due to the interference of the bending light. The system detects a false edge resulting in a less accurate reading.

The light from the LED is first polarized by a telecentric lens before passing by the tensile specimen. The passing light is captured by another telecentric lens and focused onto the cameras CCD sensor. The projected image is free from distortion resulting in a scaled projection of the original object. The pixels of the sensor are of known size and are used to take measurements of the captured image. The software detects the edges of the object using the large contrast between the passing light and the black object. It then searches for the minimum distance between the two lines. The detected section is the minimum cross section of the specimen. A close up image of the camera and telecentric lens is shown in Figure 35.

The camera used in the experiment was a scA1600-14gc Basler Scout Camera. The camera used a Sony ICX274 AL/AQ progress scan CCD sensor. The sensor had 1624 pixels and 1234 pixels parallel and perpendicular to the specimen axis, respectively. Each square pixel had side dimensions of 4.4 micrometers. The maximum frame rate of the camera was 14 frames per second (fps). The test frame used was a MTS 20 kip axial load frame shown in Figure 36.

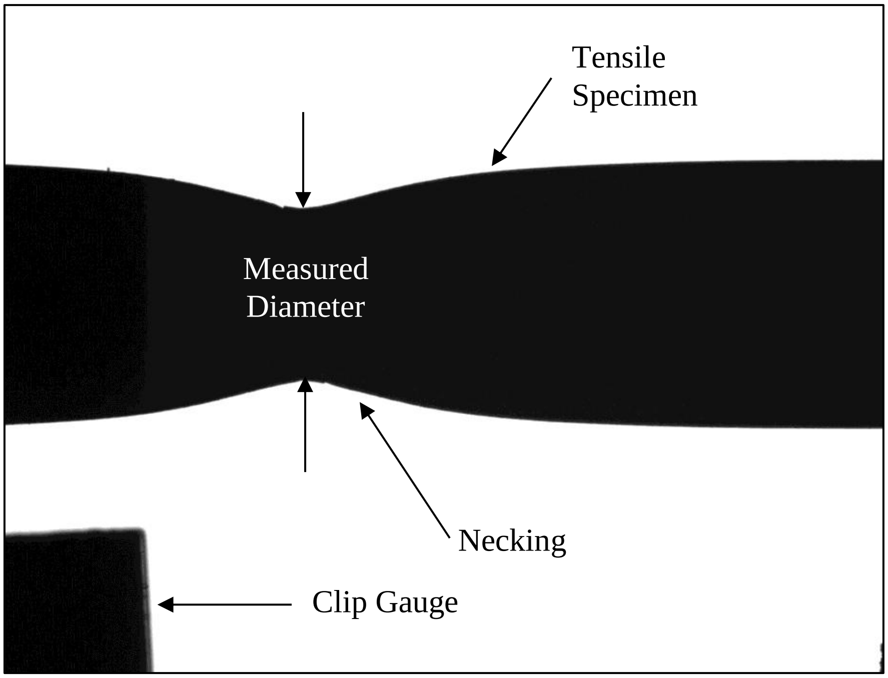

Figure 33: Specimen Profile Taken with Machine Vision System

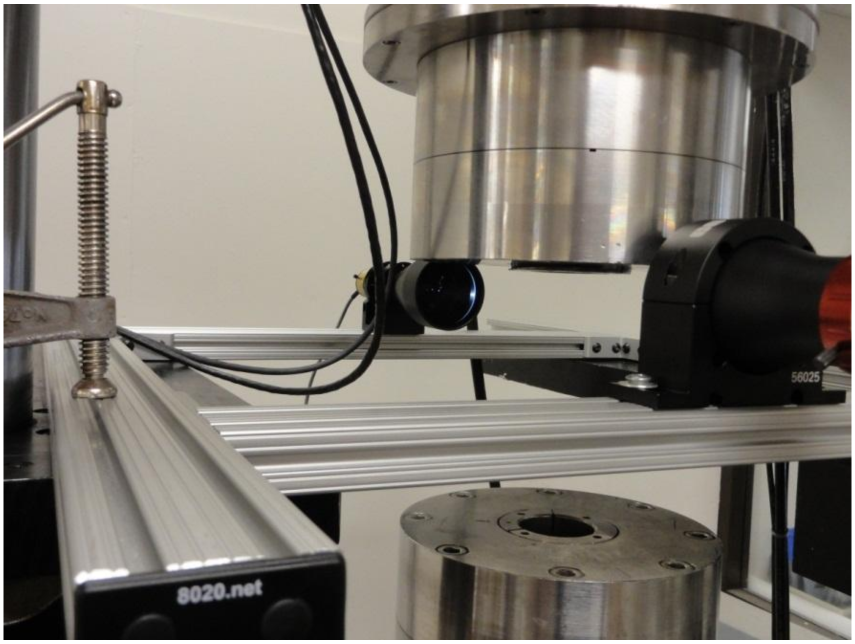

Figure 34: Critical Strain Test Setup

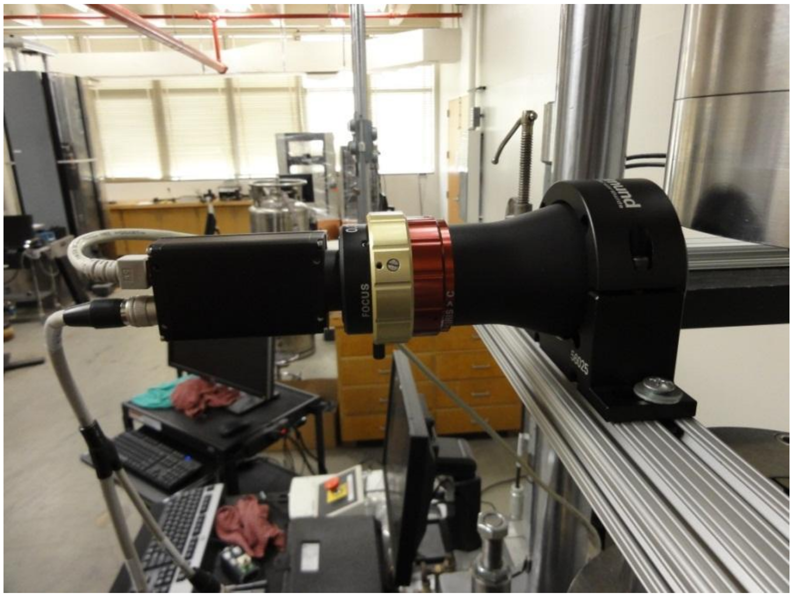

Figure 35: Basler Scout Camera and 0.36X Magnification Telecentric Lens

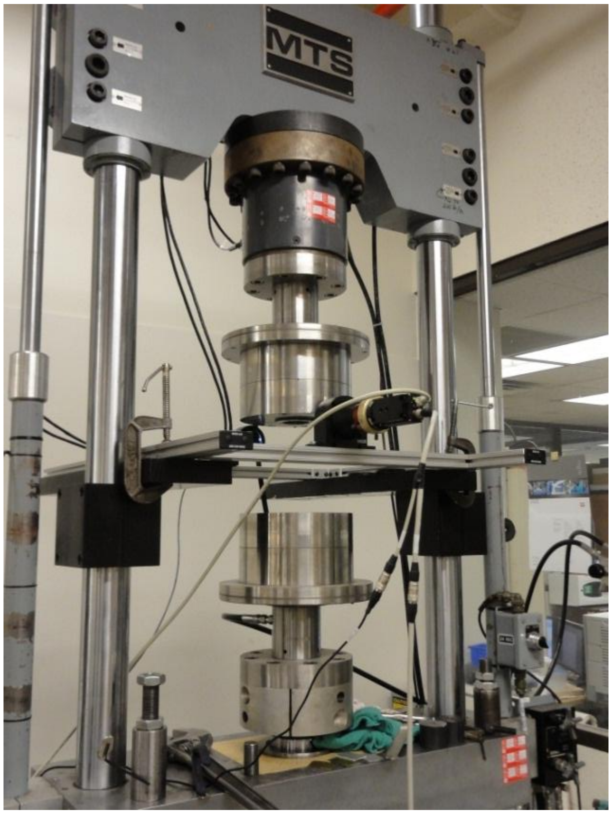

Figure 36: Test Frame

5.1.3 Procedure

Specimens were held in place by collets fabricated in the lab. The collets were designed to securely grip the specimens and prevent slipping. The camera system was mounted on a frame and placed so the sample was within the cameras field of view. A clip gauge was added to measure the strain within the gauge length. The specimens were strained at a rate of 0.0003 inches per second.

Data was acquired using National Instruments hardware and LabView software. LabView recorded the load, displacement, strain, and diameter during the test. The camera was configured to capture the instantaneous diameter at a rate of 4 frames per second. This rate supplied a sufficient amount of data and allowed proper synchronization between the camera and test frame measurements.

The goal of the critical strain segment of the research was to capture 5 acceptable tensile tests. A test was considered unacceptable if the specimen experienced any slip within the collets or if the necked region occurred outside the cameras field of view. Once 5 acceptable tests were completed the data was analyzed. The purpose of the critical strain sensitivity analysis was to see how different methods of locating the critical strain affected the value. This included fitting two parabolas through the data after the ultimate tensile stress (UTS) and fitting two line segments through the derivative of the data. In addition to testing the sensitivity of the various methods of analysis, a look into where to trim the data was also reviewed. A review of all test parameters was done using MATLAB to vary different parameters of the different algorithms. The results were reviewed and analyzed to find the best method for calculating critical strain as well as the critical strain for the denting pipe.

5.2 Laser Evaluation

The denting test requires the use of the Creaform ExaScan to extract dent profiles from the damaged pipe. An evaluation of the laser equipment is necessary prior to its use in the denting test. This ensures accuracy and reliability when using the dent profiles to calculate the DFDI. A major concern with using the laser scanner and the associated software, Pipecheck, is the need to scan the inner rather than the outer surface. During the denting process an indenter is used to create a dent in the pipe. The indenter must remain fixed within the dent so that the dent does not rebound. The profile of the dent is blocked by the indenter and thus inhibits the ability to scan from outside the pipe. This is the major reason for the evaluation of the laser equipment. For the system to be considered for the denting test, the scans of the inner and outer surface should give similar results with minimum error. Otherwise, the conclusions made from this project are not applicable to field conditions.

5.2.1 Specimen

To evaluate the laser scan software, the pipe shown in Figure 37 was used. The pipe is 125 inches long with a 24 inch diameter. There is a smooth dent located 77.5 inches from the upstream joint. The pipe is unique in that it has a spiral weld rather than a seam weld. The dent is located directly on the spiral weld. This pipe was selected based on its unique dent and convenience. Also, depending on the outcome of the current research, more tests will examine other denting conditions such as a pipe with a weld traversing a dent. This situation is unique and could cause problems with the scanning software. The selected pipe provides the same situation thus testing the sensitivity of the laser equipment to such a problem. The smooth dent is shown in Figure 38.

5.2.2 Equipment

The equipment used to extract the dent profile is the Creaform EXAscan 3D laser scanner shown in Figure 39. Creaform is a Canadian based company that develops, manufactures and markets cutting edge portable 3D measurement and analysis technologies. The EXAscan is one of many laser scanners offered by Creaform. The EXAscan is a high resolution and versatile scanner typically used for inspection and reverse engineering purposes. Blade met with the Creaform sales reps and engineers to select the optimal scanner and software for the purpose of this research.

The scanner projects a laser “X” on the surface of an object. Two cameras on the side of the scanner acquire images of the deformed “X”. Based on the deformation of the “X” the location of the surface is related to surrounding reflective dots. Each dot is recognized as the scanner takes images of the surface. Once a dot is located, it is correlated to a previously located dot. All dots are known relative to the origin of the scan. The origin is denoted by a magnetic marker that is placed on the pipe surface, as shown in Figure 40. The origin is at the center of the slot located at the back end of the marker.

Figure 37: Laser Scan Evaluation Specimen

The marker is a known pattern recognized by the scanner. The scanner will locate dots prior to recognizing the marker, but all dots are in unknown space until the marker is found by the laser scanner. At that point, each dot is correlated back to the origin using known dot patterns as references. The marker is magnetic and can be used to show flow direction. An operator in the field can measure from a known joint location and place the marker a specified distance from the joint. This allows for all axial and circumferential locations to correspond to a particular joint. This is typical of most field reporting procedures.

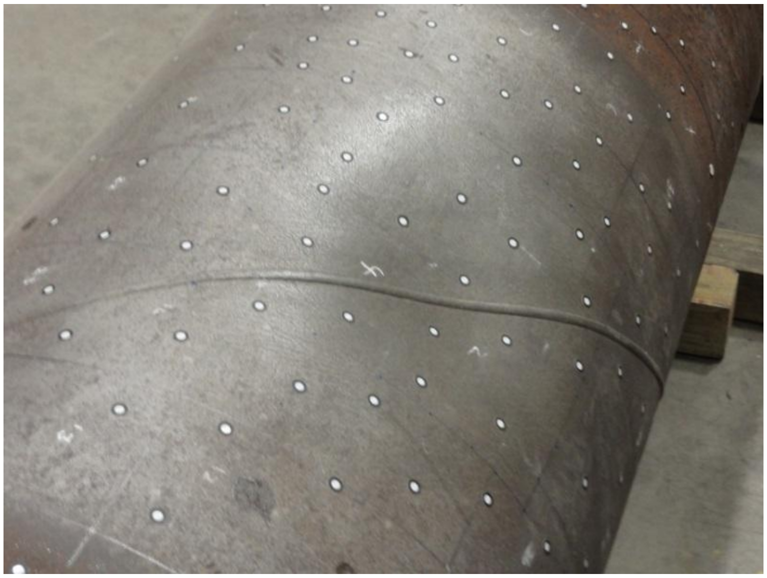

Figure 38: Smooth Dent on Spiral Weld

Figure 39: Creaform ExaScan 3D Laser Scanner

Figure 40: Creaform Marker

The scanner uses two software packages for data acquisition and analysis. The first is a general scanning program called VXelements. This is a general purpose scanning program that allows for the scan of any object. Once the scan is complete the information can be exported in many different 3D modeling file formats. This is ideal for reverse engineering purposes. For this research, the software used was Pipecheck. This is Creaforms pipeline integrity assessment software. It is essentially VXelements with various pipe modules built within the program. A screenshot of the software is shown in Figure 41. The pipeline software has two different modules, one for corrosion and the other for mechanical damage.

Only the mechanical damage package was required for the denting test. As a precautionary note, the current version of Pipecheck (Version 2.0 SR2 Build 1319), although sold as fully functional, was limited in its capabilities and required further development. As a result of this research much feedback was provided to Creaform in an attempt to improve the software, specifically for pipeline applications. Creaform is currently working on several features and improvements inspired by this research.

The purpose of the software was to extract dent profiles similar to the one shown in Figure 42. The extracted data was used to calculate strain and consequently the DFDI for the dent. As expected, the maximum strains will occur at the maximum dent depth. This makes finding the maximum depth value vital to the accuracy of the DFDI analysis.

The difficulty with the laser equipment was deciding how much of the pipe to scan and at what resolution. The amount of scanning was limited by the capabilities of the laptop as well as time constraints for scanning. The laptop used to operate the scanning equipment was the HP EliteBook 8570w. The computer was equipped with an Intel Core i7 2.30 GHz processor with 8 GB of RAM. It was purchased with Windows 7 Professional and a 64-bit operating system installed. Pipecheck required a great deal of memory and computing power during scanning.

In addition to the computer and scanner, the field pack was purchased from Creaform. As the name suggests, the field pack was designed to use the laser equipment in the field. There are several features the field pack offers that proved benefits during the scanning of the ID surface. The field pack included all the equipment shown in Figure 43 . The most important equipment for the scanning process was the tablet and the 20 ft firewire cable. The tablet allowed complete control and visualization of the scan while inside the pipe. The extended cable provided the length required for using the scanner in the center of the pipe.

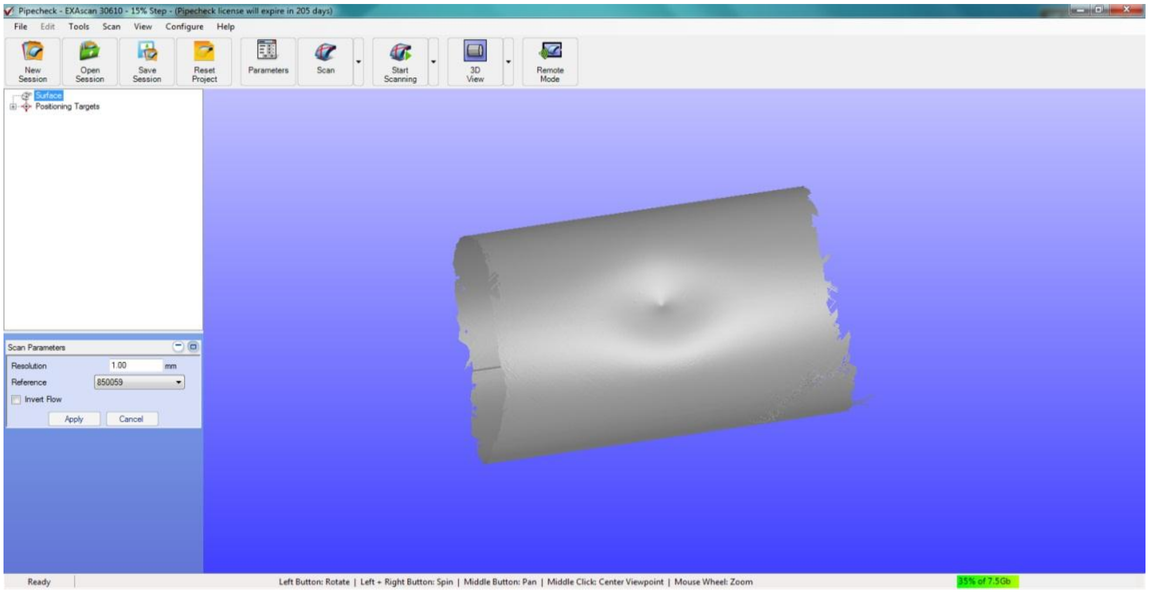

Pipecheck - EXAscan 30610 - 15% Step - (Pipecheck license will expire in 205 days)

Resolution 1.00 mm

Reference 850059

☐ Invert Flow

Ready

Left Button: Rotate | Left + Right Button: Spin | Middle Button: Pan | Middle Click: Center Viewpoint | Mouse Wheel: Zoom

35% of 7.5Gb

Figure 41: Pipecheck Software

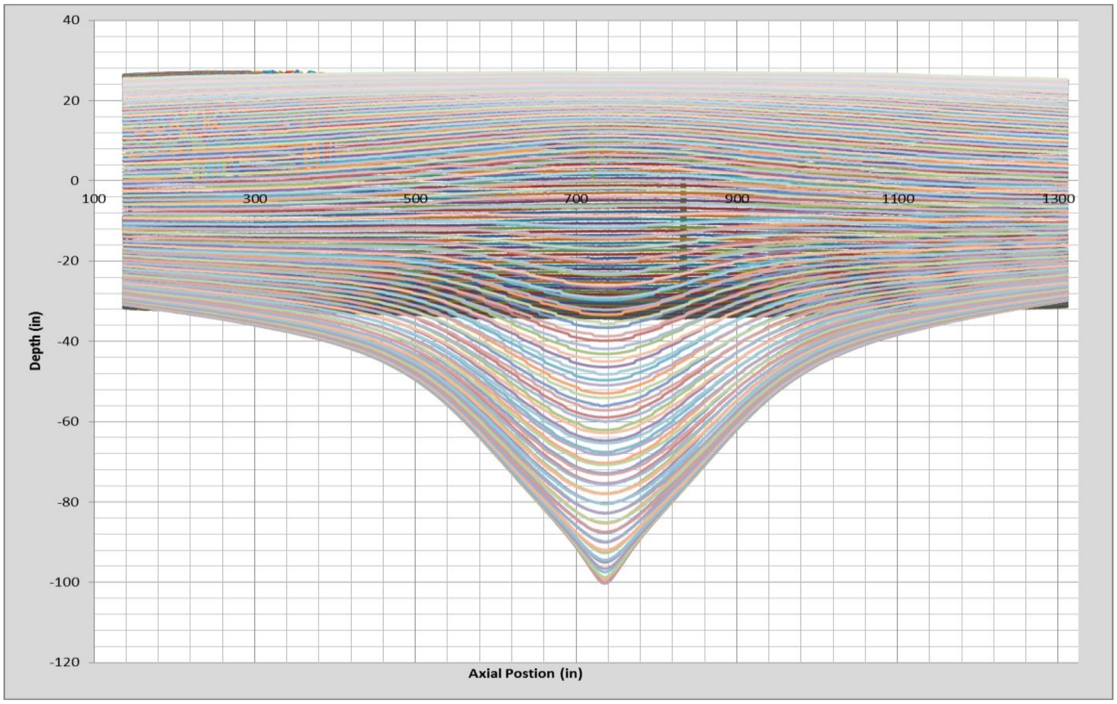

Figure 42: Dent Profile Extracted from Pipecheck

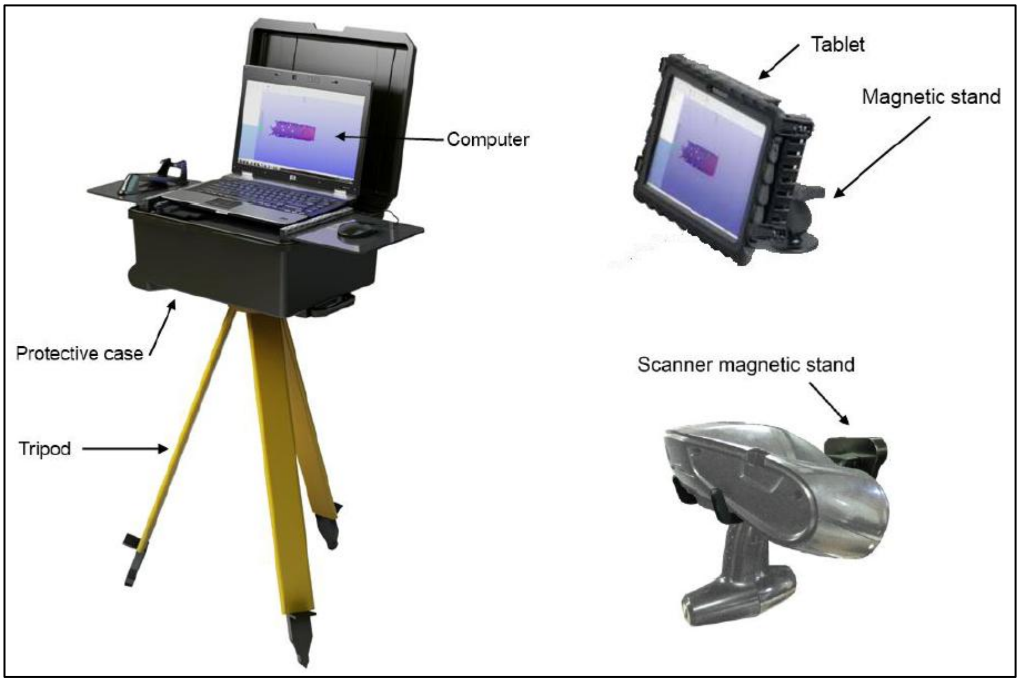

Figure 43: Creaform Field Pack

5.2.3 Procedure

The basic goal of the laser evaluation is to scan a pipe at varying resolutions, areas and surface types to see how the dent profile is affected. The optimum scanning resolution and area is found when the acceptable amount of accuracy is balanced by computer capability and time restraints. To investigate the need for a full 360 degree scan, the pipe specimen was scanned at 1.00 mm resolution 1.00 m along the pipe axis centered over the dent. Another scan was made covering only 180 degrees of the pipe to compare to the 360 degree scan.

A third scan was made similar to the 360 degree scan with the exception that a 1 ft square section centered on the dent was left unscanned. The unscanned region was then scanned at a 0.20 mm resolution and merged with the previous scan. The goal of this scan was to investigate the possibility of merging as well as the effect of combining resolutions. The final OD scan was made by scanning the pipe at 1.00 mm resolution and using the built in high resolution button on the scanner to scan the dent area. All 4 scans were analyzed and compared.

As discussed previously, the indenter makes it impossible to scan the outside surface of the pipe. That is why the fifth scan was 360 degrees at 1 m along the pipe axis on the inside surface. This allowed for comparison between the inner and outer surface scans. The final scan for the laser evaluation was another scan of the inside surface at 0.50 mm rather than 1.00 mm. This provides a direct comparison between the two resolutions. The scanning procedure was developed based on the EXAscan and Pipecheck manuals, Creaform training, and experience. The majority of the procedure was developed using trial and error to find the optimum scanning methods. The following procedure is for general scanning. The procedure is heavily relied on during the denting test.

Scanning Surface Preparation

The scanning surface was cleared of all dirt and debris. The resolution of the scanner is high enough to pick up any large pieces of debris or texture from a severely rusted surface. The laser evaluation pipe was sandblasted along a 1 m section 360 degrees around the pipe centered on the dented region. This exposed the bare metal and rid the surface of all rust texture and debris. Alcohol was used to wipe the surface clearing away any dust left. The denting pipe was not sandblasted but the interior rust was removed with a grinder and wire brush attachment.

Reflective Dot Application

The reflective dots act as fixed points used to triangulate the position of the laser scanner and the surface scan. The dots were placed at random locations 2 to 3 inches from one another. Dots are recognized by the scanner but depth measurements are not taken at their locations. It is for this reason that dots were not placed on regions of interest. For example, a dot placed on the deepest point of a dent would prevent the laser from reading the deepest section. It is very important to have at least 3 dots visible by the two cameras on the scanner. Without 3 points, the laser cannot triangulate and will stop taking data. Dots may be added any time during a scan. If the scanner is unable to read data because the dots are spread out, a dot can be added to span the gap. Dots should not be removed or moved during a scan. If a dot falls off the surface, simply remove the loose dot and continue scanning. The scanner recognizes there should be a dot but will ignore the fact that it is missing.

Scanner and Field Pack Assembly

To avoid potential problems with the scanner, the process for preparing the scanning equipment was consistent as suggested by Creaform. First, the laptop was booted up. Next, the dongle carrying the Pipecheck license was inserted into an available USB port. The scanners express card was then inserted into the appropriate slot. The firewire cable and power cable were then connected to the express card. Finally, the scanner was connected to the other end of the firewire cable. Once the scanner is connected, Pipecheck was opened. If Pipecheck is opened prior to connecting the scanner a warning message appears. This only deactivates the scanning options in Pipecheck. Pipecheck can run without the scanner attached.

The tablet used software called SplashTop to communicate to the laptop. The program worked by generating a wifi signal from the laptop. The tablet connected to the wifi signal and shared screens using the connection. Pipecheck has a built in “Remote Mode” that was used extensively during every scan. It allowed the operation of Pipecheck from the tablet. The rest of the field pack was not necessary for lab conditions. For more information regarding the setup of the field pack the reader is referred to the Pipecheck User Manual.

Scanner Calibration

The EXAscan is a high percision instrument and like all precision instruments they must be calibrated regularly. In the case of the EXAscan it was recommended that calibration occur before each day of scanning. It was also recommended that calibration occure after significant changes in environment or if the scanner is bumped or dropped. Each scanner comes with a calibration plate like the one shown in Figure 44. Using the calibration window (Figure 45) as a guide, the calibration was completed by moving and rotating the scanner to various predetermined postions.

The laser “X” was kept in the center of the plate. The program beeped when the sanner was in the correct position. The window then showed the next location for the scanner. The sequence required 10 locations directly above the plate at different elevations as well as a tilted position to the back, front, left and right. The plate has a known pattern of dots unique to a particular scanner. The plate is very sensitive and was kept in a safe location at all times.

Figure 44: Calibration Plate

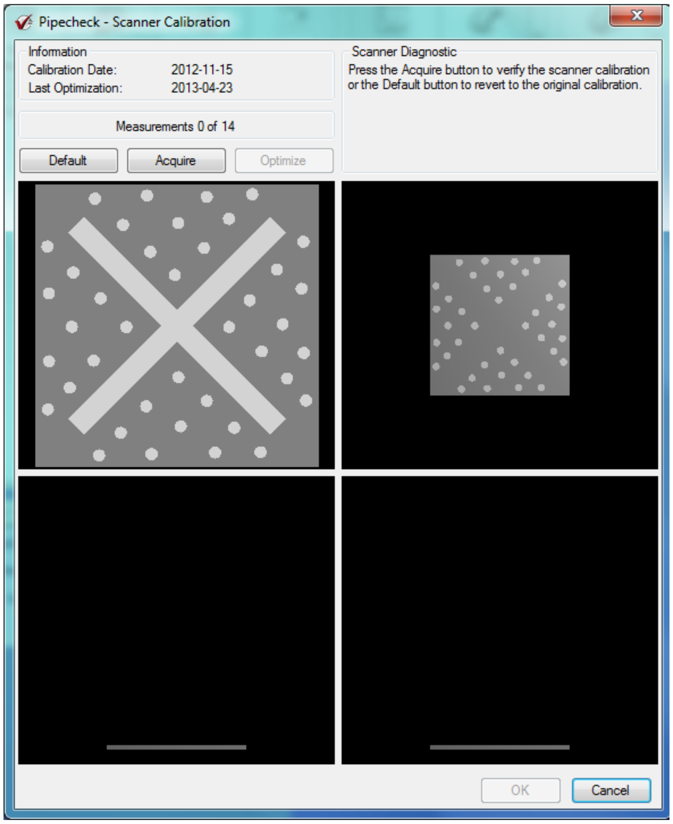

Information

Calibration Date: 2012-11-15

Last Optimization: 2013-04-23

Measurements 0 of 14

Scanner Diagnostic

Press the Acquire button to verify the scanner calibration or the Default button to revert to the original calibration.

Figure 45: Scanner Calibration Window

Scanner Configuration

There are two parameters associated with the function of the scanner. These were laser power and shutter speed. Different environments and lighting require different settings. The configuration can be saved and loaded for other sessions of Pipecheck. To optimize the configuration trigger on the scanner was pulled while aiming at the target surface. When the vertical and horizontal indicators on the sides of the configuration window were within the reliable section, the scanner was optimized. The power of the laser can be increased to make it visible on the surface of the pipe. This simplified the scanning process by providing a noticeable “X” on the surface where the scanner was taking data.

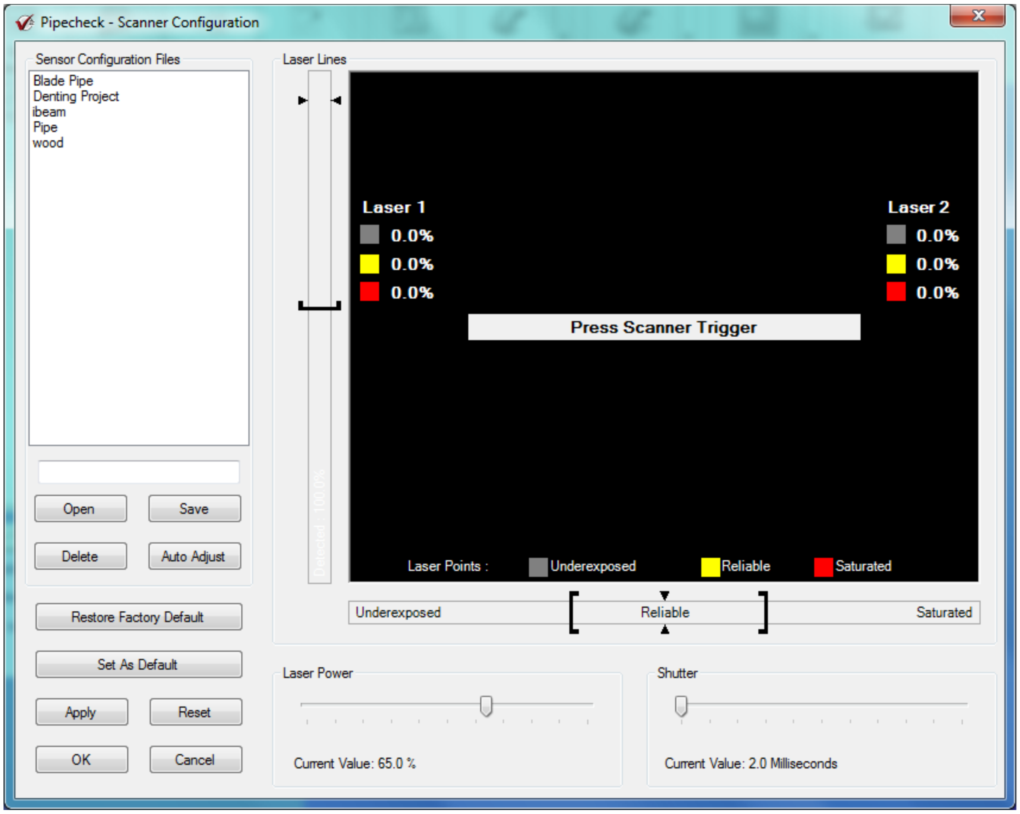

Blade Pipe
Denting Project
ibeam
Pipe
wood

Laser 1
⬛ 0.0%
🟨 0.0%
🟥 0.0%

Laser 2
⬛ 0.0%
🟨 0.0%
🟥 0.0%

Laser Power: Current Value: 65.0 %

Shutter: Current Value: 2.0 Milliseconds

Figure 46: Configuration Window

Parameters

Parameters are used to tell the program the type of pipe under inspection. The parameters included the nominal diameter and wall thickness of the pipe. Other optional information included pipe name, pipe owner, and inspector name. This information is used in the reporting functions of the Pipecheck software. The most important parameter was the nominal diameter and wall thickness. These values were used to generate the reference cylinder used to take depth measurements. This influenced the value of the depths and was made as accurately as possible.

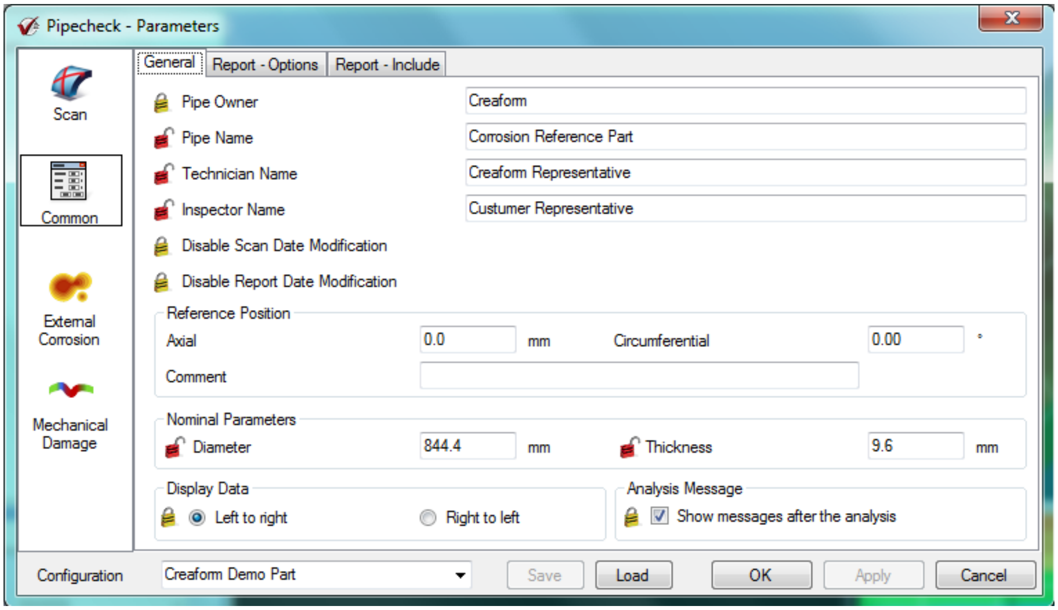

Pipe Owner: Creaform
Pipe Name: Corrosion Reference Part
Technician Name: Creaform Representative
Inspector Name: Custumer Representative
Disable Scan Date Modification
Disable Report Date Modification

Reference Position
Axial: 0.0 mm
Circumferential: 0.00 °
Comment:

Nominal Parameters
Diameter: 844.4 mm
Thickness: 9.6 mm

Display Data
● Left to right ○ Right to left

Analysis Message
☑ Show messages after the analysis

Configuration: Creaform Demo Part

Figure 47: Parameters

Remote Display

As previously noted, the tablet was used to monitor the scan while inside the pipe. This required connecting to the Pipecheck software using the "Remote Mode" button located in the top menu ribbon. The function changed the Pipecheck software so it could be controlled from the tablet. The tablet was first connected to the wifi signal generated by the SplashTop software on the laptop. Once connected, the "Remote Mode" was active and the tablet was placed inside the pipe with the magnetic stand.

Creaform Arrow

Before scanning, the Creaform marker was placed at the desired origin location. The marker acts as the start of the scan and decides the location of the origin for all measurements. The marker was placed a known distance from a weld or joint. It was also placed on or near a weld for reference. For example, during the denting test the marker was placed on the weld so that all degree measurements were taken from the seam weld location.

Scanning

Scanning was very simple. The key to scanning was monitoring the distance of the scanner from the pipe surface. Too close and the cameras could not pick up enough dots for referencing and too far away limited the ability of the scanner to see the "X". The "X" was slowly moved over the surface of the pipe. As the pipe was scanned, the surface was generated in the Pipecheck software in real time. Any missed sections could be seen on the screen and corrected by rescanning the area. While the "X" is moving across the screen, a line of missing data was formed where the intersection of the laser lines met. This is because data is not taken at the intersection point. For a fast and reliable scan, the scanning paths were overlapped to clean up any missing data.

An issue uncovered during the scanning process was the scanned surface getting in the view of the unscanned areas. This problem occurred because Pipecheck is designed to only scan the outer surface of a pipe. VXelements has functions that handle this issue because it was intended to scan a variety of objects. The issue was raised with Creaform and will be rectified in a later version.

Mechanical Damage and Data Export

After the scan was complete, the mechanical damage software was used to generate depth data. The pipe parameters were previously entered. Therefore, the only step that was required was going to the mechanical damage module and press the analyze button. The software then generated a reference cylinder and created a depth profile of the entire scan. The software recognizes mechanical damage and separates dents into different features. To export the depth data the dent feature on the left hand menu was right clicked. The export data option was selected along with the “All Pipe” option. This exported all the depth data to a csv file. While investigating the software, it was found that the data could not be organized or sorted. After discussing this issue with Creaform, a macro was developed by Creaform and that imported the csv file and organized the depth data into a grid designated by the user. The now exported and sorted depth data was imported into Excel and plotted using Excels plotting functions.

5.3 Denting Test

The denting test was designed to evaluate the applicability and accuracy of the DFDI method of pipe inspection. The goal of the test was to evaluate the use of the DFDI approach to estimate the depth at which a crack would form within the dent region. If the crack formed when the DFDI was equivalent to 1 then the assessment method was verified and considered accurate. Otherwise, the method did not accurately estimate the crack formation and should be reassessed.

5.3.1 Specimen

The specimen selected for denting was picked from pipe already available. The 34 inch diameter pipe was cut to a length of 134 inches. 12 inches were cut from one end of the pipe to form two 6 inch reinforcement rings. The rings were used to reinforce the ends of the pipe to prevent them from collapsing. The final length of the specimen was 122 inches. This length was selected so that the stress distribution was uniform throughout the pipe. This is accomplished by providing 1.5D of pipe on each side of the denting location. The diameter of the pipe was not important because different diameters will eventually be required for testing. This project is intended only to verify the method and justify more tests. An image of the pipe is shown in Figure 49.

5.3.2 Equipment

The denting setup is shown in Figure 51. The frame of the setup consisted of two 20 ft W12x106 columns spaced at 6 ft. The header beam was a 7.27 ft W24x103 with a W12x106 diaphragm located at the center of the beam. According to the FE analysis, the maximum required load was approximately 41 kips needed to reach the maximum dent depth. Based on this information a 50 kip MTS actuator was selected.

To monitor the depth of the dent under the indenter, a 2 inch LVDT was used. The decision to use an external LVDT rather than the displacement recorded by the actuator was based on the error associated with deflections in the actuator itself and other components of the test frame. An accurate reading of the travel of the indenter was made by placing an LVDT inside the pipe directly under the dent location. A second LVDT was placed in the horizontal position to record the out of roundness of the pipe. A 2 inch LVDT was used in this direction as well. The choice for a 2 inch LVDT was based on the need for high resolution. The required travel for the vertical LVDT was approximately 5.1 inch. Instead of using a longer LVDT, a higher resolution LVDT was used and reset at each step.

The research is focused on unconstrained plain dents. Complications such as gouges are ignored for this research due to the complexities of the problem. To create a smooth dent a 2.5 inch diameter sphere was used as an indenter. A fixture was fabricated in the lab to hold the sphere in place and attach to the actuator. Figure 48 is an image of the indenter.

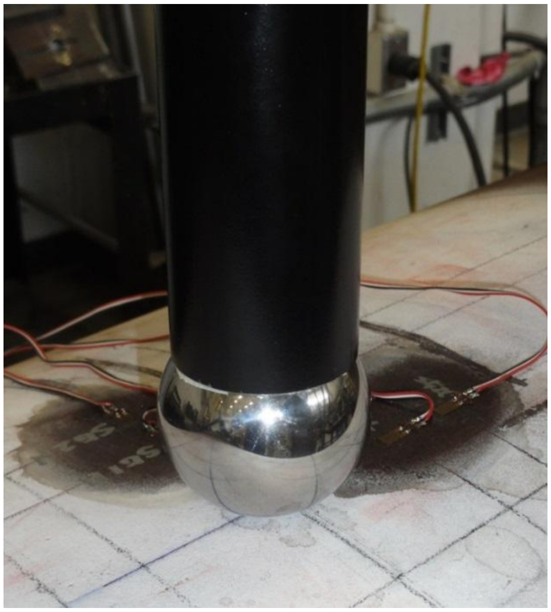

Figure 48: Sphere Indenter

Figure 49: Denting Pipe

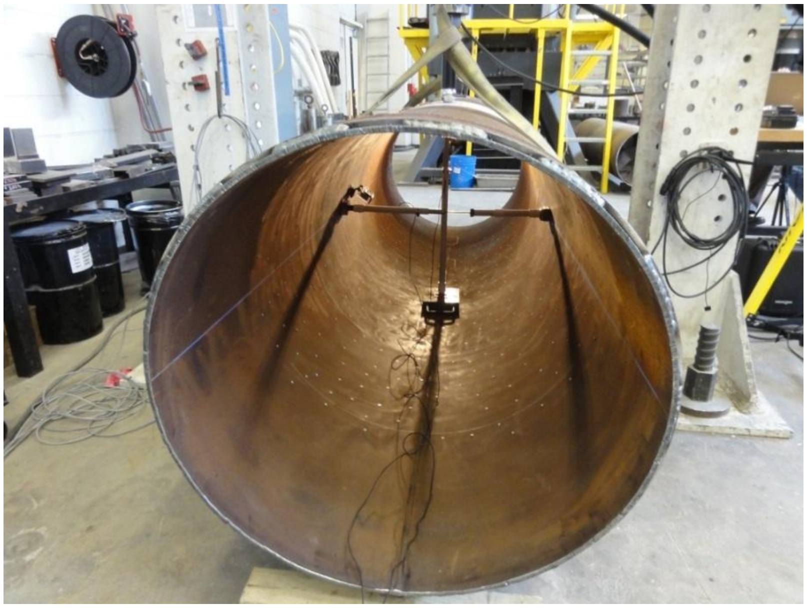

Figure 50: LVDT Placement

The pipe was inspected before and after denting using two methods of crack detection. The first was magnetic particle inspection (MPI). This method involved applying a metallic powder over the surface of the pipe. A yolk, shown in Figure 52, applied a current to the pipe between the two contact points. If there was a crack, a magnetic field formed between the two surfaces of the crack. The magnetic field attracts the metallic powder creating a line on the surface of the pipe. The second method was the dye penetration test (PT). The surface of the pipe was cleaned and soaked with a dye. After 5 minutes the dye was wiped from the surface with a clean cloth. This removed the dye from the surface of the pipe while leaving the dye trapped within the crack. A developer was then applied to draw the dye out from the crack. Similar to the MPI method, a line was left on the surface of the pipe where the dye was extracted from the crack. MPI was used to check the untested pipe for cracks prior to denting. PI was used to check for cracks after the denting was complete. The dye penetration chemicals are shown in Figure 52.

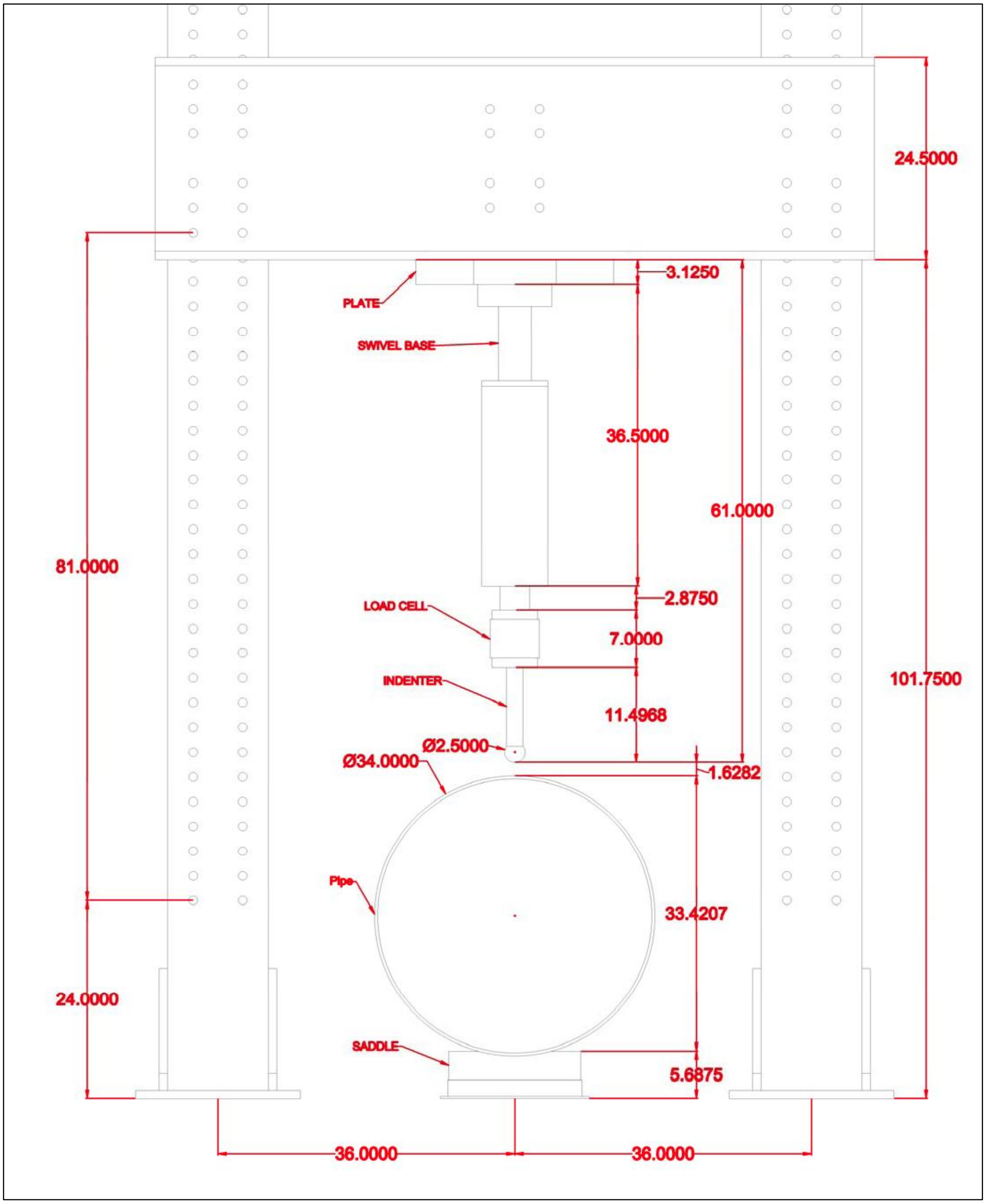

Figure 51: Denting Setup

Figure 52: MPI and Dye Penetration Test

5.3.3 Procedure

The procedure for denting the pipe was completed in 5 denting intervals of 3% OD. Table 7 shows the 5 steps taken during denting and the corresponding dent depths calculated based on the 34 inch pipe diameter. Each step was 3% of the OD or 1.02 inches. Due to an error with the placement of the vertical LVDT during the first step, the actual dent depths vary from the target dent depths. This has no effect on the outcome of the results but does require some adjustment to the FE analysis.

At each denting step, a scan of the dent was required using the laser scanner. The procedures for scanning were discussed in section 5.2 and therefore will not be discussed in this section. After each scan, the profiles were inspected for holes or other anomalies in the data. If the scan was error free the process was repeated for the next denting interval. An outline of each step taken during the denting process is listed below.

Table 7: Dent Depths

Step	Target Dent Depth (in)	Actual Dent Depth	Interval (in)
0%	0.00	0.000	0.000
3%	1.02	1.123	1.123
6%	2.04	2.143	1.020
9%	3.06	3.162	1.019
12%	4.08	4.183	1.021
15%	5.10	5.203	1.020

1. Inspected dent region for signs of cracking
2. Placed vertical and horizontal LVDT inside pipe at appropriate locations
3. Adjusted placement of LVDT's to ensure enough travel for dent displacement
4. Placed lighting and video camera inside pipe to monitor dent region for cracking
5. Recorded the starting LVDT readings for both the vertical and horizontal directions
6. Began denting process
7. Stopped denting when LVDT reached appropriate value
8. Removed lighting, camera and LVDTS
9. Scanned 360 degrees and 0.5 m in both the upstream and downstream directions
10. Exported data from Pipecheck and generated dent profile in excel
11. Inspected profile for jumps caused by holes in the scan
12. Repeated procedure for next denting interval

Data was continuously acquired during the entire denting process. Data acquisition (DAQ) is the process of measuring physical phenomenon with a computer. Data acquisition for this project was accomplished using a National Instruments (NI) DAQ device. This device recorded data from the actuator, LVDT's and strain gauges. The loading intervals are shown in Figure 53. The stretch of time shown between each step represents the time taken to adjust testing equipment and to scan the inner surface. Each scan took roughly 1 hour to complete. The long time period shown between the 6% and 9% steps represents the test running overnight. The test had to run overnight to prevent the dent from rebounding. For this project the dent is considered constrained and consequently must be restrained from rebounding. This requires the indenter to remain fixed at each depth interval. This is why there is a large span of time between the 6% and 9% steps.

The loading was designed to represent an indenter slowly denting the pipe over time. This is representative of a pipe settling onto a rock. For testing purposes, this type of loading is considered static. To create static loading conditions, the same rate was used to simulate static loading for a standard tensile test. This rate is presented in ASTM E8 and is a rate of 0.00057 in/sec or 0.034 in/min. This means that each denting step required 30 minutes to travel the necessary 1.02 inches.

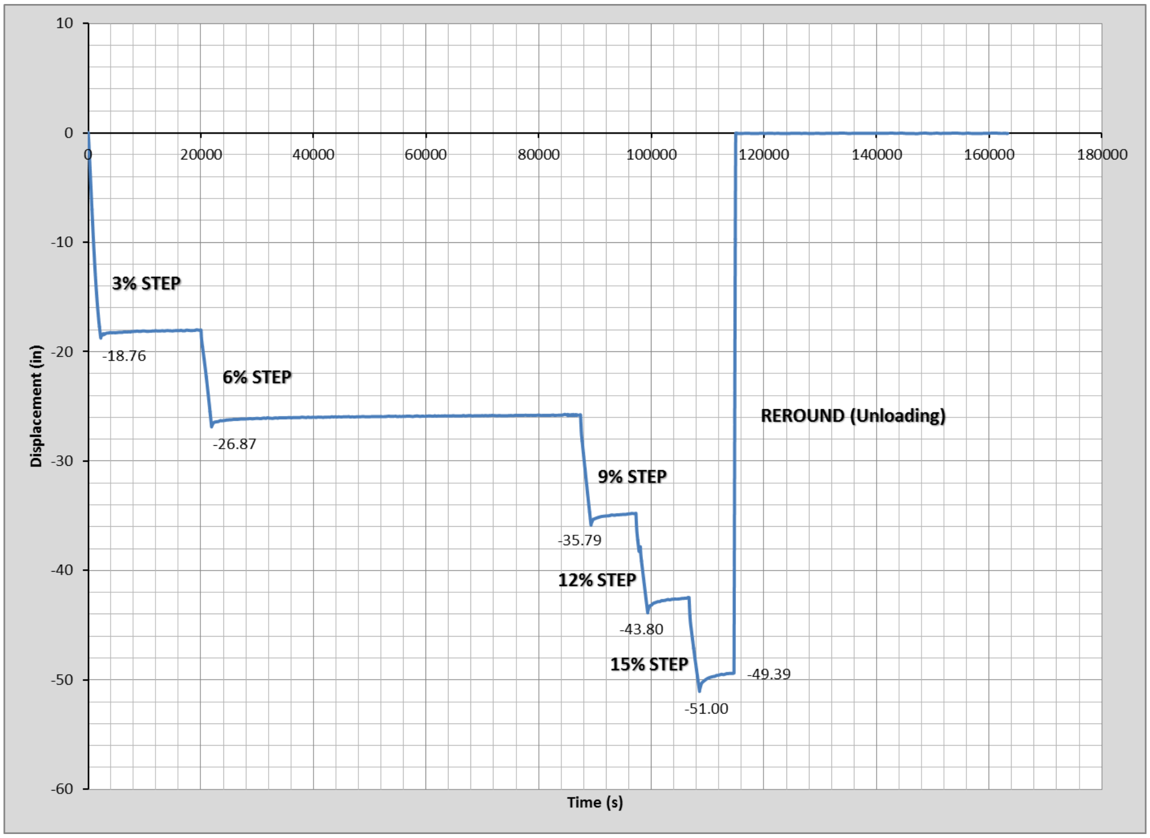

Figure 53: Loading Plot for Denting Test

6 RESULTS AND DISCUSSION

6.1 Critical Strain

Critical strain was the target material property used for the DFDI approach. It is essential that the results from the critical strain analysis are accurate and reliable. As discussed previously, the critical strain is found from either the stress-strain or slope-strain curve. The stress-strain curve for the 5 pipe specimens are shown in Figure 54. The results show good agreement between the 5 samples. There is minor scatter near the failure stress (FS). Figure 55 is a plot of the data beyond the ultimate tensile stress (UTS) for each sample. This was the data used to calculate critical strain. The rest of the data was unnecessary and ignored throughout this section.

6.1.1 Stress-Strain Approach

The basic theory states that the critical strain lies beyond UTS but gives no indication as to how it is located. Fischer et. al. (1999) stated that the stress-strain data beyond UTS traces a parabolic path until it reaches critical strain at which point the data follows a secondary parabola. Based on that idea, it seemed appropriate to find two parabolas that best fit the data before and after critical strain. A simple algorithm accomplished this task by selecting critical strain points and choosing the critical strain point at which a fitted parabola on each side minimized the overall residuals.

The first attempt at such a method used MATLAB’s polyfit and polyval functions. The program started at UTS and selected a data point. Polyfit was used to fit a parabola before and after the selected point. The residuals were then calculated and compared to the current minimum. The program cycled through successive data points until the failure stress was reached. After completing all cycles, the data point related to the minimum sum of residuals was chosen as the critical strain. An example of the results from the program is shown in Figure 56. The two parabolas do not intersect. This occurred with each data set because the parabolas are not forced to intersect.

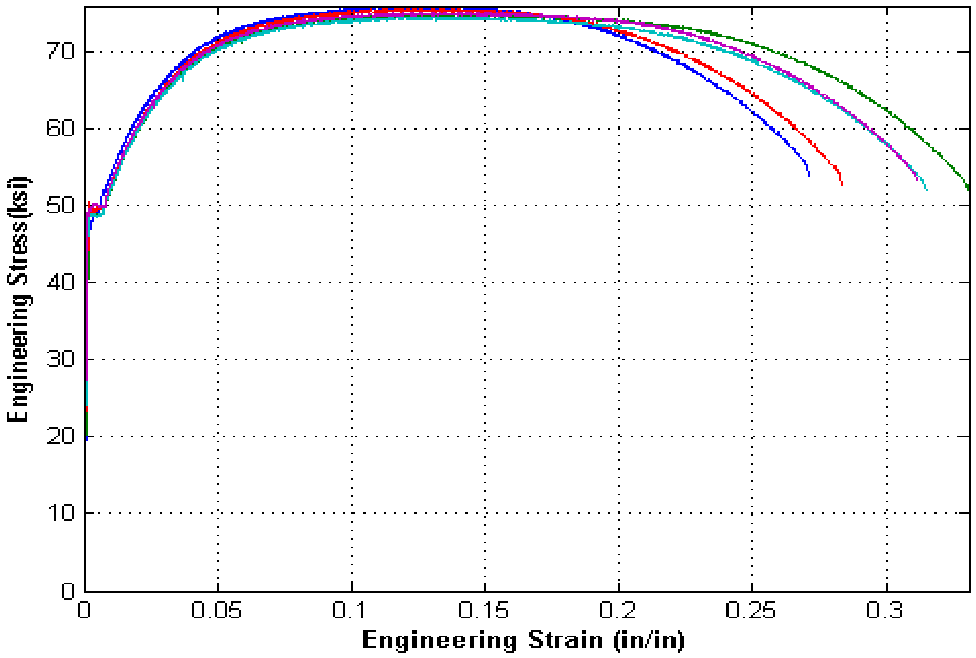

Figure 54: Pipe Sample Stress-Strain Curves

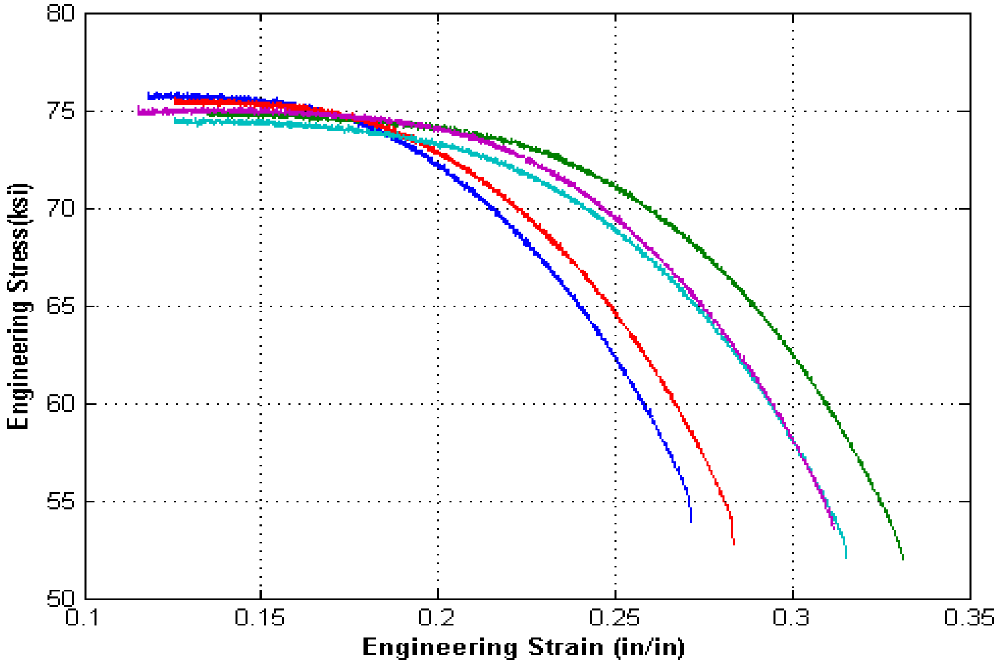

Figure 55: Pipe Sample Stress-Strain Curve Beyond UTS

An alternative approach was to constrain the parabolas so that they intersect. This was done by taking the equation for a parabola, $\mathrm{y} = \mathrm{A}\mathrm{x}^2 + \mathrm{B}\mathrm{x} + \mathrm{C}$, and setting the constant C equal to the current data point. This forced both parabolas to intersect at the current value for critical strain. The parabolas were fitted to the data on the left and right hand sides of the data point. Figure 57 is a plot of the results using the same data set as Figure 56. The critical strain results for the intersecting and non-intersecting parabolas are 0.1816 and 0.1976, respectively. The critical strain value for the non-intersecting parabolas is approximately 8% higher than that for the intersecting parabolas. This confirms that the two methods are not equivalent and only one should be selected for the evaluation process.

The intersecting parabolas are a more appropriate choice for calculating critical strain. The kink in the stress-strain data represents the transition from one parabola to another. The kink requires the two parabolas to join at the critical strain value. It was for this reason that the constrained parabola method was selected. The non-constrained method does not agree with the theory and therefore was disregarded.

When investigating how to calculate critical strain, it became apparent that the start and end locations for each method would influence the results. A sensitivity analysis investigating the effects of these parameters was conducted. The critical strain was calculated using the parabola method while the data used in the algorithm was trimmed by 60% and 10% from the UTS and FS ends respectively. Figure 58 shows approximately how much data was trimmed. The variation in the amount of data trimmed for each side of the curve is a result of the density of the points. The UTS end has a much greater number of data points unlike the FS end. 60% appeared to be a sufficient amount of data to observe the effects at the UTS end whereas 10% was more appropriate for the FS end.

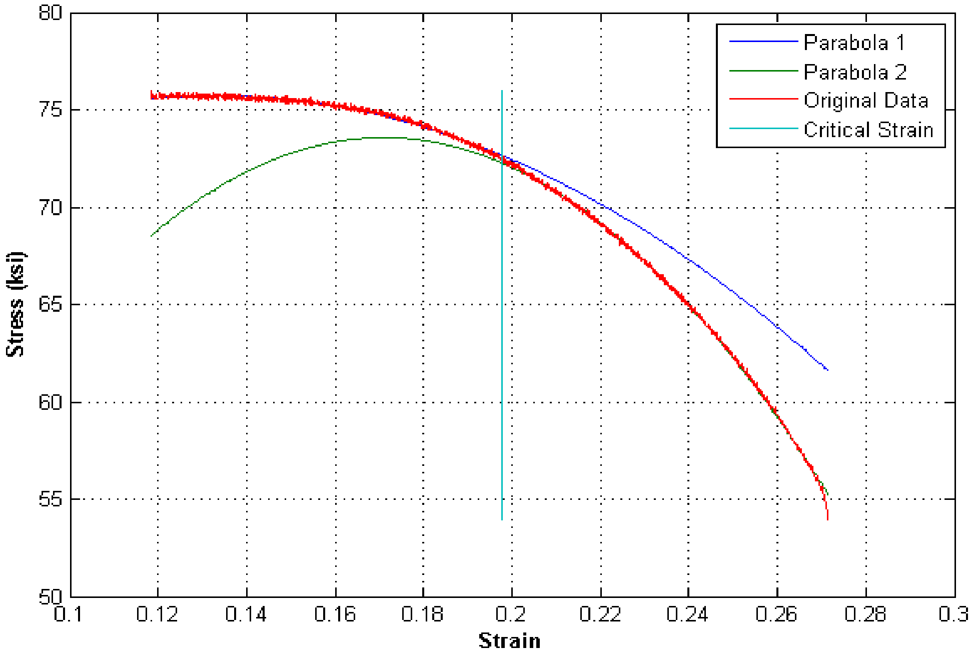

Figure 56: Critical Strain Results for Non-Intersecting Parabolas

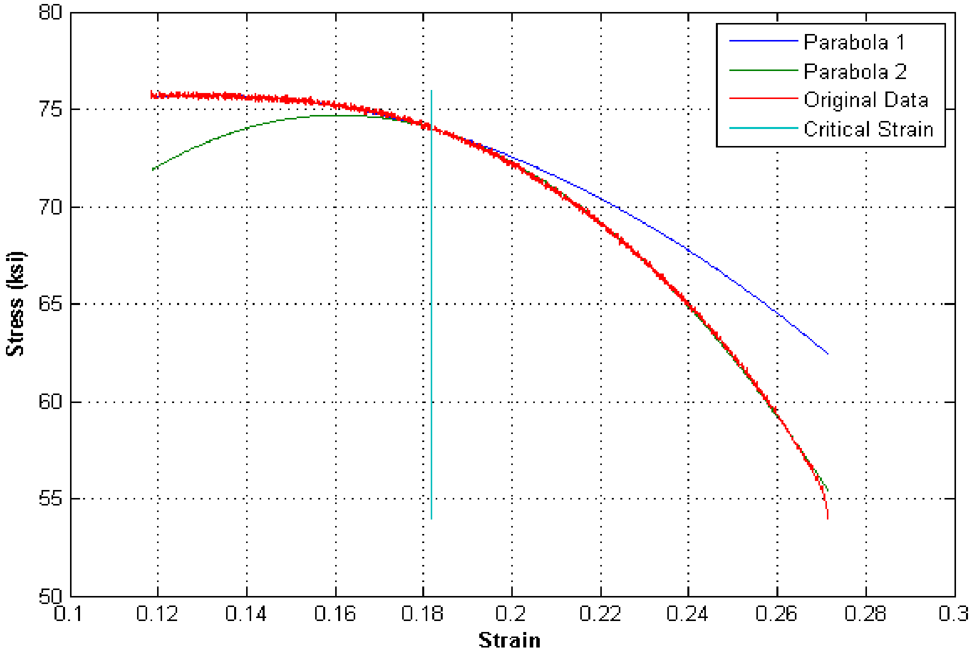

Figure 57: Sample Calculation for Intersecting Parabolas

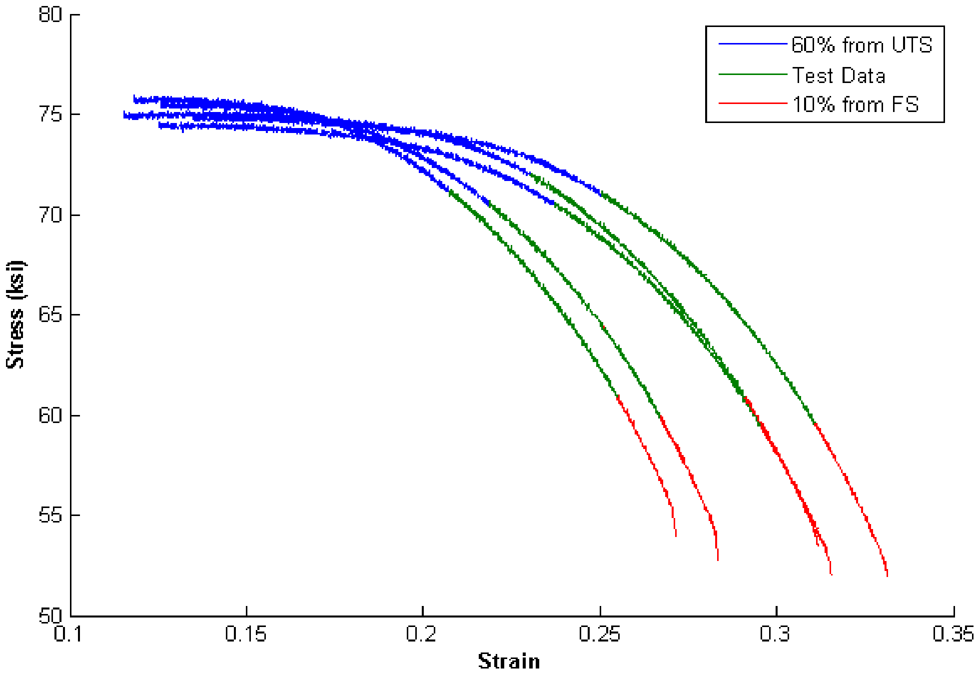

Figure 58: Trim Locations

The UTS end of the data set was investigated first. The program looped through the data at 2% increments from 0%-60%. The amount of time required for computing the critical strain limited the step size of the calculations. At each interval the critical strain was recorded. The results are shown in Figure 59. The plot shows that moving the starting point further away from UTS has the effect of increasing the calculated critical strain. It can be seen from the stress-strain plot that samples D2, D4, and D5 follow a similar path. The plots have a longer flat region at UTS than samples D1 and D3. D1 and D3 follow a different path that appears parabolic beginning at a point closer to UTS. The variation in stress-strain curves can be seen in the critical strain values of Figure 59. D2, D4, and D5 have similar trends whereas D1 and D3 follow a different trend. The results show that critical strain continuously increases as the starting point moves further away from UTS. There is not a point where the data converges to a particular value. This is not ideal when attempting to create a consistent method.

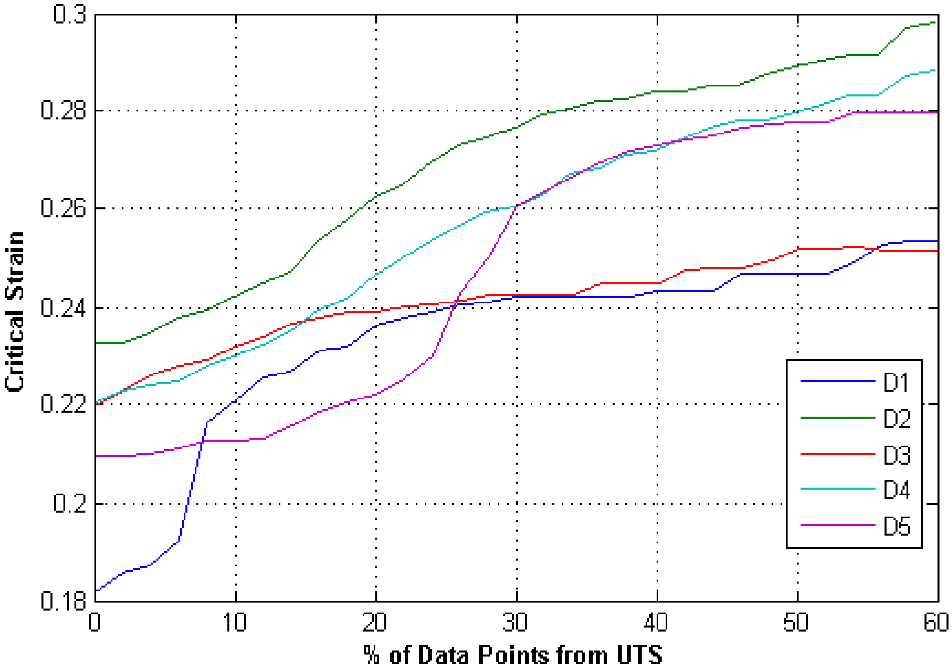

Figure 59: 60% Data Trimmed at UTS End

Figure 60 shows the relationship between critical strain and trimming the data from the failure end of the curve. The results show a trend inverse from the UTS results. The value of the critical strain tends to decrease as the amount of data trimmed increases. The two plots are similar in that the samples are grouped as before. D2, D4, and D5 show similar curves and D1 and D3 start at different locations but tend to converge. Unlike the UTS end, the FS end does not appear to have a major effect on the critical strain value. The change in critical strain appears relatively steady. There is not a linear section on the FS end that could possibly interfere with the fitting process.

The results of both plots appear sensitive to the shape of the stress-strain curve. This is intuitive since the algorithm uses the geometry of the curve to find critical strain. A surface plot of sample D1, Figure 61, shows the combined effects of reducing the data on each end of the set. The data was trimmed up to 30% on each end. The results agree with the previous plots. What is interesting is the jump that occurs at around 28% from

UTS and 15% from FS. Prior to these limits the surface is relatively smooth. The jump is caused by excessive trimming on the FS end of the curve. The remaining data forces the critical strain value to the intersection of the flat and parabolic regions. Figure 62 shows this location for sample D1. This could represent an ideal cutoff point for the algorithm.

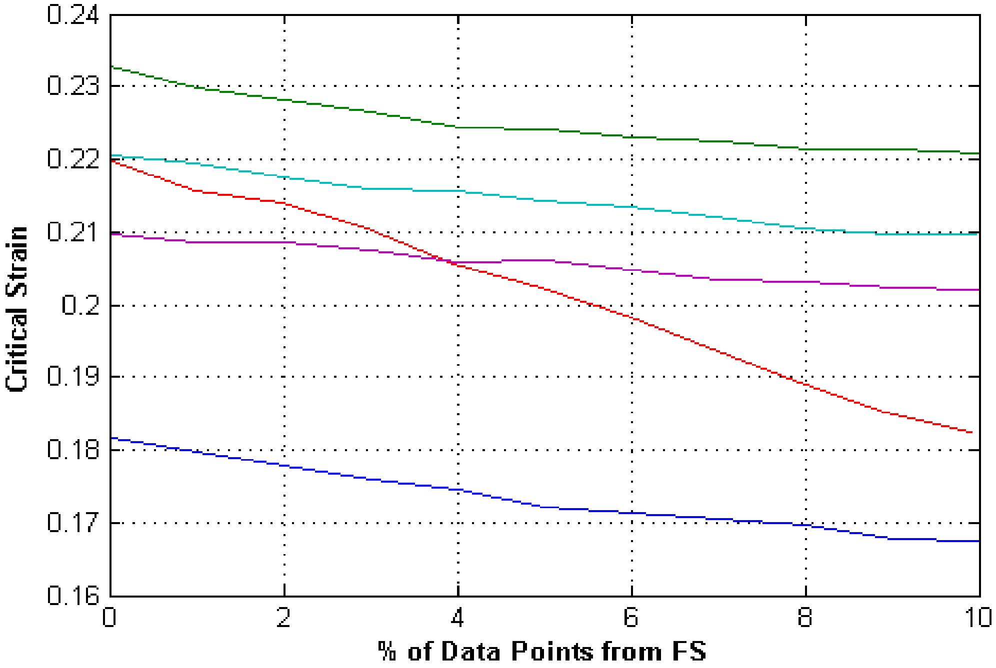

Figure 60: Data Trimmed at Failure End

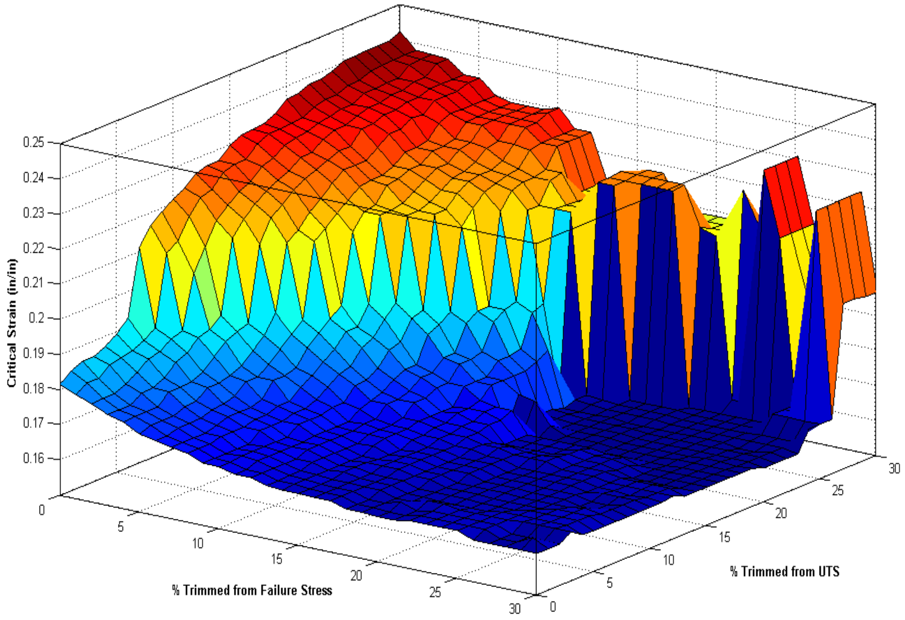

Figure 61: Surface Plot of D1 Critical Strain Values

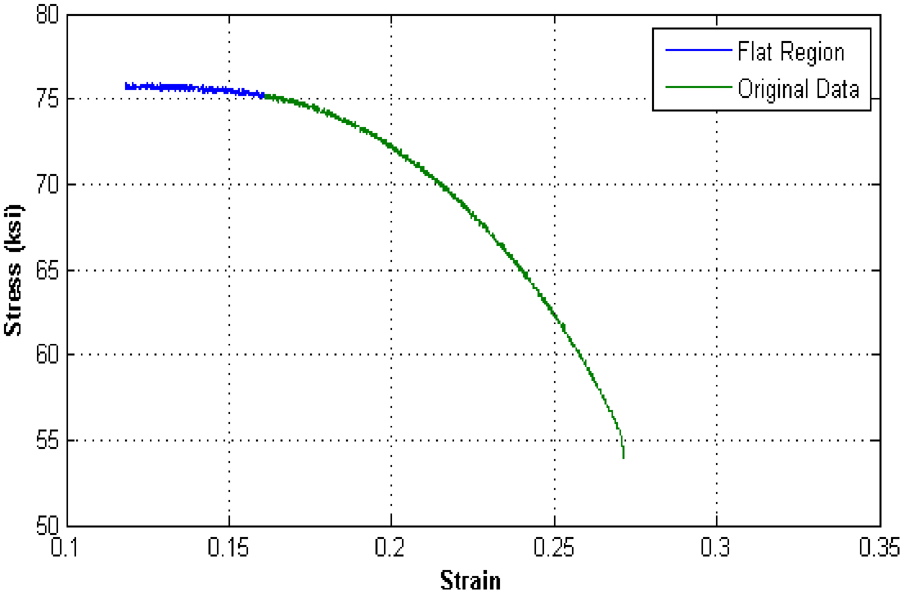

Figure 62: D1 Cutoff Location

The parabola method was modified to accommodate the new information regarding the UTS cutoff point. A 3-curve fit was used to locate the value of the critical strain. Instead of fitting only two parabolas, an additional line was fitted to the beginning of the curve. This had the effect of forcing the parabola fitting outside of the linear region. This method allows for the calculation of critical strain using all the data from UTS. The cutoff points are not arbitrary and therefore consistent for each curve. The algorithm used involved much iteration and required a large amount of processing time. To shorten the amount of iterations performed the plots were used to create boundaries for the search algorithms. This greatly reduced the required time and computing power. The results for the 3-curve fit are shown below in Table 8. The values were compared with those obtained from Blade Energy Partners. The results show good agreement with little error.

The true critical strain value is needed to calculate the DFDI. True strain was captured by the machine vision system used during the tensile test. The camera was able to capture the instantaneous diameter of the specimen. The true strain was calculated using the true diameter and load from the test frame. The true critical strain is found from the engineering critical strain. The engineering critical strain is used to find the corresponding true critical strain. The true critical strain values are also shown in Table 8. The true stress-strain curves for the pipe samples are shown in Figure 64.

Table 8: 3-Curve Fit and Blade Results

Sample	3-Curve Fit		Blade		Engineering Difference (%)	True Difference (%)
	Engineering (%)	True (%)	Engineering (%)	True (%)		
D1	24.2	68.1	24.1	66.8	0.41	1.91
D2	28.2	50.7	27.8	48.8	1.42	3.75
D3	24.5	60.2	24.3	59.3	0.82	1.50
D4	26.7	57.3	26.6	56.7	0.37	1.05
D5	26.8	60.0	27.2	63.3	-1.49	-5.50

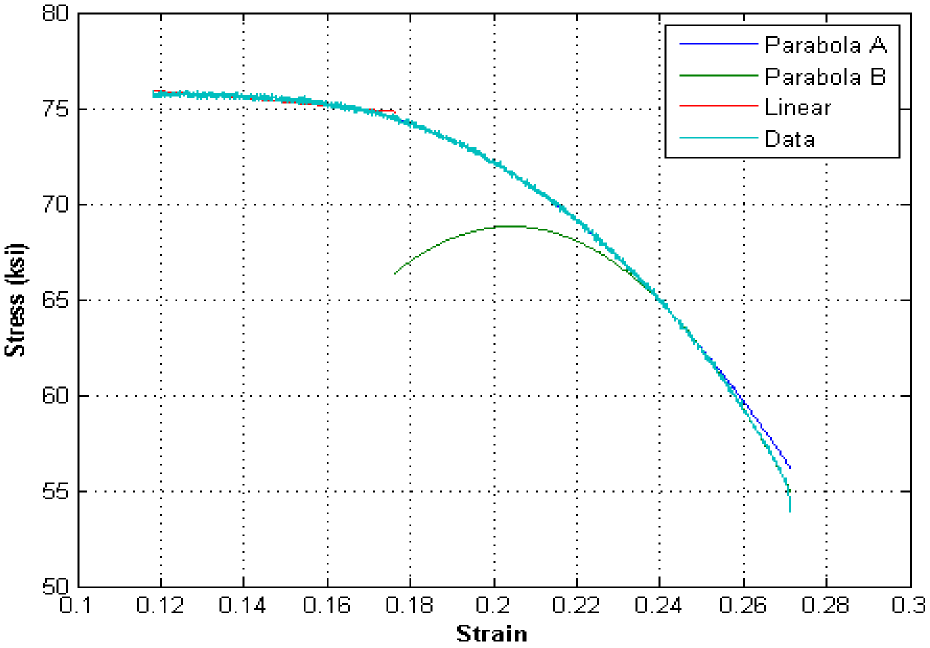

Figure 63: Critical Strain Using a 3 Curve fit

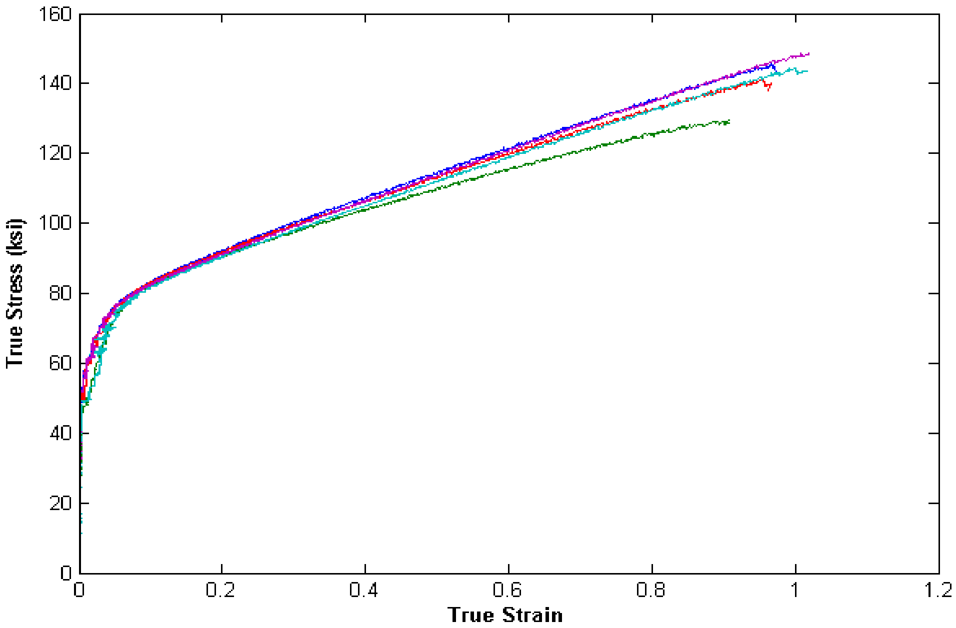

Figure 64: True Stress-Strain Curve for Pipe Samples

6.1.2 Slope-Strain Approach

The second approach to finding critical strain was using the slope-strain curve. This method is similar to the previous approach with the exception that two lines are fitted to the data rather than parabolas. This is intuitive because the derivative of a parabola is a straight line. It would then be expected that the critical strain is located at the intersection of the two lines associated with the derivative of each parabola. Several differentiation techniques exist to evaluate the derivative. The problem associated with numerical differentiation is noise. Most methods, such as finite differences, have the negative effect of amplifying noise. The amplified noise hides the true derivative making it difficult to locate critical strain. To overcome this challenge, various methods were used to smooth the data prior to differentiation. The first method was the Savitzky-Golay method.

This method used a parameter to control the amount of smoothness of the stress-strain curve. The method fits a parabola to a selected amount of data and takes the derivative of the parabola using the calculated coefficients. The amount of data used in the curve fit determined how smooth the resulting derivative was. Before investigating the effects of trimming the data, the parameter was calibrated. The calibration of the parameter was done by calculating the critical strain using different window sizes. The window size refers to the number of data points used in the curve fit. The minimum window size that provided stable results was selected. A plot of critical strain versus window size is shown in Figure 65. There is scatter in the results for window sizes 2% or less. At 2% the results began to level off. 5% was selected for the parameter because the results are stable for all samples at this level. Therefore, a window size of 5% of the data beyond UTS was used for the Savitzky-Golay method.

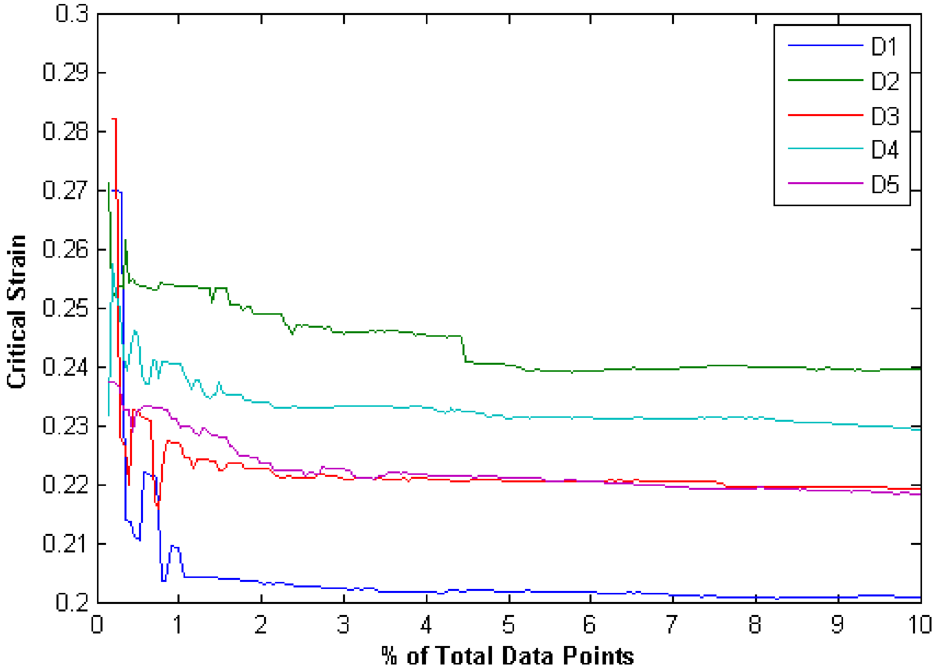

Figure 65: Savitzky-Golay Method with Varying Window Size

Figure 66 is a plot of the slope-strain curves for all samples using a window size of 5%. The curves are much smoother than other methods such as finite differences but still contain a significant amount of noise. This is the lower limit for smoothing that still provides stable critical strain values. Additional smoothing could be done to the curves similar to that shown in Figure 67 with the negative effect of increased computational time. As the window increases the amount of time needed for computation of the derivate increases.

With the parameter selected the effects of trimming were investigated. The procedure was identical to the stress-strain method. The data was trimmed by 60% and 10% from the UTS and FS ends respectively. The critical strain values associated with the trimmed data at the UTS and FS ends are shown in Figure 68 and Figure 69 respectively. The plots show the same trends as the stress-strain method. The plots start and end at similar locations.

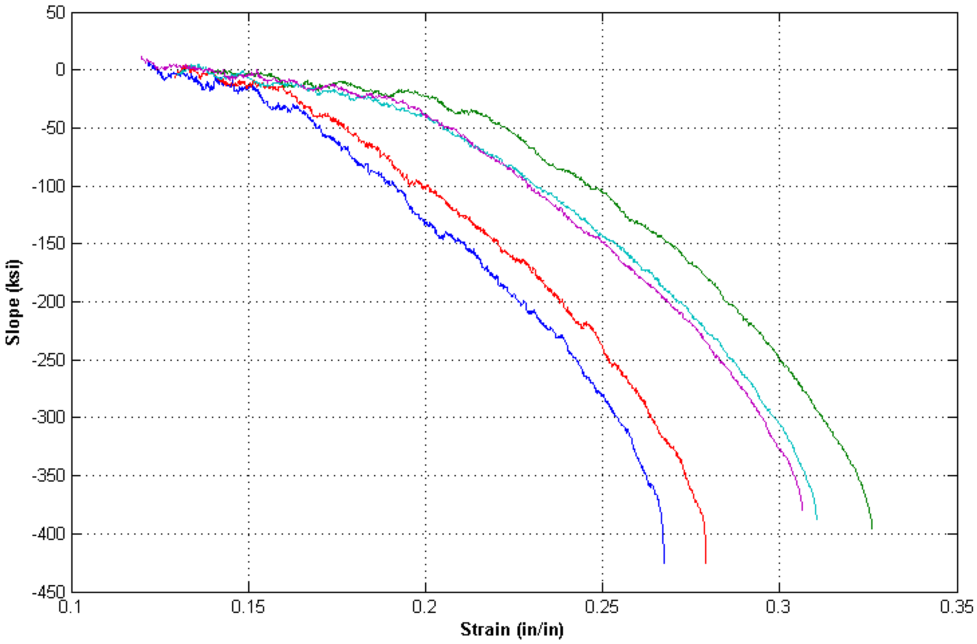

Figure 66: Savitzky-Golay Derivative with a 5% Window

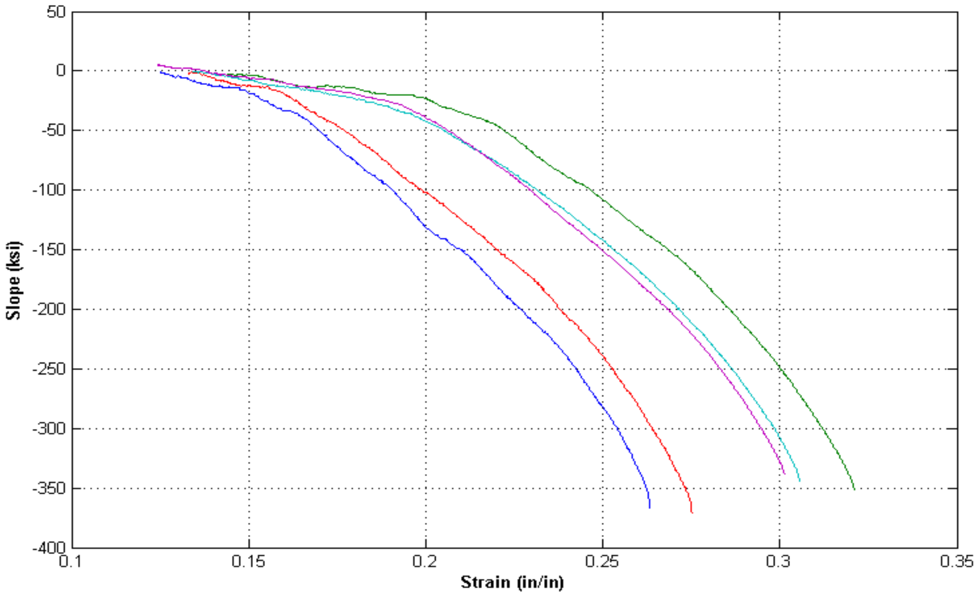

Figure 67: Savitzky-Golay Derivative with 10% Window

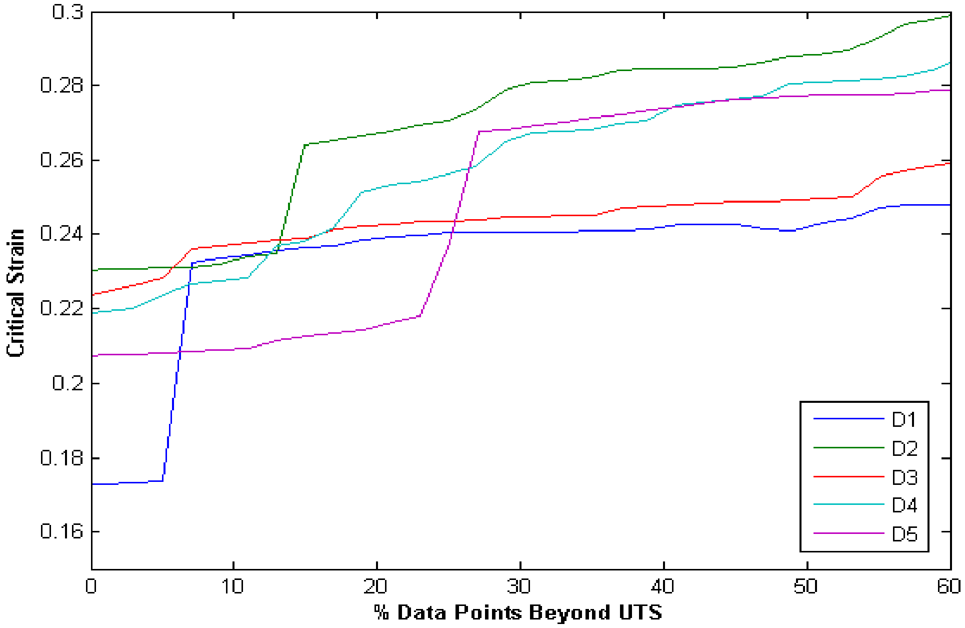

Figure 68: Savitzky-Golay Method Trimmed from UTS

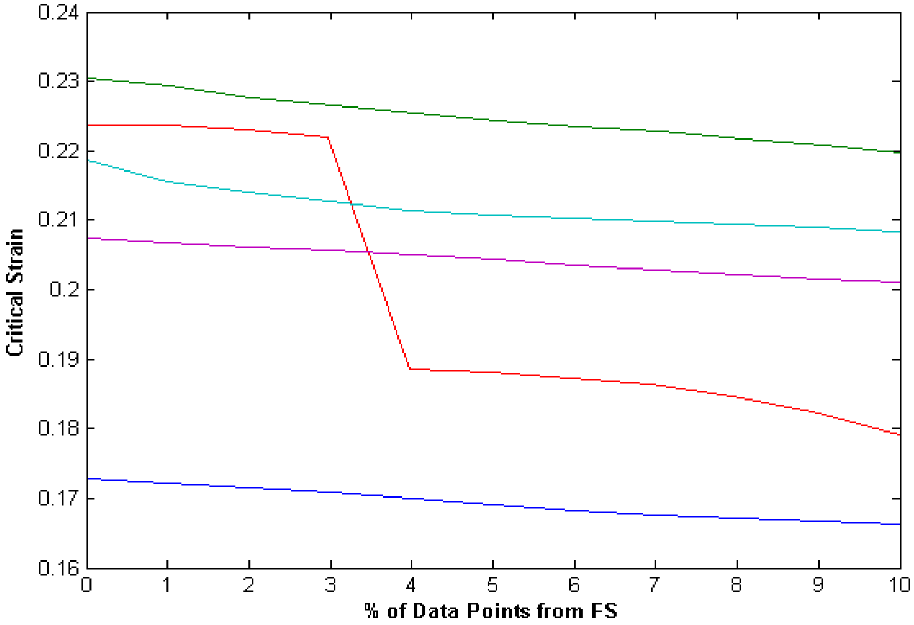

Figure 69: Savitzky-Golay Method Trimmed from FS

Figure 70 is a plot of the results from both the Savitzky-Golay and parabola methods. The curves show similar results with different jump locations in the data. The results from the stress-strain approach are represented by solid lines and the dashed lines represent the Savitzky-Golay results. The excessive jumps could be explained by the smoothing effect of the Savitzky-Golay method. The curves show stretches of smooth results but is interrupted by sharp jumps in the critical strain value. This is problematic when attempting to create a reliable method. The jumps were investigated to find the source of the irregularity in the curves.

The spikes in the Savitzky-Golay method are associated with changes in the slope-strain plot. The points at which the jumps occurred were traced back to the corresponding point on the slope-strain curve. The points were at locations at which the slope-strain curve had significant changes in smoothness. The change causes a jump in the best fit lines used to locate the critical strain. The Savitzky-Golay method, overall, shows good agreement with the parabola method used for stress-strain curves.

Another proposed method was the regularization method. The derivative of the stress-strain curve was taken from the smoothed stress-strain curve. Figure 71 is a plot of the smooth stress-strain curves for the dent samples. The noise in the data appears reduced from the original data. Just like the Savitzky-Golay method, the regularization technique had a smoothing parameter. This parameter was a smoothness penalty used in a least squares approach. This parameter can take on a wide range of values. The original data is not overly noisy and consequently requires little smoothing. The smoothing parameter was varied to observe the effect on the resulting stress-strain curves. The change in the smoothing effect was examined by increasing the smoothing parameter by orders of magnitude.

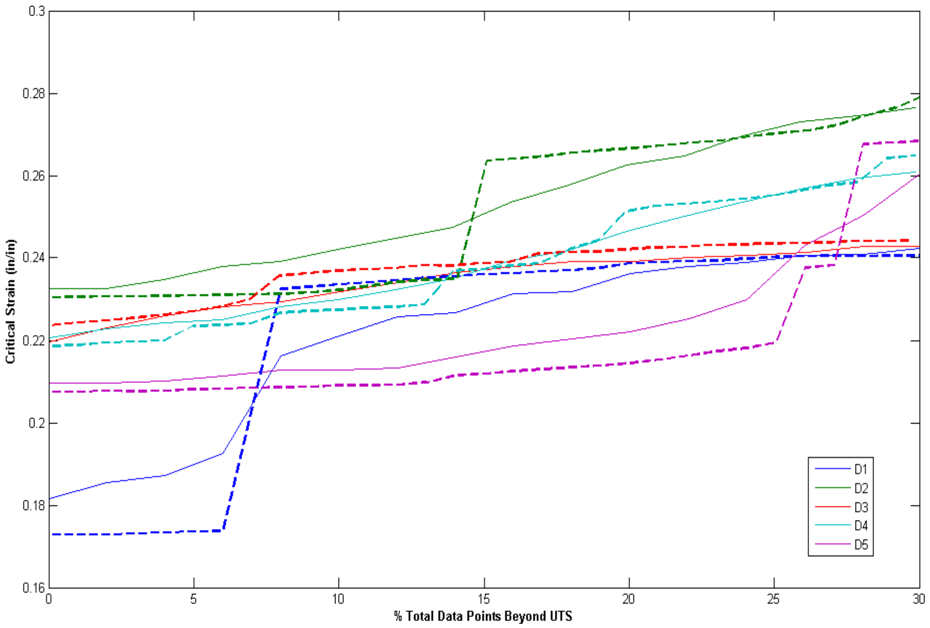

Figure 70: Combined Results for Trimming from UTS

The results for smoothing of D1 are shown in Figure 72. The plot has an offset of 2 ksi for each curve to separate them for examination. The curves show that by increasing the smoothing parameter from 100 to 100,000,000 has no obvious effect on the smoothness. A closer look shows that the data points are becoming smoother as the parameter is increased. Therefore, the value of 100,000,000 was selected for the smoothing parameter to ensure a highly smooth curve.

According to Stickel (2010), the derivative is simply calculated from the smoothed data using the finite difference method. The problem with this approach is shown in Figure 73. Even with limited noise in the data, there was still some amplification of the remaining noise. This obscures the derivative making it difficult to find the second kink. To limit the effects of the noise, the Savitzky-Golay algorithm was used in conjunction with the regularization method. This had the effect of smoothing out the noise in the calculated derivative. The results from this procedure are shown in

Figure 74. The data shows minimum difference between the results of the Savitzky-Golay method with or without regularization.

The parabola and Savitzky-Golay methods were compared using data trimmed at the end of the linear portion from the 3-curve fit. Table 9 shows the results for each sample. All values are within 1% of the values obtained using the 3-curve fit. The table also shows that the smoothing effects of the regularization technique have little effect on the critical strain value and that a 5% window for the Savitzky-Golay smoothing is satisfactory. The last column in Table 9 was calculated using a window size of 10%. The results were comparable to those obtained with the 5% window.

Table 9: 3-Curve Fit and Slope-Strain Results

Samples	3-Curve	Savitzky-Golay No Regularization	Minor Regularization	Major Regularization	Savitzky-Golay with Increased Window
D1	0.242	0.240	0.240	0.238	0.237
D2	0.282	0.279	0.279	0.279	0.275
D3	0.242	0.248	0.248	0.247	0.232
D4	0.267	0.264	0.264	0.264	0.267
D5	0.268	0.274	0.274	0.275	0.273

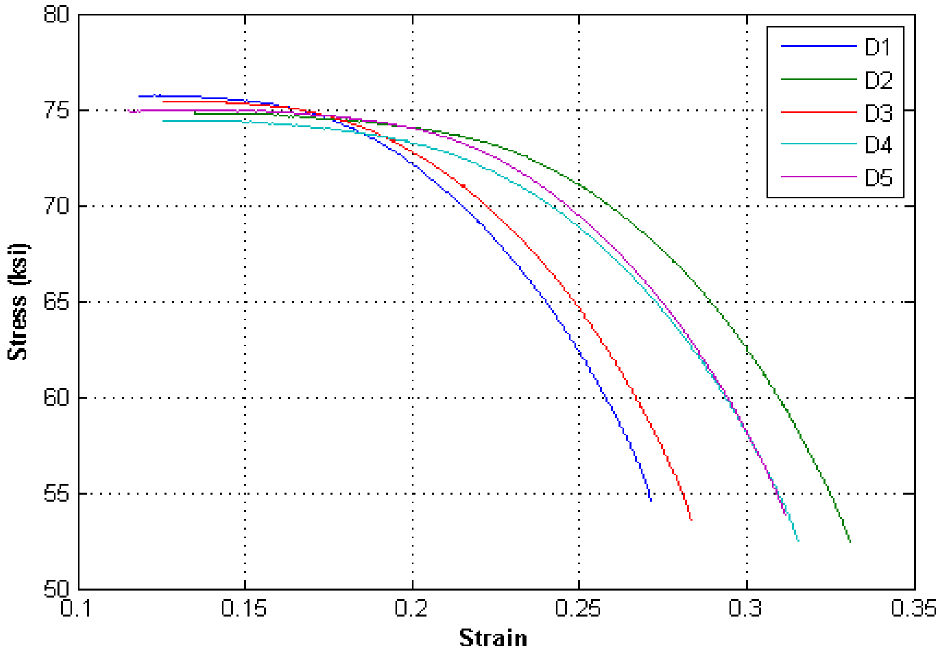

Figure 71: Smoothing by Regularization

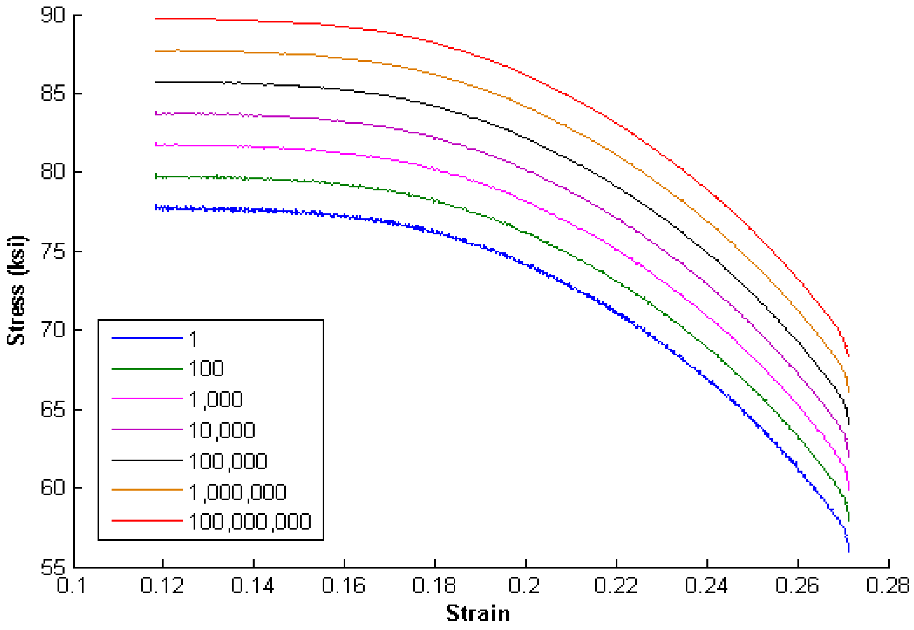

Figure 72: Smoothing Parameter

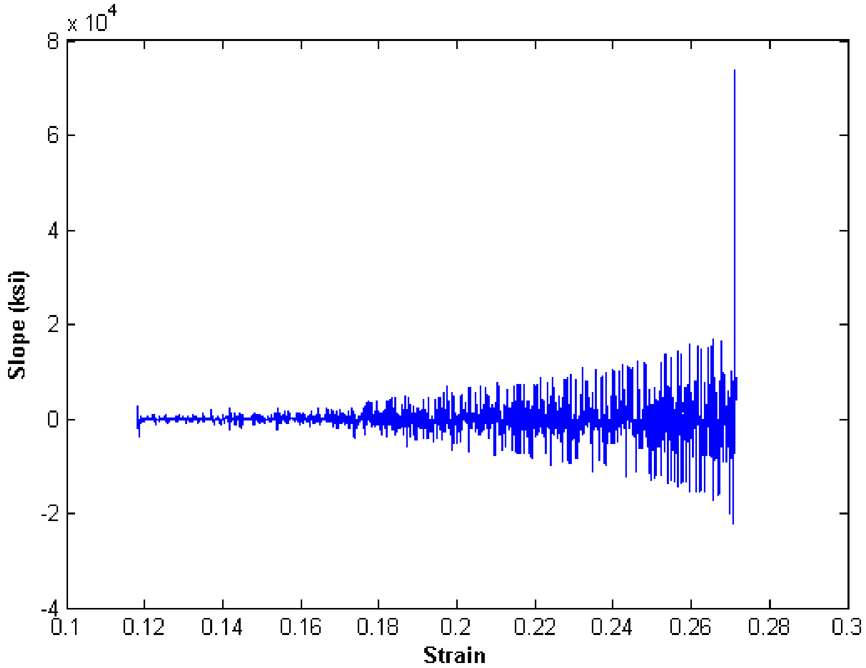

Figure 73: D1 Derivative Using Finite Differences

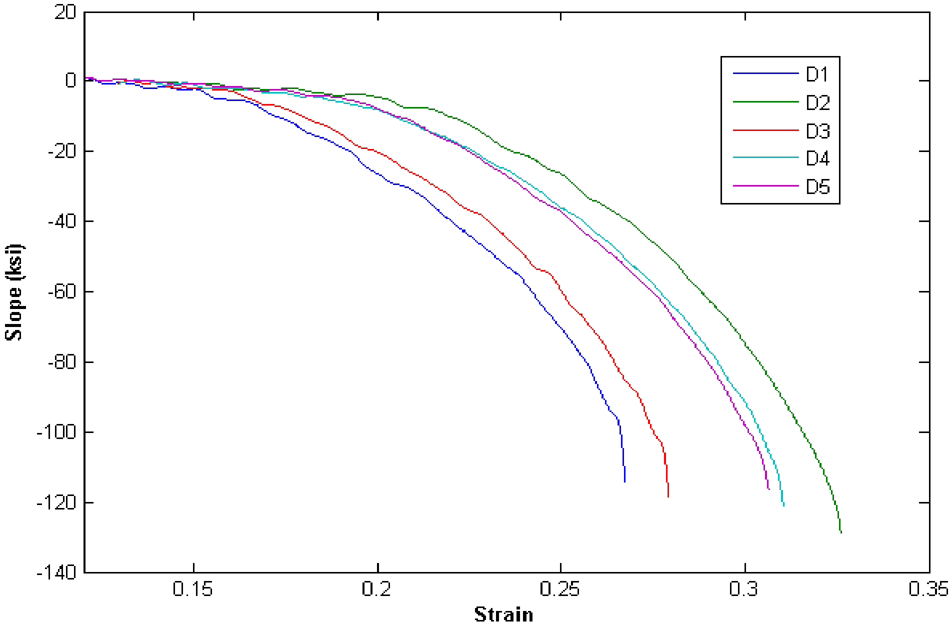

Figure 74: Regularization Smoothing with Savitzky-Golay Method

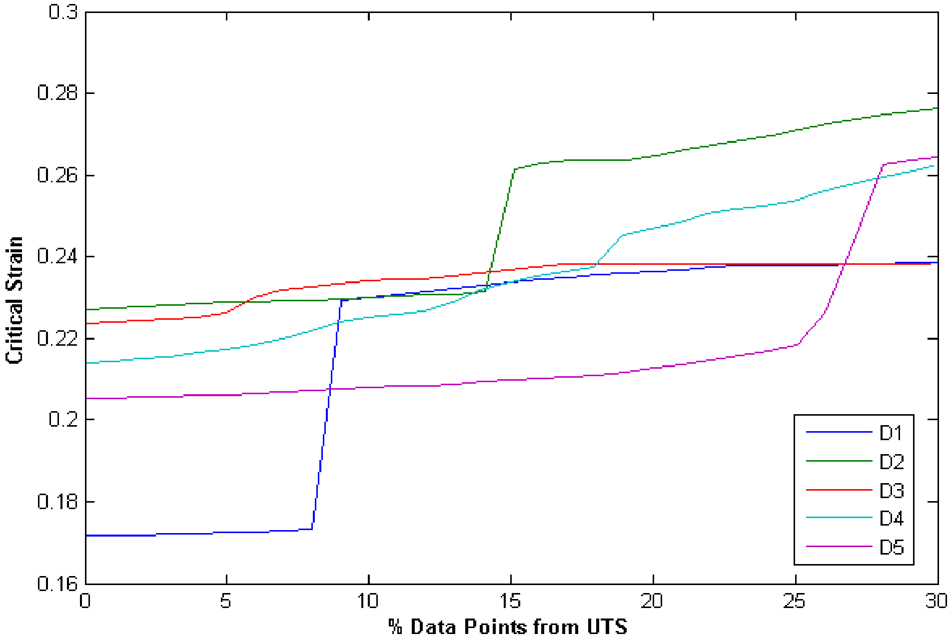

Figure 75: Regularization with Savitzky-Golay

6.2 Laser Evaluation

The results from the laser evaluation are shown in Table 10. The table shows significant scatter in the maximum depth values. The variation in depth values could result from a shift in the fitting of the reference cylinder with the scanned surface. The depths are based on the difference between the scan data and the reference cylinder thus explaining a shift associated with various reference cylinders. The scatter suggests an issue with the fitting algorithm used by the Pipecheck software.

The scanner is designed for field use. The equipment is typically taken to a location along a pipeline at which time the damaged area is exposed using excavation equipment. It is ideal that the technician using the laser equipment only scans the dent area and a small amount of undamaged pipe around the target area. This requires less time and less excavation. Since the data shows a significant amount of scatter, a technician using this equipment would need to scan a full 360 degrees around the pipe to ensure a good fit of the reference cylinder. Before the software is considered developed, Pipecheck should generate similar depth values regardless of the amount of area scanned away from the dent area. This issue was brought to Creaforms attention during the study.

The required data from Pipecheck is the depth profile of the deepest section. As mentioned previously, the profiles experienced a shift or translation. These shifts could be caused by different parameters of the scanning process. The most significant being the fact that the denting procedure requires an ID scan and the Pipecheck software is designed for OD scanning only. Since the strain calculations rely on the depth profile and not the actual depth measurements, a look at the depth profiles of the maximum depth was required. The scans can have different maximum depth values but must have the same profile for them to be considered equivalent.

For example, the 180 and 360 degree OD scan shows different depth values. If the profiles of the maximum depth section for both scans are laid over one another they should show little variance. If this is true then the two scans are considered the same and will give equivalent strain values. On the other hand, if the profiles show significant variance between the two profiles, then the strain calculations will not be the same and the two scans are not equivalent. Figure 76 shows the scatter associated with the depth profiles at maximum depth locations. It appears that each profile is the same. That is to say that each curve only differs by translation and rotation and not by any distortion. This seems correct because the profile is based on scan data. No matter how much of the pipe is scanned the overall profile is the same. The only difference lies in the placement of the reference cylinder.

Figure 77 shows the same depth profiles from Figure 76 with the exception that they have been normalized and translated so they overlay one another. The profiles were only mirrored and translated. None of the profiles experienced any stretching or fitting of any kind. The results show that each profile is almost identical. There is a shift of the location of the spiral weld between the OD and ID scans. This is to be expected because the location of the weld moves between the two surfaces.

Table 10: Laser Evaluation Results

Surface	Circumferential (deg)	Dent Resolution (mm)	Pipe Resolution (mm)	Maximum Depth (mm)
OD	180	1.00	1.00	-22.849
OD	360	1.00	1.00	-30.013
OD	180/360	1.00	1.00	-27.310
OD	360	0.20	1.00	-21.978
OD	180	High Res. Button	1.00	-16.148
ID	360	1.00	1.00	-29.841
ID	180	0.50	0.50	-22.941

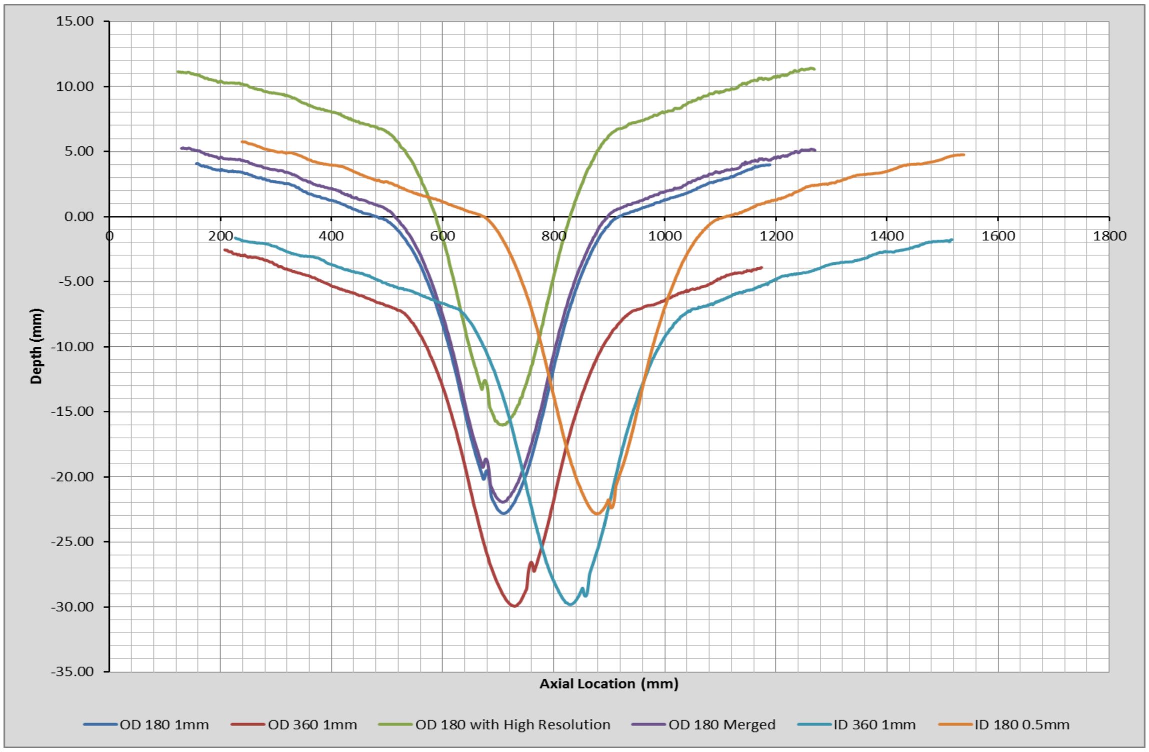

Figure 76: Depth Profile at Max Depth Locations

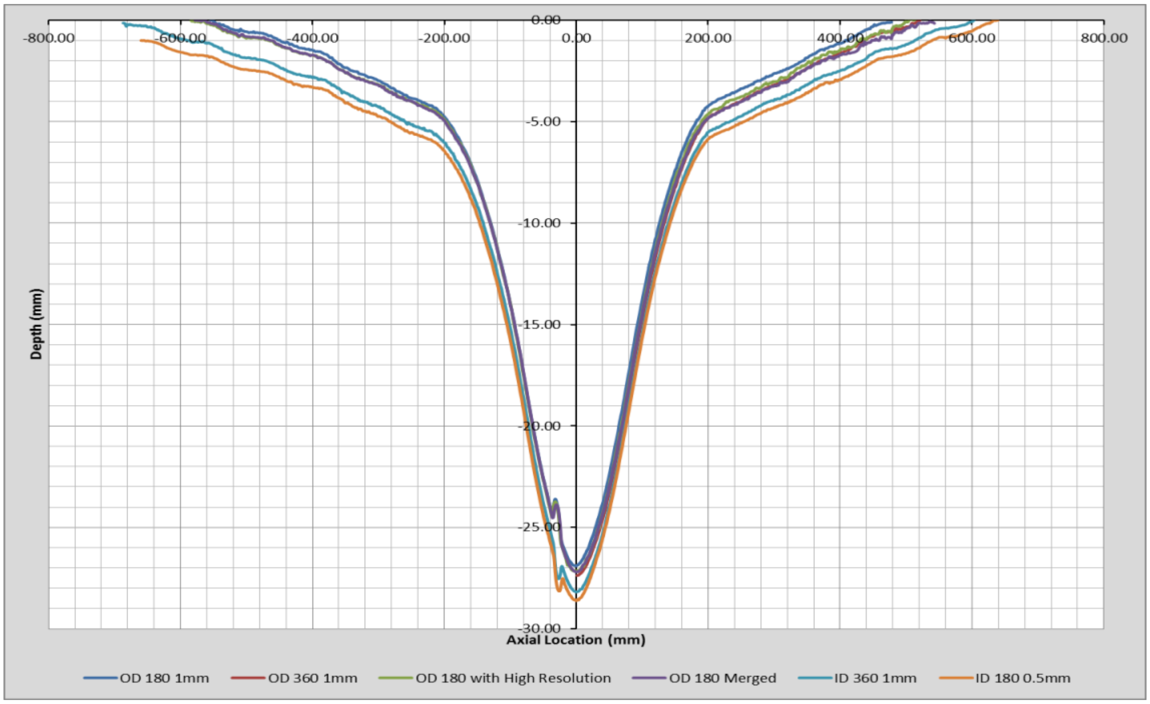

Figure 77: Normalized Depth Profiles as Max Depth Locations

The profile data shows that any of these scans may be used for the strain calculations with little to no error. Table 10 also shows there is only a 0.40% error between the depth values calculated between the 0.50 mm and 1.00 mm ID scans. This means that either resolution can be used for scanning smooth dents with little error. Many would suggest using the higher resolution to maintain accuracy when capturing the maximum depth. The issue with using 0.50 mm resolution is the time and computer capacity required. Depending on the experience of the scanner, a typical scan of the interior of a pipe can take roughly 1 hour per meter of pipe section. This is what was experienced on both the 24 inch evaluation pipe as well as the 34 inch denting pipe. They require similar times because of various tradeoffs between pros and cons. A smaller pipe has less scan area but limits the operator’s ability to move inside the pipe. A larger pipe allows for more mobility but has a larger surface area.

In addition to the time restrictions, computer limitations were also introduced during testing of the laser equipment. In general, a 360 degree by 1 meter scan at 1 mm resolution requires roughly 60% of the RAM to carry the data during scanning. Scanning the same amount of area at 0.50 mm resolution required multiple scans that were eventually merged together. This proved very strenuous on the computer and led to lock ups and crashes. Although it is possible to scan the pipe at 0.50 mm, the amount of time and computer power required does not justify the minor increase in accuracy. As an alternative, the pipe could be scanned at a lower resolution and merged with a high resolution scan of the dented region. This was done with the evaluation pipe. The pipe was scanned at 1.00 mm and the dent at 0.20 mm resolution. The overall effect of such a scan would be the increased difficulty in assuring a successful merge and a small increase in accuracy.

In conclusion, the above plots and tables show that the laser equipment will accomplish what is needed for the DFDI evaluation. Despite the resolution and the size of the scan, the overall dent profile will be the same. The difference lies in the depth values which are based on the location of the reference cylinder. The scatter in the maximum depth values is a product of this fact and will be rectified in later versions of Pipecheck. The most important conclusion that can be made from this evaluation is that an OD and ID scan will result in the same dent profile. This means that Pipecheck and the scanner can be used for the denting test despite the fact that the software is intended for OD scans only. Based on the above results, the denting pipe will be scanned at 1.00 mm resolution 360 degrees around the pipe. The 360 degrees is selected to better capture the deformation of the pipe and to obtain a more reliable scan even though a 180 degree scan is capable of capturing the profile.

6.3 Denting Test

The goal for this portion of the study was to verify the loads, strains, and dent profiles from the test data to the results of the strain calculations. This was accomplished in three steps. The first task was to verify an FE analysis with results from the dent test. The FE model was considered valid if the results matched reasonably well with the measured data. The second task was to create a second FE model based on the depth data acquired from the laser scanner. The model was deformed to the same shape as the physical pipe. This model provided actual strain values from the pipe based on the known dent shape. The final task was to calculate the strains based on the modified ASME B31.8 strain equations. If the strain values for the second FE model matched those from the strain calculations, then the ASME B31.8 modified equations were valid and acceptable for use with the DFDI.

The results from the denting process are shown in Table 11. The force, depth, and strains were used to verify the FE model. The longitudinal and circumferential profiles are shown in Figure 78 and Figure 79, respectively. Both plots show that the pipe became out-of-round during the denting procedure. The stiffeners located at the ends of the pipe helped to restrain the pipe from excessive deformation. The amount of deformation to the circumferential cross section can be seen by the LVDT or laser data. Table 11 shows that the horizontal LVDT experienced an average extension of 0.37 inches per dent increment. The vertical LVDT compressed at an average length of 1.04 inches.

The vertical LVDT was used to monitor the dent depth during testing. Therefore, the average should have been 1.02 inches. The error occurred during the 3% increment. The LVDT was placed 1 inch away from the dent apex. This caused the apex of the dent to deform beyond 1.02 inches. This has no effect on the outcome of the study because the actual profiles were captured by the laser scanner. The LVDT's were used as a verification tool for the scanner and FE analysis. The only significant discrepancy between the laser scanner and LVDT readings was during rerounding. The vertical and horizontal displacements had an error of 37.3% and 45.7% respectively. This could be explained by errors associated with placing the LVDT's back into the deformed pipe. Table 12 is a comparison between the laser scanner and LVDT measurements.

Table 11: Denting Data Summary

	Depth (mm)	Force (kips)	$LVDT_V$ (in)			$LVDT_H$ (in)		
			Start	Stop	Step	Start	Stop	Step
3%	-20.26	-18.76	0.000	1.123	**1.123**	NA	NA	**NA**
6%	-41.17	-26.88	0.212	1.232	**1.020**	1.833	1.508	**0.325**
9%	-61.00	-35.86	0.332	1.351	**1.019**	1.800	1.414	**0.386**
12%	-80.41	-43.88	0.088	1.109	**1.021**	1.896	1.501	**0.395**
15%	-100.28	-51.02	0.252	1.272	**1.020**	1.861	1.482	**0.379**
Reround	-65.01	0	1.219	-0.347	**1.566**	1.482	2.331	**0.849**

Table 12: LVDT and Scanner Measurements

Step	Vertical Displacements			Horizontal Displacements		
	Scanner	LVDT	% Error	Scanner	LVDT	% Error
3%	-1.245	-1.123	9.8%	0.647	-	-
6%	-1.023	-1.020	0.2%	0.327	0.325	0.6%
9%	-1.063	-1.019	4.1%	0.356	0.386	8.5%
12%	-1.032	-1.021	1.1%	0.358	0.395	10.3%
15%	-1.019	-1.020	0.1%	0.370	0.379	2.4%
Reround	2.497	1.566	37.3%	-1.562	-0.849	45.7%

Figure 78 is plot of the longitudinal depth profiles exported from Pipecheck. The depths were taken at 0.5 m on each side of the dent apex. The data was exported at a grid spacing of 1 mm and 1 degree. This equates to 1 mm in the longitudinal direction and 7.37 mm in the circumferential. The actual measured depths were taken at a spacing of 1 mm by 1 mm. This is a relatively fine mesh when compared to high resolution PIGs. High resolution PIGs have approximately 64 sensors. This is equivalent to a circumferential spacing of 41.45 mm. The laser scanner has a much higher chance of capturing the maximum depth than the high resolution PIGs. Strain calculation based on the laser profile is more accurate than those from ILI tools. Figure 79 is plot of the circumferential cross section. The out-of-roundness can clearly be seen. The pipe diameter decreases in the vertical direction while it expands in the horizontal. The result is an oval shaped pipe.

These profiles are to be used for curvature calculations used in the modified ASME B31.8 strain equations. These equations were proven to be sufficient in the root analysis study conducted by Arumugam et. al. (2012). This study intends to properly validate the equations and further prove that they are comparable to FE results. The ultimate goal is to create a damage assessment tool that is capable of rapidly identifying critical damage features in a pipeline. This would allow more advanced tools such as FEA to be used for only severe damage as determined by the assessment tool. This is only for the first part of the study which will eventually evaluate pipes of different material and damage. The current pipe used in this study was intended to validate the process and justify the study of more pipes. The results from the current denting test are being evaluated by Blade Energy Partners.

Blade is currently running FE models to compare with the test results as well as the results from the strain calculations. Using the deformation data from the laser equation, Blade intends to calculate the DFDI from FE results. The DFDI values will be compared to those obtained from the modified strain equations. If the results are comparable then the method is verified and more research can be conducted. The definition of the DFDI is that a crack has formed when the DFDI is equivalent to 1. According the initial FE results conducted by Blade prior to testing, the pipe should have formed a crack between 12% and 15%. Unlike the results from the case study done by Arumugam et. al. (2012), a visible crack did not form on the surface. The root cause study showed visible cracks along the predicted paths shown in Figure 29. Figure 80 shows the dent surface inside the pipe at 15% depth. A visible crack did not form on the inside surface of the pipe as was shown in the root cause study. There were popping sounds heard during the 12% and 15% increments. These sounds were similar to those heard during a tensile test after failure. These sounds could suggest cracks forming within the pipe wall. The sounds could be the formation of microcracks by the linking of microvoids.

This is to be determined after modified FE models have been analyzed. To investigate the value of the DFDI for visible cracks, the next test will go until a visible crack has formed. This will require a larger actuator with a higher maximum force and a longer stroke. The FE models are currently under review to account for differences between the original FE model and the denting test. One such adjustment is the loading of the pipe. The original FE model used a rigid spherical indenter. This type of contact is mathematically modeled as a point load where only one point of the sphere is in contact with the surface. Testing showed that the indenter actually left an imprint on the surface of the pipe. As can be seen in Figure 81, the imprint is better modeled as a soft contact rather than rigid. Investigation of methods for correcting this is currently under way and will be implemented on the next series of denting tests.

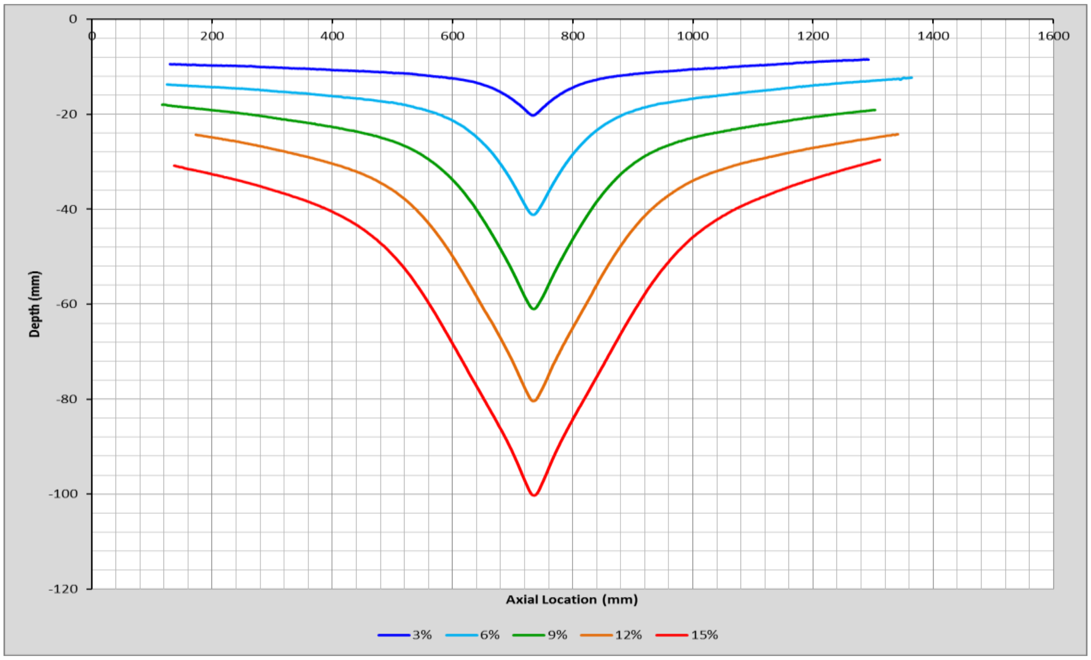

Figure 78: Longitudinal Profiles

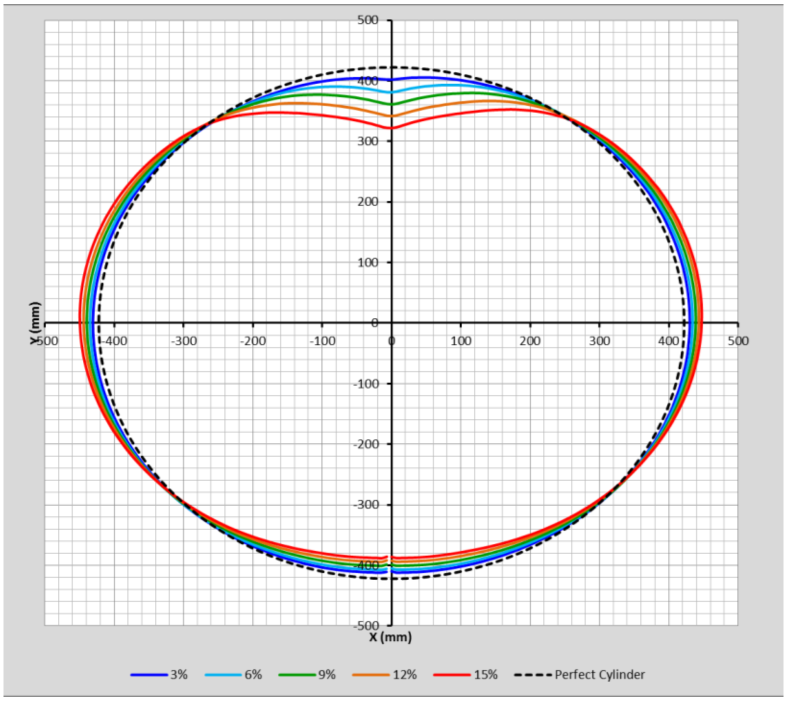

Figure 79: Circumferential Profiles

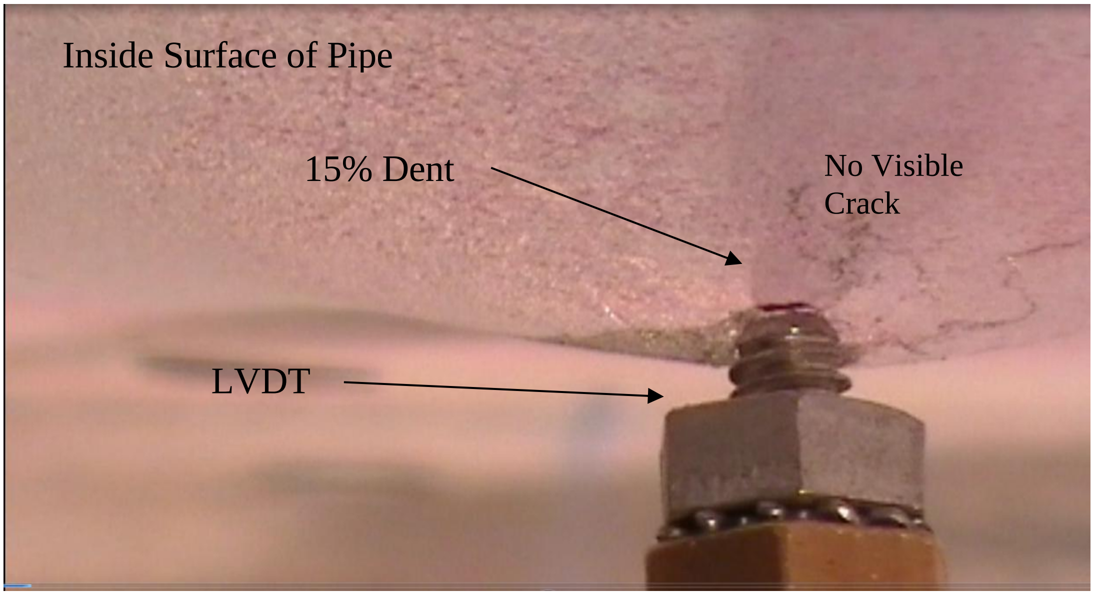

Figure 80: Dent at 15% Depth (No Crack)

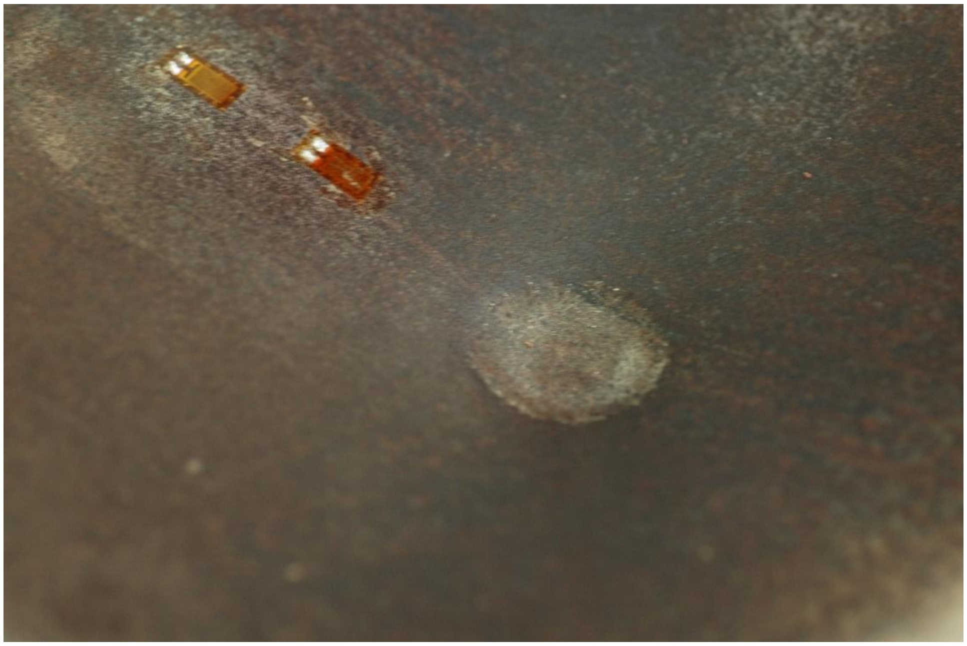

Figure 81: Imprint of Spherical Indenter

7 CONCLUSION

The research leading up to this study has shown that critical strain is the material property representing the initiation of cracking. This is the importance of critical strain and its use in the ductile factor damage indicator (DFDI). This study investigated various techniques for locating critical strain from the materials stress-strain curve. This material property was used in the DFDI to quantify the amount of plastic damage in plain dents. The research also investigated the equipment used to calculate the strain within the dent, more specifically the laser equipment and software. The denting test showed that visual cracks did not occur as was expected from the FE analysis. Since critical strain represents crack initiation, a crack could have initiated but is not visible at the surface. A detailed conclusion for each aspect of the research is discussed in the proceeding sections.

7.1 Critical Strain

The results show that trimming the data from UTS or FS does have a significant effect on the calculated critical strain value. Trimming data from the UTS increases critical strain whereas trimming from FS results in a reduction. The UTS end of the tensile test has a linear section prior to the parabolic curve. The plots showed that jumps occurred in the critical strain values as this linear portion was decreased. To consistently and accurately locate critical strain, the linear portion should be removed entirely to avoid interference with the parabolic fit. The FS end did not contain a linear section. The plots did show that trimming the FS had more or less a linear effect on critical strain. There is no reason to trim the FS end of the stress-strain curve. This only has the effect of shifting the critical strain value. The only problem that occurred with the FS end was artifacts left behind by the tensile test. These artifacts are data points measured after fracture of the sample. These points give a false bend in the curve. These should be removed prior to calculating critical strain. The Savitzky-Golay smoothing method proved to be an effective means of calculating critical strain from the slope-strain curve when used with a window size of 5% or greater.

The stress-strain and slope-strain results showed good agreement and proved to be viable methods for finding the critical strain value. The most important task to obtain reliable results is to ignore the linear portion of the stress-strain plot beyond UTS. This allows for a good fit of the parabolas and an accurate value for critical strain. The DFDI requires the true critical strain. Therefore, the critical strain was found using the engineering stress-strain plot but was then correlated to the appropriate true strain value. The values are found in Table 8. The plots of the results from the 5 pipe samples can be found in Appendix D.

The camera system used to capture true stress has been used in many different applications most notably in manufacturing. The use of a machine vision system to measure the diameter of a tensile specimen proved to be ideal. This system overcame the daunting task of constantly measuring the diameter after necking. The camera made it possible to find the true critical strain needed to calculate the DFDI for damage assessment.

7.2 Laser Evaluation

The laser evaluation was required to prove the effectiveness of the laser scanner for the current study. The evaluation investigated the effects of varying scanning areas, techniques and resolutions. The most important goal of the evaluation was to justify the use of the scanner and Pipecheck software for the denting test. The target data for the laser scanner was the dent profile. The evaluation showed that the profiles, although translated, were the same for all scan types. The ID and OD scan showed similar profiles and therefore proved that the equipment could be used for the strain equations needed for the DFDI.

The ID scan was required because the indenter was in the way of the scanner during denting. The Pipecheck software was intended for OD scans only but testing showed that ID scans provided similar results. The only difficulty encountered by the software was during the scanning process. The view of the pipe was often obscured by the other side of the scanned pipe. This is a direct consequence of the software's design for OD scanning. This was overcome by adjusting the scanning process so that the current scan area was always in view in the Pipecheck software. The limitation of time and computing power limited the resolution of the scan to 1.00 mm and the scanning area to 1 m in the longitudinal direction and 360 degrees in the circumferential.

7.3 Denting Test

The denting process was the first of many pipes to be tested. The goal was to validate the DFDI approach to justify further testing. The results from the denting test are still under review but a few conclusions can be drawn from what has already been done. The first is that the laser equipment proved successful with the profile scans. The results from the scans are shown in Appendix B. The second is that the idealized conditions from the original FE analysis do not reflect actual conditions. The modeling of the contact point between the indenter and pipe surface did not reflect what was actually seen during testing. The imprint left in the pipe surface after denting affected the outcome of the modified strain equations. Since the indenter caused an impression on the surface the curvature at the deepest point was always the same. This caused a constant value for the DFDI for each step when in reality the DFDI should continuously increase. This suggests that the denting procedure should be modified to reflect field conditions caused by indenters such as rocks.

Since the data is still being analyzed, the validity of the DFDI approach cannot be determined at this time. The results show that the laser scanner did an excellent job of capturing the pipe deflections and that these deflections can be incorporated into an FE model to obtain stress and strain values for the dented pipe. When an actual model is obtained, the results from the strain calculations can be compared and validated for further research. The FE model can provide insight as to when a visual crack might form and perhaps why a visual crack was not seen for this pipe.

The sounds heard during the 12% and 15% increments could be explained by the linking up of microvoids to form a microcrack. This would mean that the DFDI value of 1 corresponds to the initiation of the crack within the pipe, but not necessarily a visual crack. To investigate the relationship between a visual crack and the DFDI, the next series of tests will dent the pipe until a visual crack is detected. The absence of a visual crack could also be explained by the discrepancies between the original FE results and the actual denting. The modified FE should show whether the DFDI value was actual at a value of 1 between 12% and 15%. The results might show that further denting was required to actually reach a DFDI value of 1.

7.4 Further Investigation

To further investigate the applicability of critical strain and the DFDI approach for the assessment of mechanical damage, a few modifications and additional adjustments can be made:

1. Investigate the stress-strain curves and associated critical strain for different materials. Different materials have varying stress-strain curves. The methods proposed in this research might be difficult or unreliable for a material with a unique stress-strain curve.
2. Perform the dent test on various pipe diameters. The modified DFDI approach must be applicable to many different pipe diameters for it to be considered for the pipeline industry.
3. Perform the denting test on various grades of steel. The key to the validity of the modified DFDI approach is the critical strain value. Additional materials need to be tested to ensure that this property is consistent for all pipe materials.
4. Investigate the effects of additional damage features such as dents with gouges or dents on welds. The current study is focused on plain dents. To expand the applicability of the method, other damage features such as dents on welds need to be investigated.
5. The effects of critical strain on fatigue life could also be investigated. The DFDI represents the amount of damaged experienced by the pipe. How

does this affect the fatigue life of the pipe? Additional research is needed to investigate the correlation between fatigue life and the DFDI.

REFERENCES

Ahnert, K. (2007). "Numerical Differentiation of Experimental Data: Local Versus Global Methods." Comput.Phys.Commun., 177(10), 764-774.

Anderson, T. L. (1995). Fracture Mechanics : Fundamentals and Applications. CRC Press, Boca Raton.

Argon, A. S., IM, J., and Safoglu, R. (1975). "Cavity Formation from Inclusions in Ductile Fracture." Metallurgical Transactions A, 6A.

Arumugam, U., Gao, M., and Krishnamurthy, R. (2012). "Root Cause Analysis of Dent with Crack: A Case Study." Proceedings of IPC2012 9th International Pipeline Conference Calgary, Canada, 24-28.

Baker, M. (2009). Mechanical Damage Final Report. Washington, D.C. : U.S. Dept. of Transportation, Pipeline and Hazardous Materials Safety Administration, Office of Pipeline Safety, Washington, D.C.

Bridgman, P. W. (1964). Studies in Large Platic Flow and Fracture. Harvard University Press, Cambridge.

Broek, D. (1973). "The Role of Inclusions in Ductile Fracture and Fracture Toughness." Engineering Fracture Mechanics, 5 55-66.

Chartrand, R. (2011). "Numerical Differentiation of Noisy, Nonsmooth Data." ISRN Applied Mathematics, 2011 1.

Cosham, A., and Hopkins, P. (2003). "The Effect of Dents in Pipelines—Guidance in the Pipeline Defect Assessment Manual." International Journal of Pressure Vessels and Piping, 81(2), 127-139.

Czyz, J. A. (2008). "Calculating Dent Strain." Pipeline and Gas Technology, 2, 38.

Eilers, P. H. C. (2003). "A Perfect Smoother." Analytical Chemistry, 75(14), 3631.

Ferziger, J. H. (2002). Computational Methods for Fluid Dynamics. Springer Berlin,.

Fischer, F. D., Kolednik, O., Shan, G. X., and Rammerstorfer, F. F. (1995). "A Note on Calibration of Ductile Failure Damage Indicators." International Journal of Fracture, 73 345-357.

Gao, M., McNealy, R., and Krishnamurthy, R. (2008). "Strain-Based Models for Dent Assesment - A Review." Proceedings of IPC2008 7th International Pipeline Conference Calgary, Alberta, Canada, .

Goods, S. H., and Brown, L. M. (1978). "Overview No. 1: The Nucleation of Cavities by Plastic Deformation." Acta Metallurgica, 27(1), 1-15.

Griffith, A. A. (1921). "The Phenomena of Rupture and Flow in Solids." Philosophical Transactions of the Royal Society of London.Series A, Containing Papers of a Mathematical or Physical Character, 221 163-198.

Griffith, A. A. (1921). "The Phenomena of Rupture and Flow in Solids." Philosophical Transactions of the Royal Society of London.Series A, Containing Papers of a Mathematical or Physical Character, 221 163-198.

Hancock, J. W., and Mackenzie, A. C. (1975). "On the Mechanisms of Ductile Failure in High-Strength Steels Subjected to Multi-Axial Stress-States." Journal of Mechanics and Physics of Solids, 24 147-169.

Juliano, T., Dominich, V., Buchheit, T., and Gogotsi, Y. (2004). "Numerical Derivative Analysis of Load-Displacement Curves in Depth-Sensing Indentation." Mater Res Soc Symp P, 791 191-201.

Kachanov, L. (1986). Introduction to Continuum Damage Mechanics. Springer, .

McClintock, F. A. (1968). "A Criterion for Ductile Fracture by the Growth of Holes." Journal of Applied Mechanics, 35 363.

McClintock, F. A., Kaplan, S. M., and Berg, C. A. (1966). "Ductile Fracture by Hole Growth in Shear Bands." International Journal of Fracture Mechanics, 2(4), 614-627.

Moin, P. (2010). Fundamentals of Engineering Numerical Analysis. Cambridge University Press, New York.

Noronha, D. B., Martins, R. R., Jacob, B. P., and de Souza, E. (2010). "Procedures for the Strain Based Assessment of Pipeline Dents." International Journal of Pressure Vessels and Piping, 87(5), 254-265.

Psioda, J. A. (1985). "Microstructural Aspects of Fracture by Dimpled Rupture." International Metals Reviews, 30(1), 157-180.

Puttick, K. E. (1959). "Ductile Fractures in Metals." Philosophical Magazine, 4(44), 964-969.

Ramm, A., and Smirnova, A. (2001). "On Stable Numerical Differentiation." Mathematics of Computation, 70(235), 1131-1153.

Rice, J. R., and Tracey, D. M. (1969). "On the Ductile Enlargement of Voids in Triaxial Stress Fields." Journal of Mechanics and Physics of Solids, 17 201-217.

Rogers, H. C. (1960). "The Tensile Fracture of Ductile Metals." Transactions of the Metallurgical Society of AIME, 218 498-506.

Rosenfeld, M. J. (1998). "Strain Estimation Using VETCO Deformation Tool Data." Proceedings of the International Pipeline Conference, 1(1998), 389-397.

Rosenfield, A. R. (1968). "Criteria for Ductile Fracture of Two-Phase Alloys." Metallurgical Reviews, 29-40.

Savitzky, A. (1964). "Smoothing and Differentiation of Data by Simplified Least Squares Procedures." Analytical Chemistry, 36(8), 1627-1639.

K. H. Scott. (2011). "The PIGs that Keep Things Clean." http://www.personal.psu.edu/afr3/blogs/SIOW/2011/12/the-pigs-that-keep-things-clean.html (05/25, 2013).

Singh, A. K., and Bhadauria, B. S. (2009). "Finite Difference Formulae for Unequal Sub-Intervals Using Lagrange's Interpolation Formula." International Journal of Math. Analysis, 3(17), 815-827.

Stickel, J. J. (2010). "Data Smoothing and Numerical Differentiation by a Regularization Method." Computers & Chemical Engineering, 34(4), 467.

Tvergaard, V., Tvergaard, A., and Needleman. (1984). "Analysis of the Cup-Cone Fracture in a Round Tensile Bar." Acta Metallurgica, 32(1), 157-169.

Voyiadjis, G. Z. (2005). Damage Mechanics. Taylor & Francis, Boca Raton.

APPENDIX A

Parabola Function

```
function [ critstrain,critstraint,lspot,critstress,critstresst ] =
parabolacalc2( x, y,z1, z2)
%  parabolacalc     Find crtitical strain by fitting parabolas
%  Input:
%      x            = vector containing engineering strain
%      y            = vector containing engineering stress
%      z1           = vector containing true strain strain
%      z2           = vector containing true stress data
%  Output:
%     critstrain    = calculated engineering critical strain value
%     critstraint   = calculated true critical strain value
%     critstress    = corrosponding engineering stress
%     critstresst   = corrosponiding true stress
%     lspot
%
%  Author:
%     Ryan Milligan, ryanmilligan10@gmail.com
%     Texas A&M University, Civil Engineering Department
%     27 April 2013

% Loop through each data point beginning with enough data points so
% polyval is not badly conditioned n is the end location for the linear
% portion of the curve

for n = 1:round(0.40*length(x))

    % i is the current critical strain value
    for i = round(0.70*length(x)):length(x)-5

        % Find the coeffecients of the best fit polynomial before i and
        % after i using matlab polyfit function

        tempx1 = x(n:i);
        tempy1 = y(n:i);
        tempx2= x(i:length(x));
        tempy2= y(i:length(y));

        % Calculate the error associated with the linear portion of the
        % curve

        liney = y(1)+((y(1)-y(n))/(x(1)-x(n))).*x(1:n);

        currenterr = sum(abs(liney-y(1:n)));

        tempx1 = tempx1-x(i);
        tempy1 = tempy1-y(i);
```

```
        tempx2 = tempx2-x(i);
        tempy2 = tempy2-y(i);

        % Evaluate the stress at each strain level using the best fit
        % coefficients

        [a1,b1] = pfit(tempx1,tempy1);
        [a2,b2] = pfit(tempx2,tempy2);

        newy1 = (a1.*tempx1.^2+b1.*tempx1)+ y(i);
        newy2 = (a2.*tempx2.^2+b2.*tempx2) + y(i);



        % Find the error between the known stress and the calculated
        % best fit stress.

        currenterr = currenterr + sum(abs(y(n:i)-newy1))+
sum(abs(y(i:length(y))-newy2));

        % If this is the first iteration of the loop set the minimum
        % error equivalent to the current error. Else, if the current
        % error is less than the minimum error set minimum error equal
        % to the current error and store the calculated stress values

        if i == round(0.70*length(x))
            minimumerr = currenterr;
        elseif currenterr < minimumerr
            minimumerr = currenterr;
            critstrain = x(i);
            critstress = y(i);
            critstraint = z1(i);
            critstresst = z2(i);
            lspot = n;
        end


 end
end


 disp(critstrain);

end
```

Parabola Fitting Function

```
function [a,b] = pfit( x,y )
%PFIT calculates the best fit parabola with the y-intercept at the
%     origin

% Generate the different sums required for the best fit parabola
```

```
x2y = sum(x.^2.*y);
xy = sum(x.*y);
x3 = sum(x.^3);
x4 = sum(x.^4);
x2 = sum(x.^2);

A = [x4,x3;x3,x2];
B = [x2y;xy];

ab = linsolve(A,B);

a = ab(1);
b = ab(2);

end
```

Savitzky-Golay Function

```
function [ newx,dydx,true] = SolviskyGolay(n, x, y, d, tr )

%  SolviskyGolay       Calculates the derivative of a function using
%                      the Solvisky-Golay-filtering
%  Input:
%     n          = degree of smoothing used to calculate the derivative
%     x          = vector containing the engineering strain data
%     y          = vector containing the engineering stress data
%     tr         = vector containing the true strain data
%  Output:
%     dydx       = vector containing the calculated derivative
%     newx       = vector containing the corrosponding strain data
%     true       = vector containing the corrosponding true strain
%  Author:
%     Ryan Milligan, ryanmilligan10@gmail.com
%     Texas A&M University, Civil Engineering Department
%     14 April 2013

% Find the step sized used on each side of point to avegarge the values
del = ((n-1)/2);

% Initialize the dydx and newx vectors before the loop
dydx = zeros(length(x)-2*del,1);
newx = zeros(length(d),1);

% Loop through each data point and calculate the slope of the best fit
line
for i = (1+del):length(x)-del;

    % Calculate the coefficients for the best fit polynomial
    Coeff = polyfit(x(i-del:i+del),y(i-del:i+del),d);

    %Calculate the derivative and corrosponding strain
```

```
    dydx(i-del,1) = 2*Coeff(1)*x(i)+ Coeff(2);
    newx(i-del,1) = x(i);
    true(i-del,1) = tr(i);
end

end
```

Total Regularization Function

```
function [ z , d] = TotalRegularization( y, x, lambda)

%TOTALREGULARIZATION Smooth data using the total regularization
%                     technique
%  Input:
%     y         = engineering strain
%     x         = engineering stress
%     lambda    = smoothing parameter
%  Output:
%     z         = new stress values
%     d         = corresponding strain values
%  Author:
%     Ryan Milligan, ryanmilligan10@gmail.com
%     Texas A&M University, Civil Engineering Department
%     14 April 2013

 m = length(y);
E = speye(m);
D = diff(E,3);
C = chol(E+lambda.*transpose(D)*D);
z = C\(transpose(C)\y);

for i = 1:length(z)-1
    d(i,1) = (z(i)-z(i+1))/(x(i)-x(i+1));
end

end
```

Critical Strain Calculation for Slope-Strain Curves Function

```
function [critstrain,line1,line2] = critstrain(d,s)
%  CritStrainCalc      Calculates the critical strain of trimmed data
%                      by taking the derivative and finding the knee in
%                      the data
%  Input:
%     d           = vector containing the derivative of the engineering
%                   stress vs strain data
%     s           = vector containing strain data corresponding to the
%                   derivative array d
%  Output:
%     critstrain  = critical strain calculated from the d and s vectors
%
%  Author:
```

```
%     Ryan Milligan, ryanmilligan10@gmail.com
%     Texas A&M University, Civil Engineering Department
%     14 April 2013

% Loop through all the data points in the derivative vector d

for i = 2: length(d)-1
    % Best fit line for data 1 to i

    % Calculate the slope and y-int for the best fit line

    coeff1 = polyfit(s(1:i),d(1:i),1);

    % Find the error between the actual data and the best fit line

    currenterror = sum(abs(d(1:i)-polyval(coeff1,s(1:i))));

    % Best fit line for data i to length(d) i.e. end of data vector

    % Calculate the slope and y-int for the best fit line

    coeff2 = polyfit(s(i:length(d)),d(i:length(d)),1);

    % Find the error between the actual data and the best fit line

    currenterror = currenterror + sum(abs(d(i:length(d))-
polyval(coeff2,s(i:length(d)))));

    % Initialize the first value of currentmin

    if i <= 3
        minerror = currenterror;
    else
        if currenterror < minerror
            minerror = currenterror;
            line1 = polyval(coeff1,s);
            line2 = polyval(coeff2,s);
            critstrain = (coeff2(2) - coeff1(2)) / (coeff1(1) -
coeff2(1));
        end
    end
end

end
```

APPENDIX B

Laser Evaluation Scans

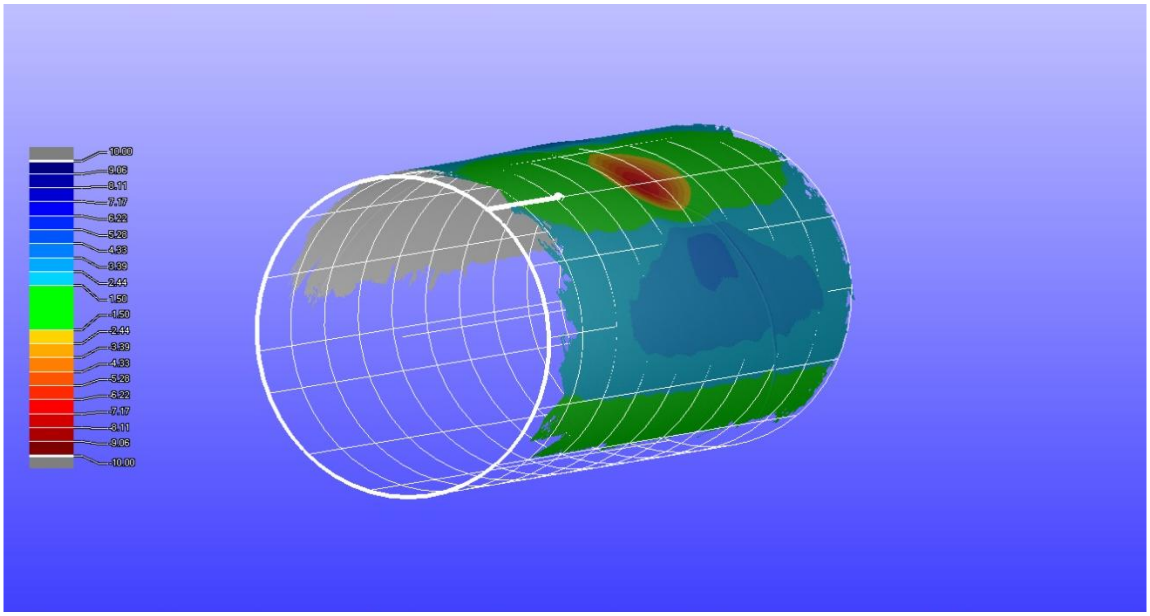

Figure B1: 180 OD 1mm Scan

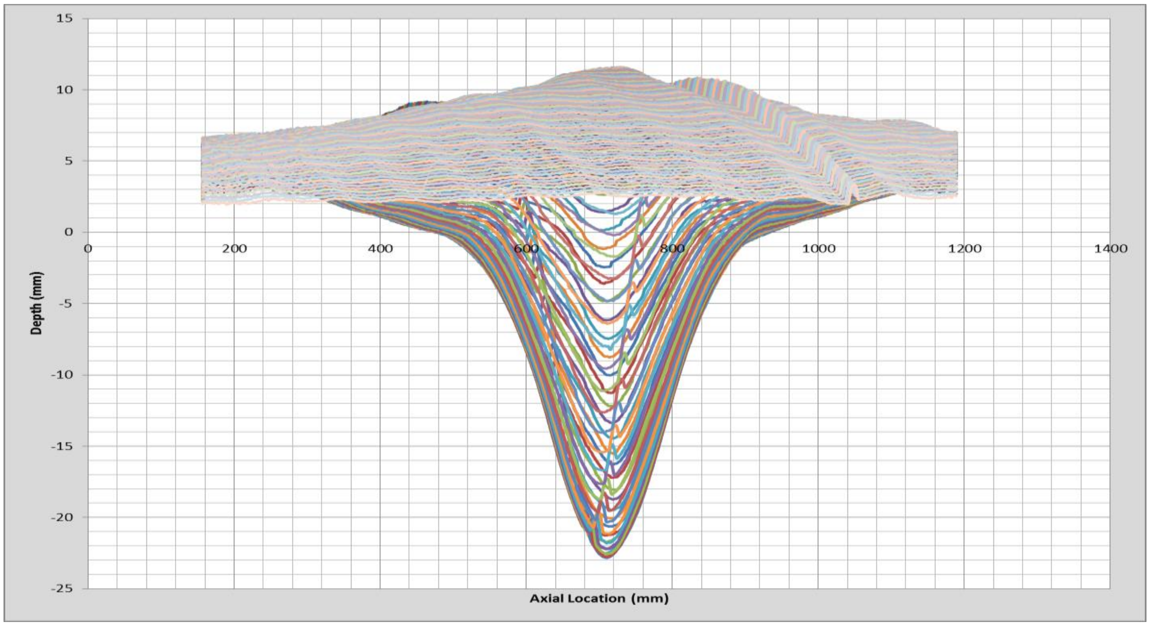

Figure B2: 180 OD 1mm Scan

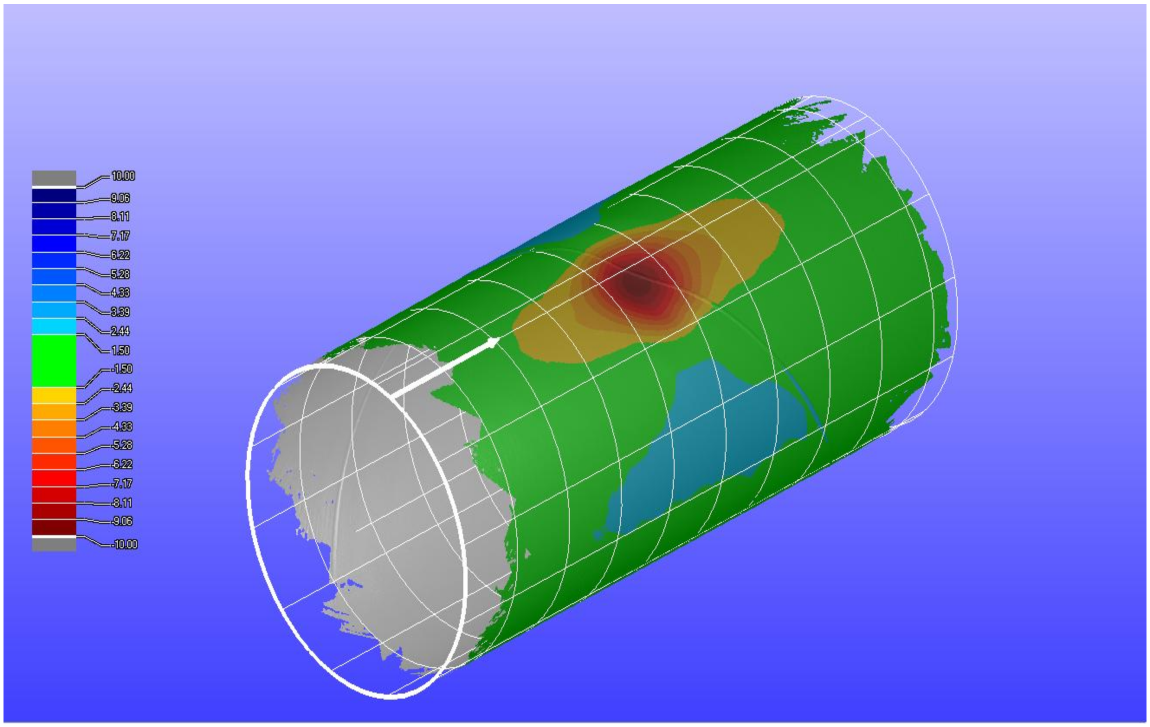

Figure B3: 360 OD Scan

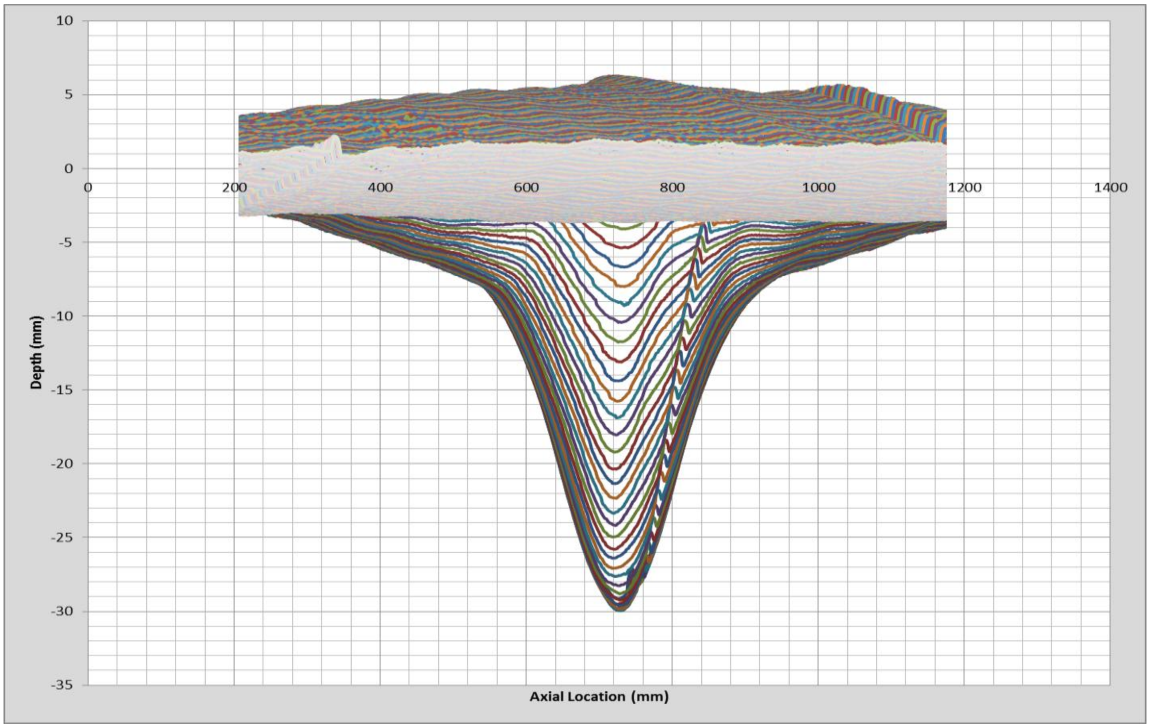

Figure B4: 360 OD 1mm Depth Profile

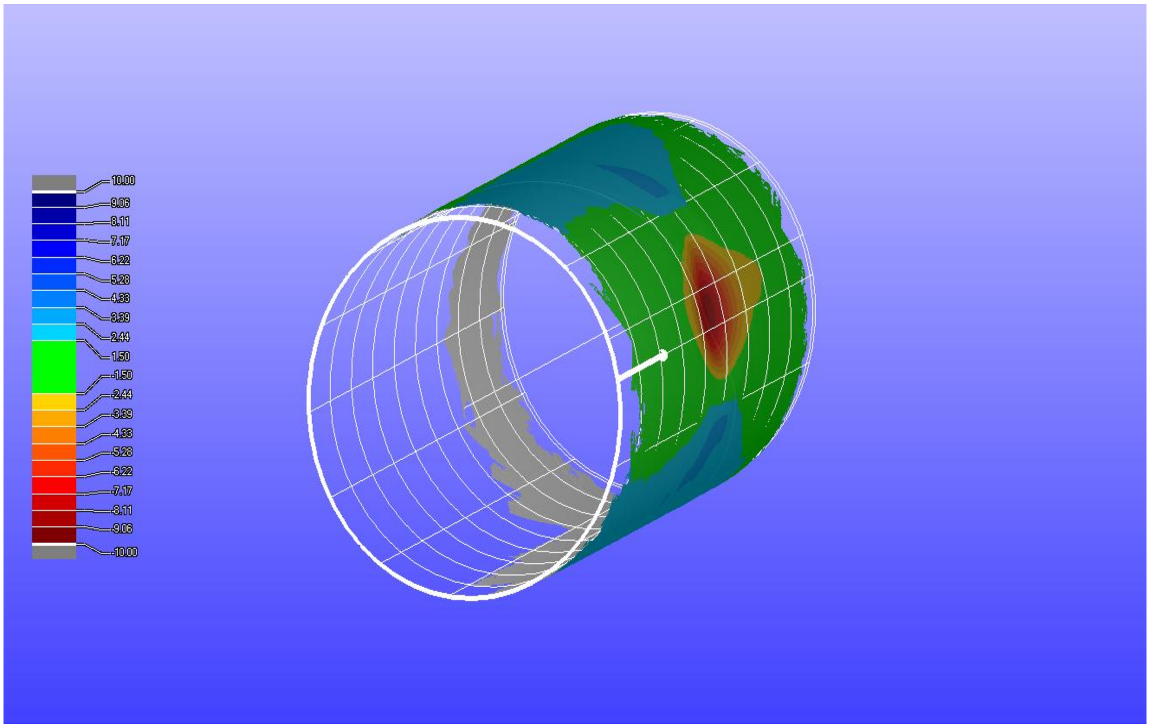

Figure B5: 180 OD Scan with 360 Ring Scan

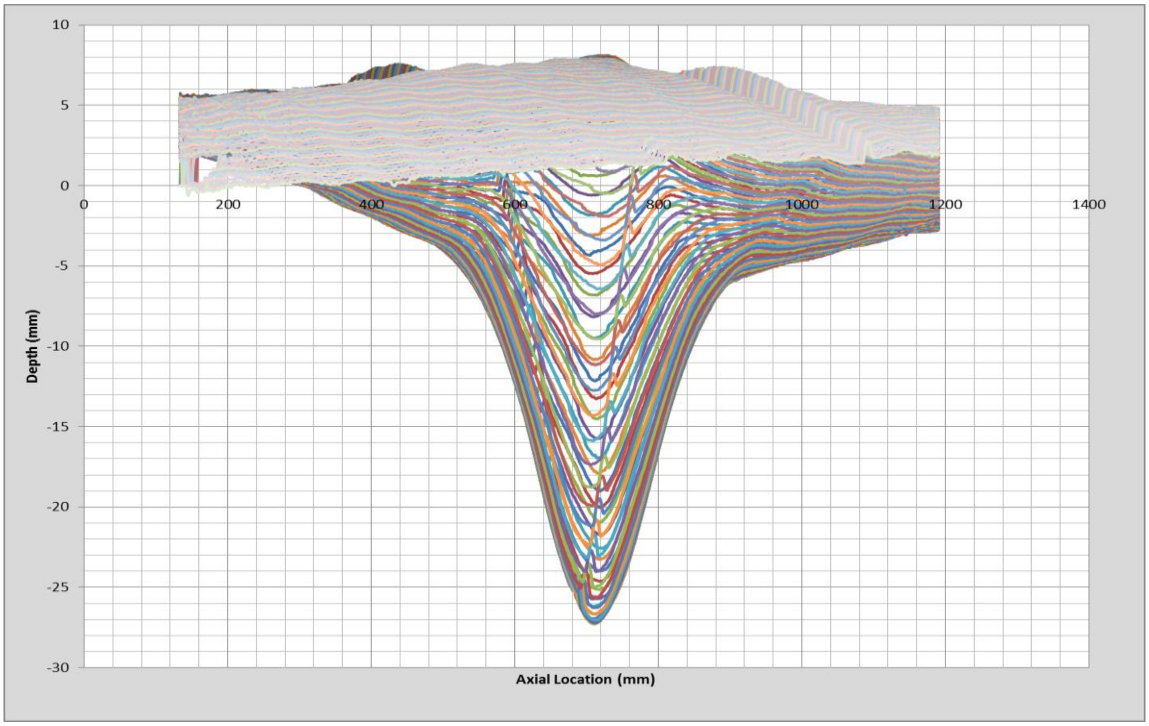

Figure B6: 180 OD Scan with 360 Ring Scan

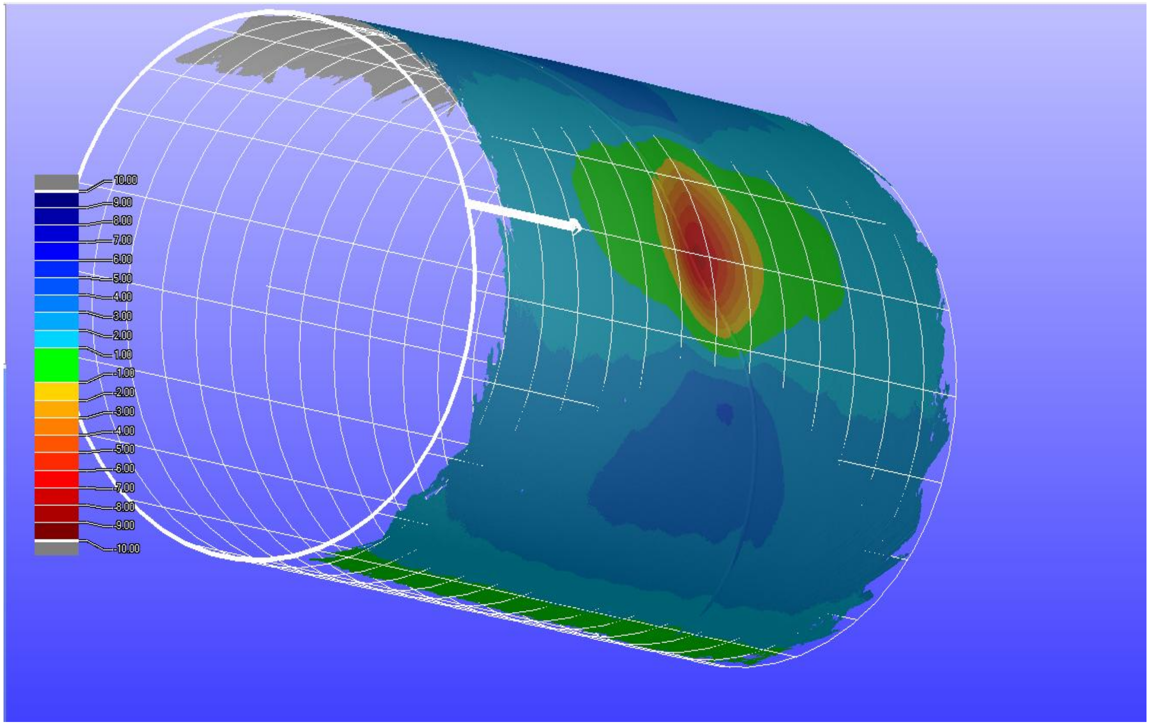

Figure B7: 180 OD 1mm with 0.20mm Dent Region Scan

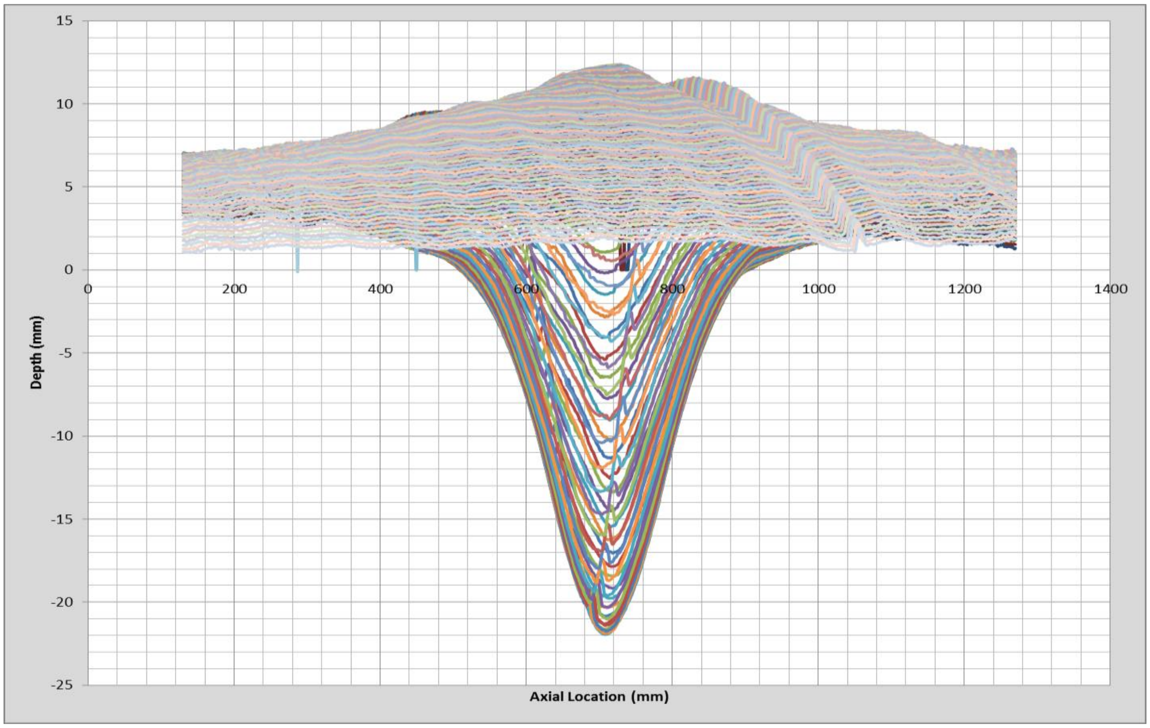

Figure B8: 180 OD 1mm with 0.20mm Dent Region Depth Profile

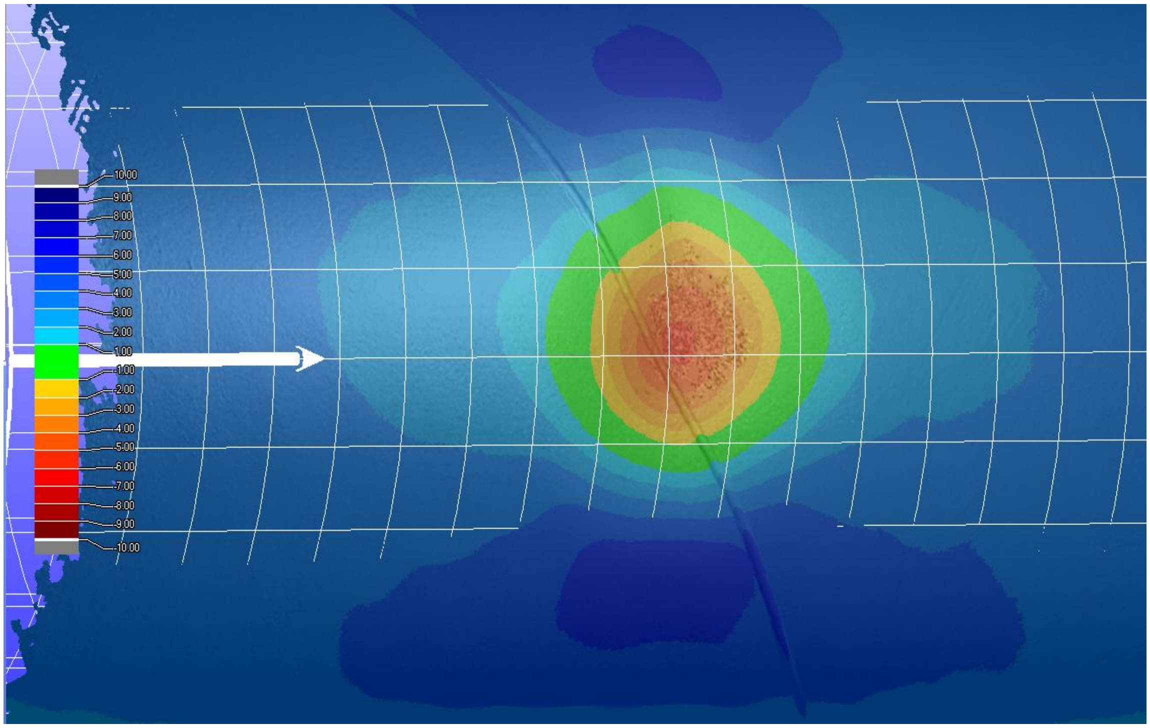

Figure B9: 180 OD 1mm with High Resolution Button Scan

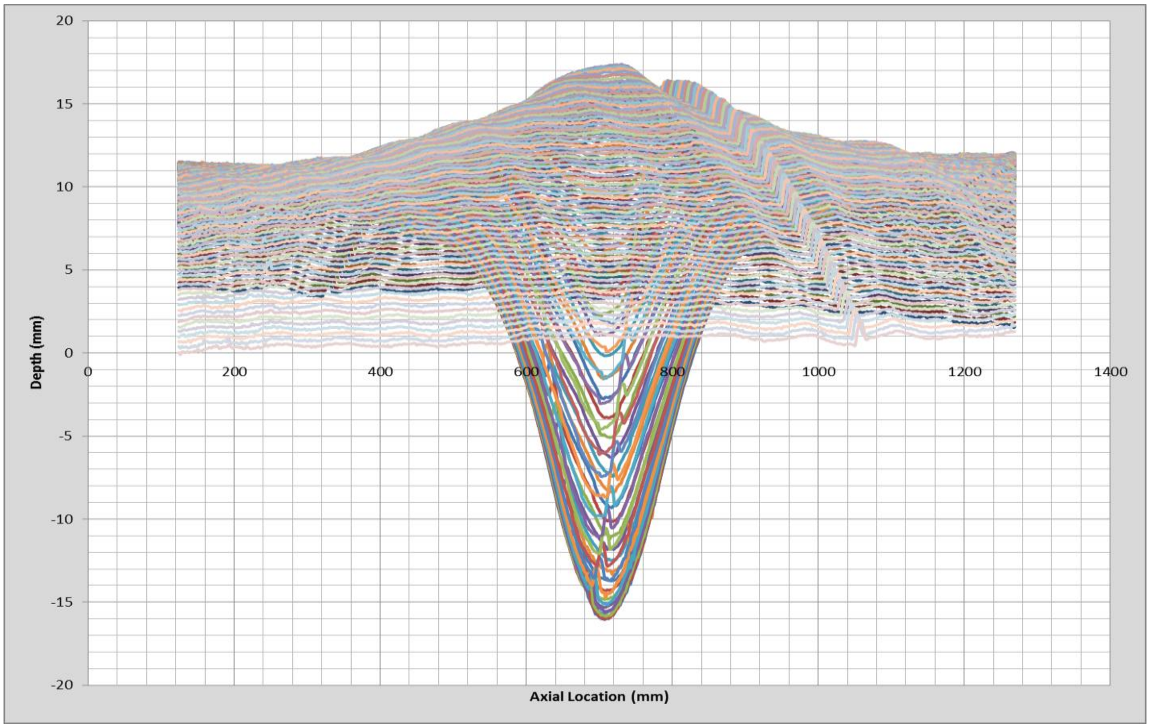

Figure B10: 180 OD 1mm with High Resolution Button Depth Profile

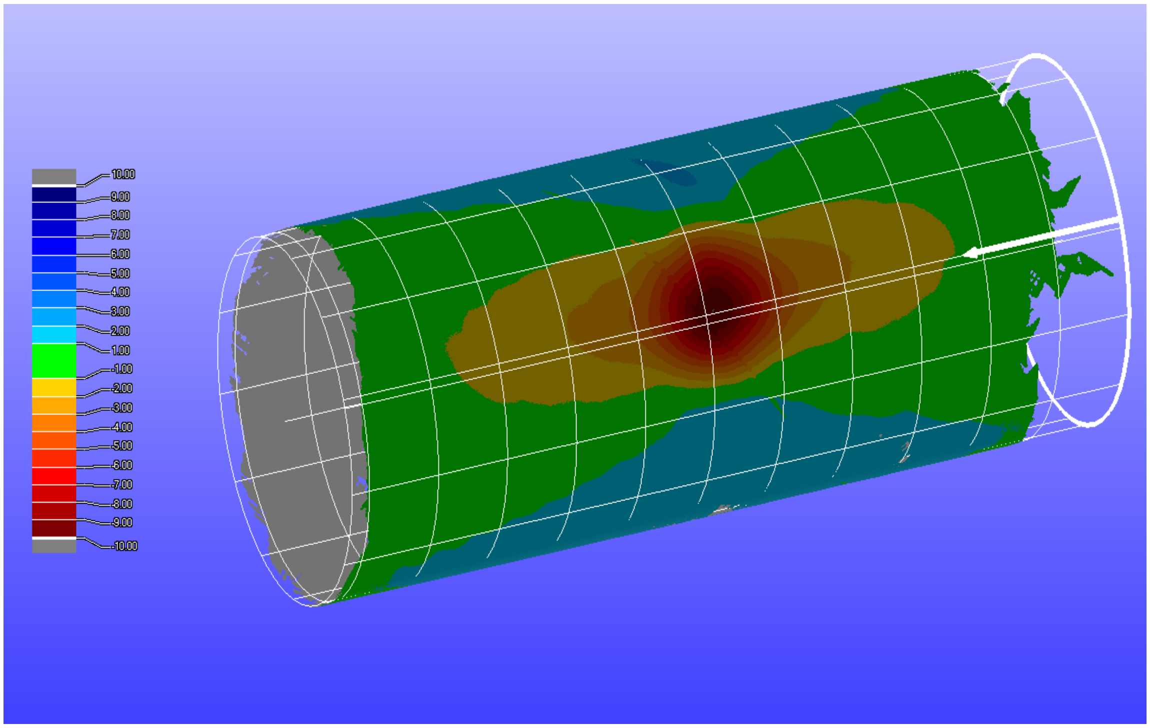

Figure B11: 360 ID 1mm Scan

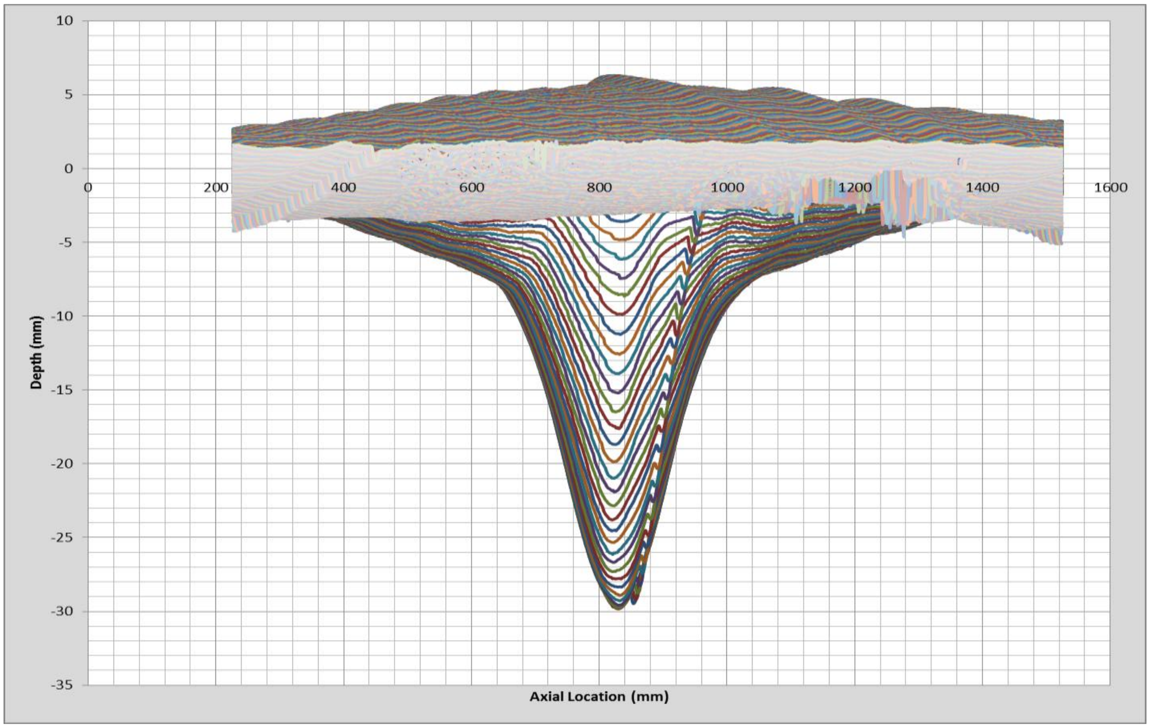

Figure B12: 360 ID 1mm Depth Profile

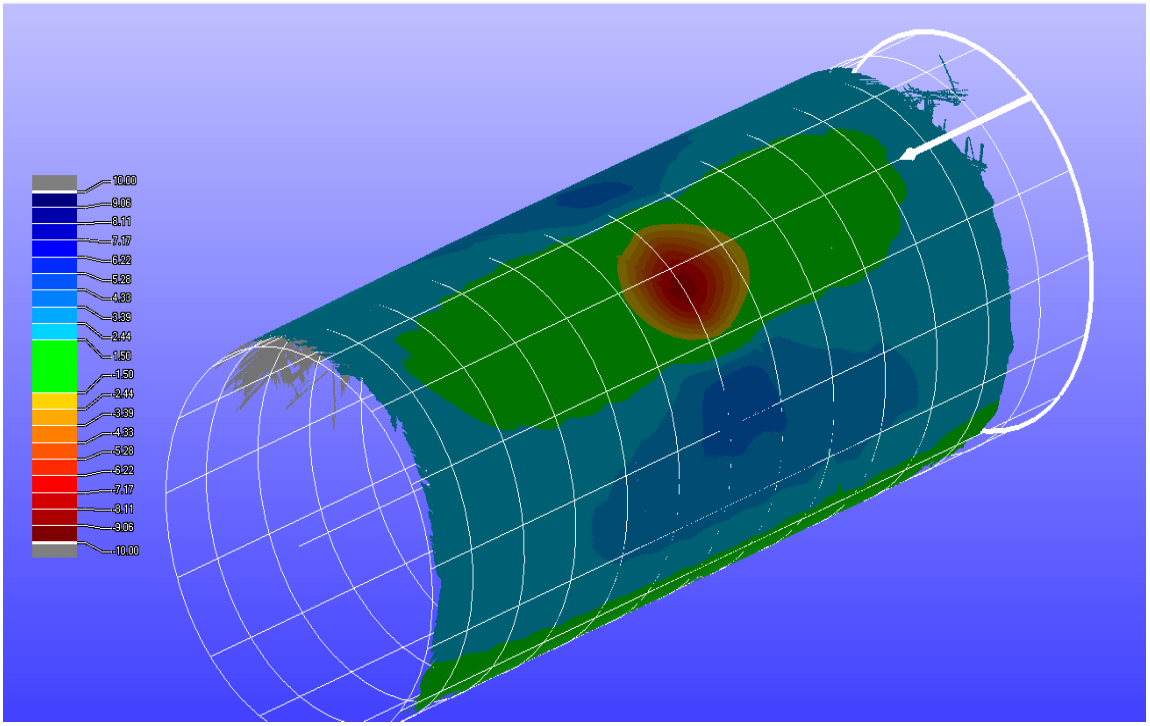

Figure B13: 180 ID 0.5mm Scan

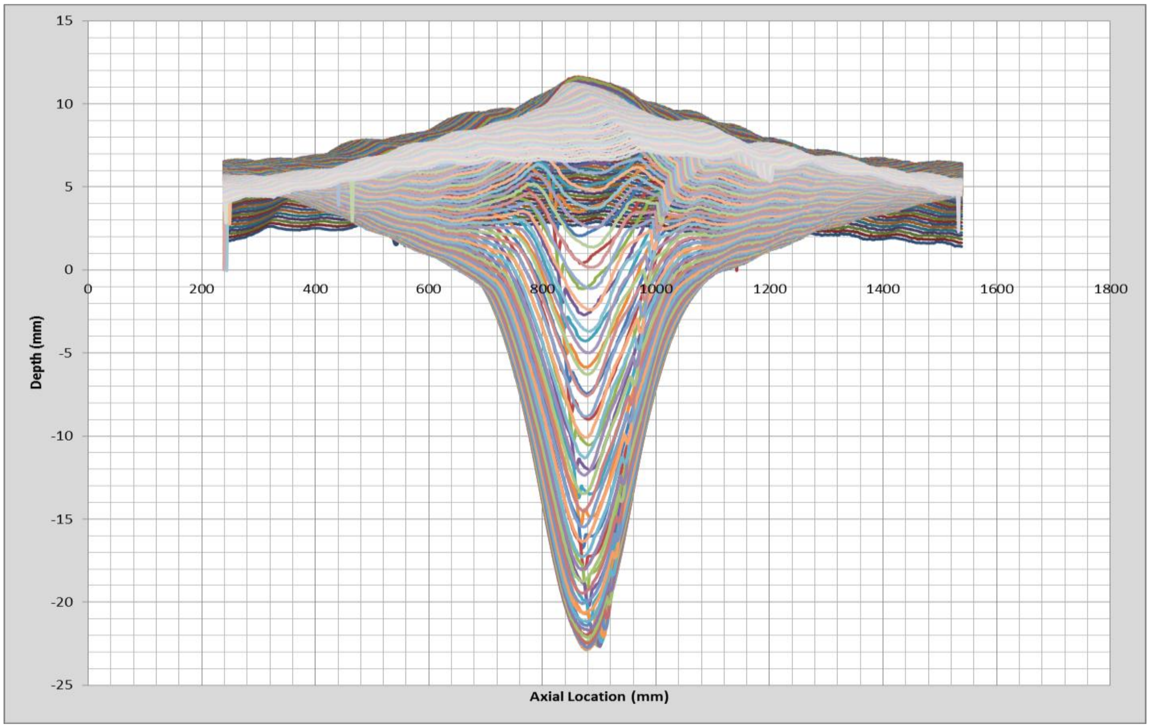

Figure B43: ID 180 0.5mm Depth Profile

Denting Scans

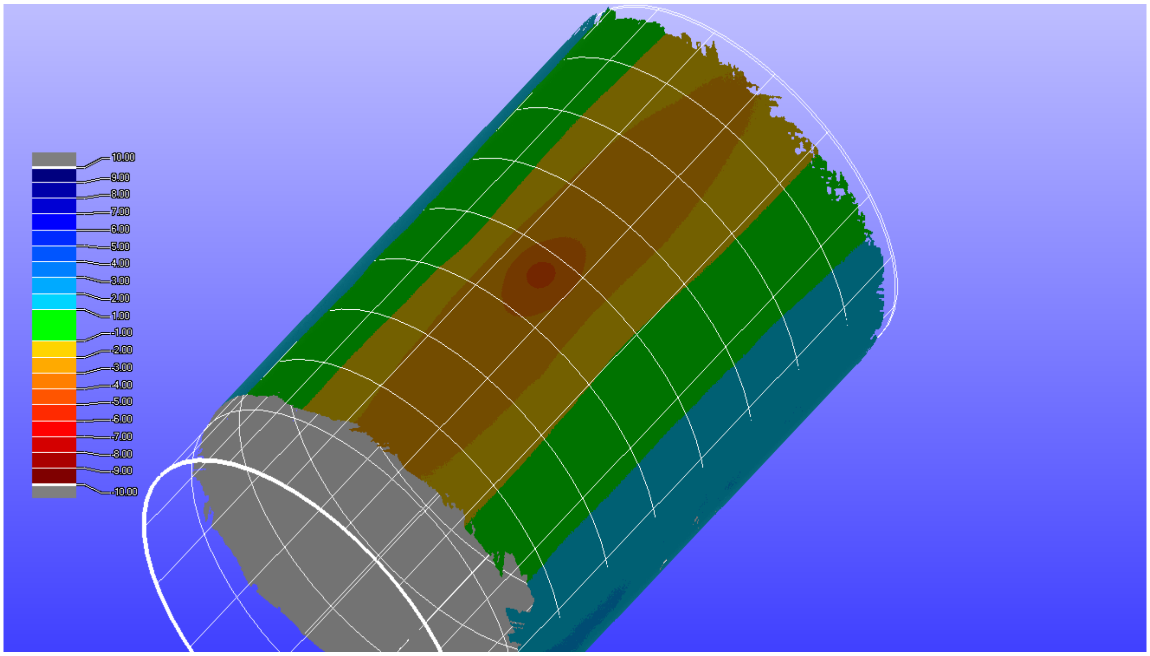

Figure B15: 3% Dent Scan

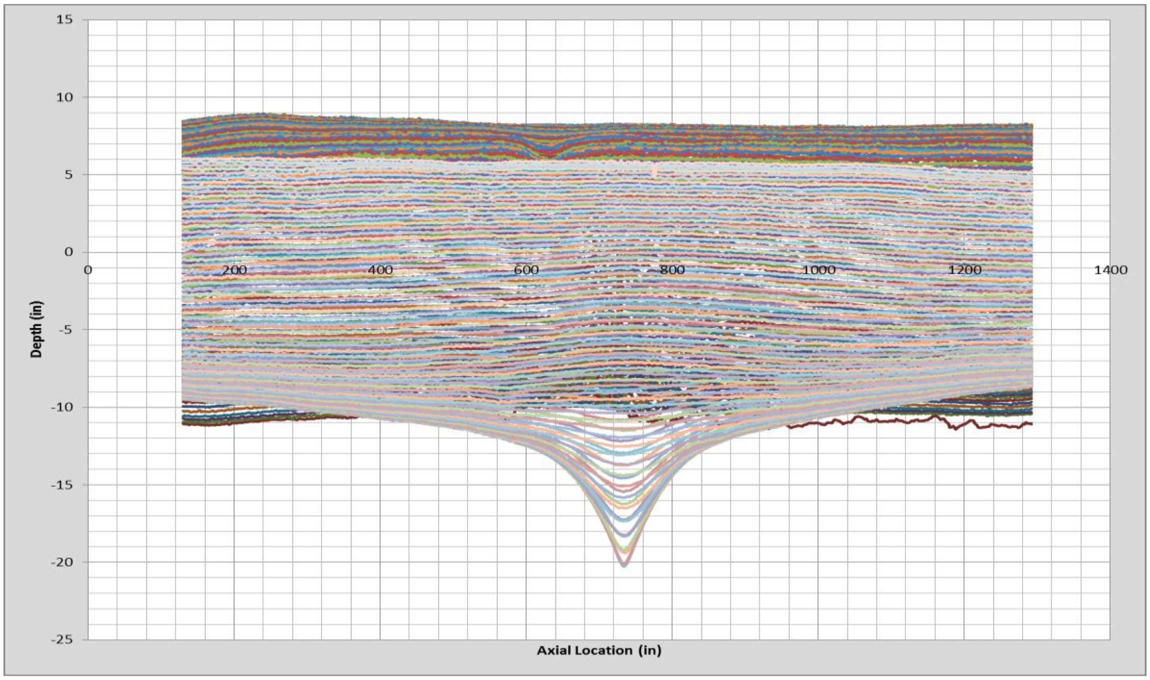

Figure B16: 3% Dent Profile

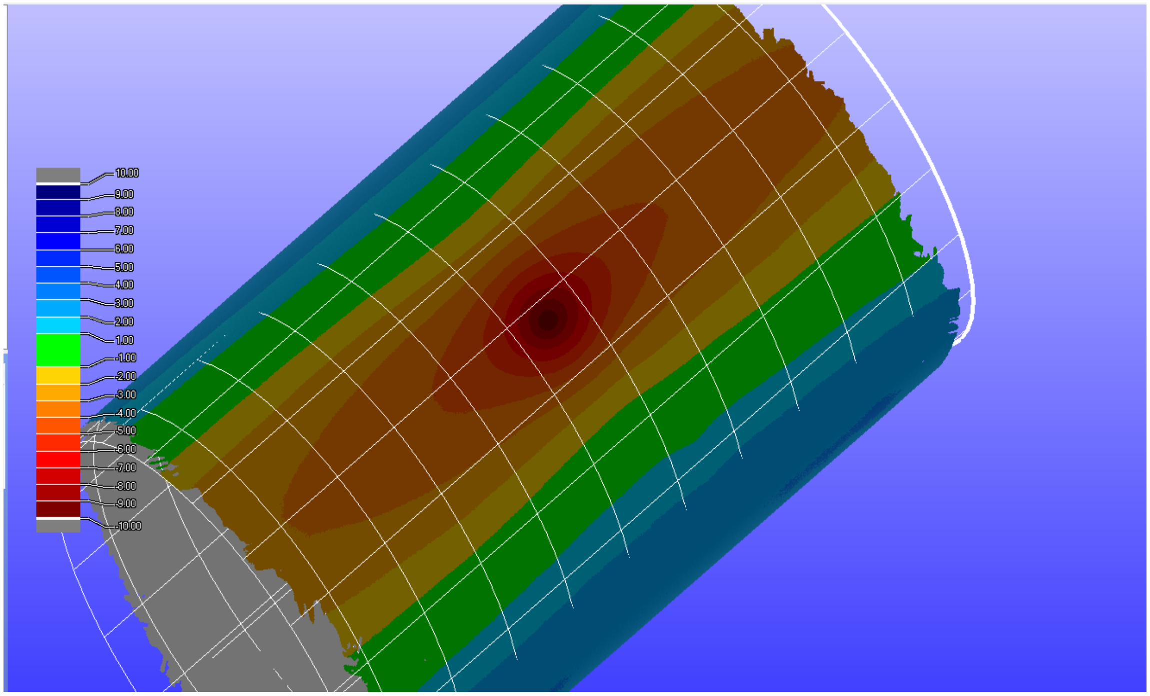

Figure B17: 6% Dent Scan

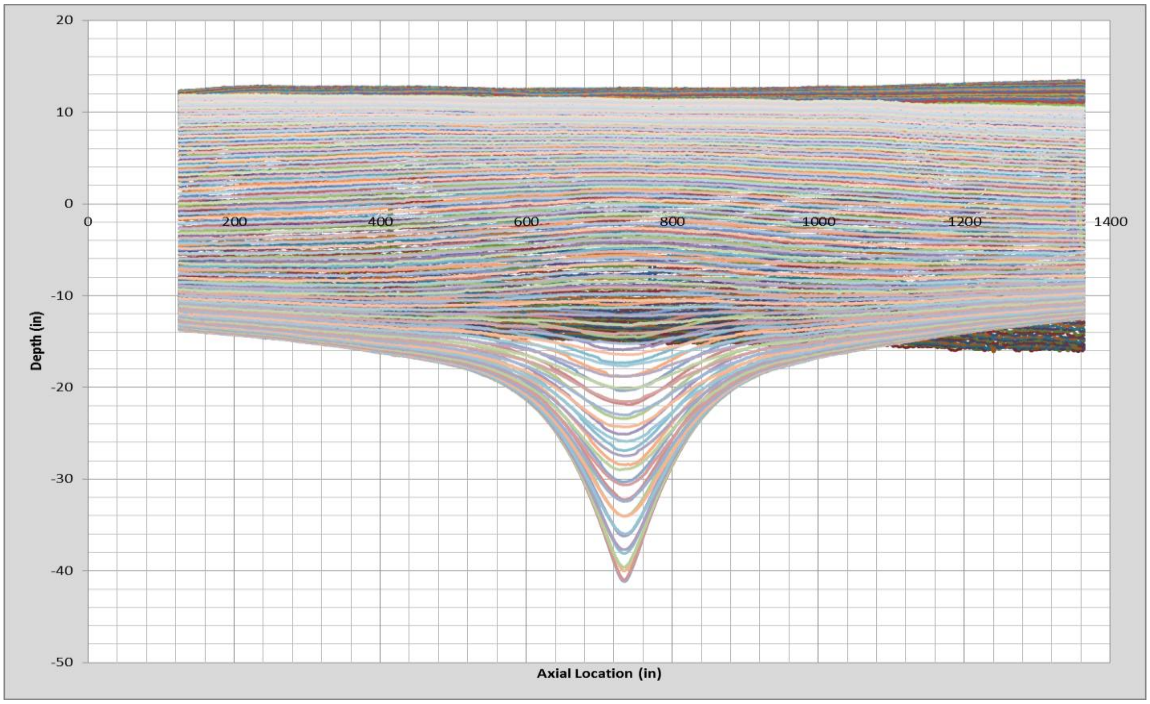

Figure B18: 6% Dent Profile

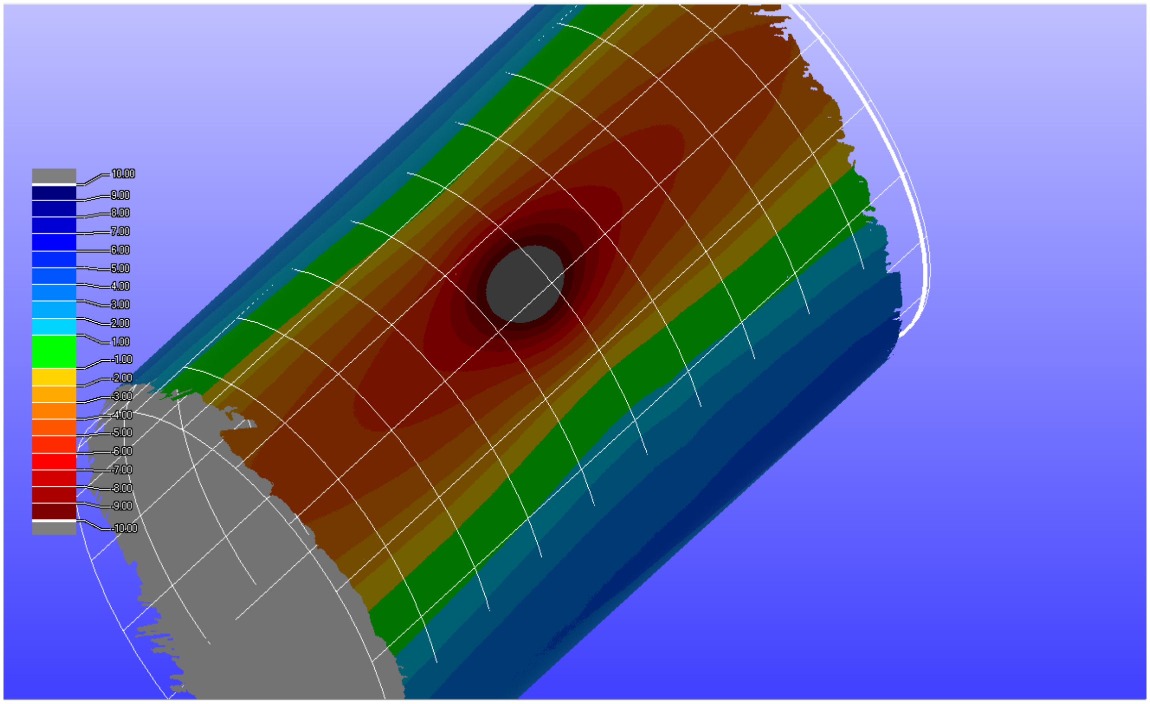

Figure B19: 9% Dent Scan

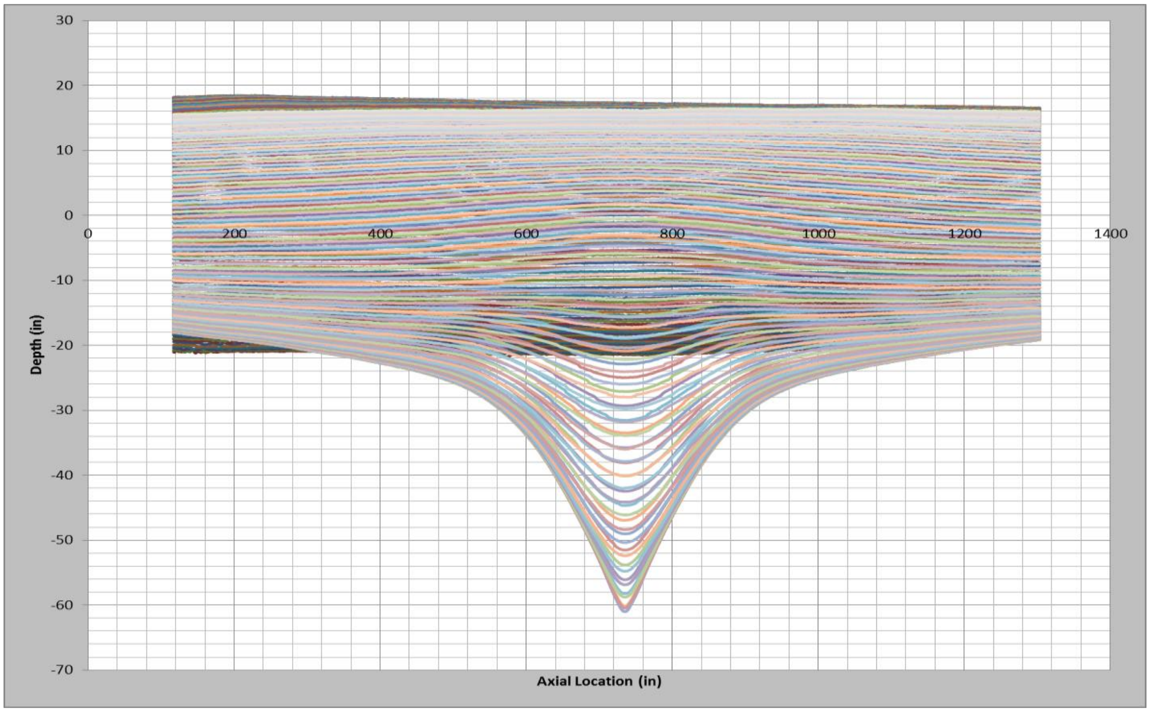

Figure B20: 9% Dent Profile

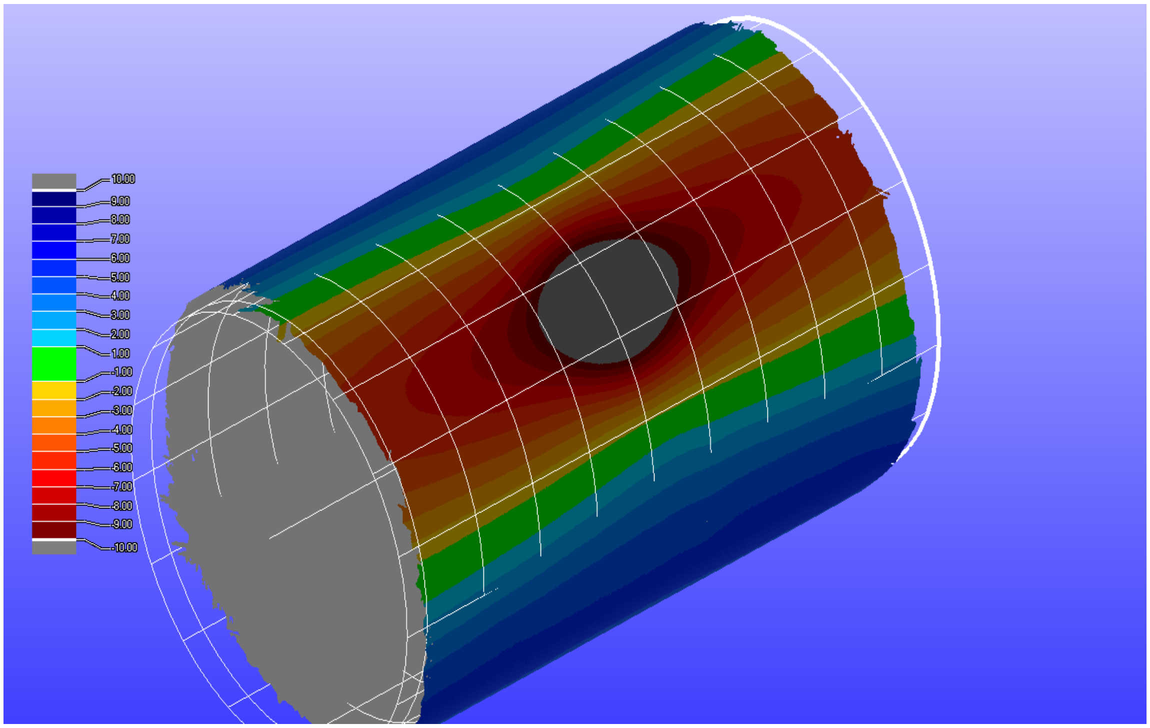

Figure B21: 12% Dent Scan

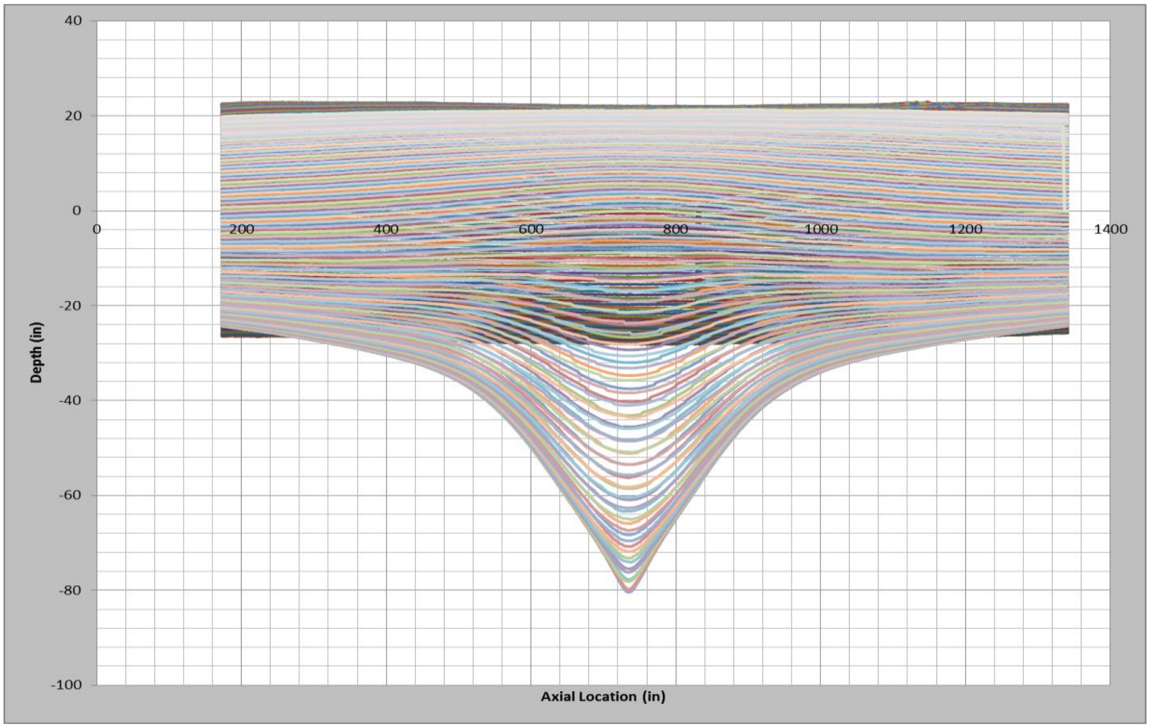

Figure B22: 12% Dent Profile

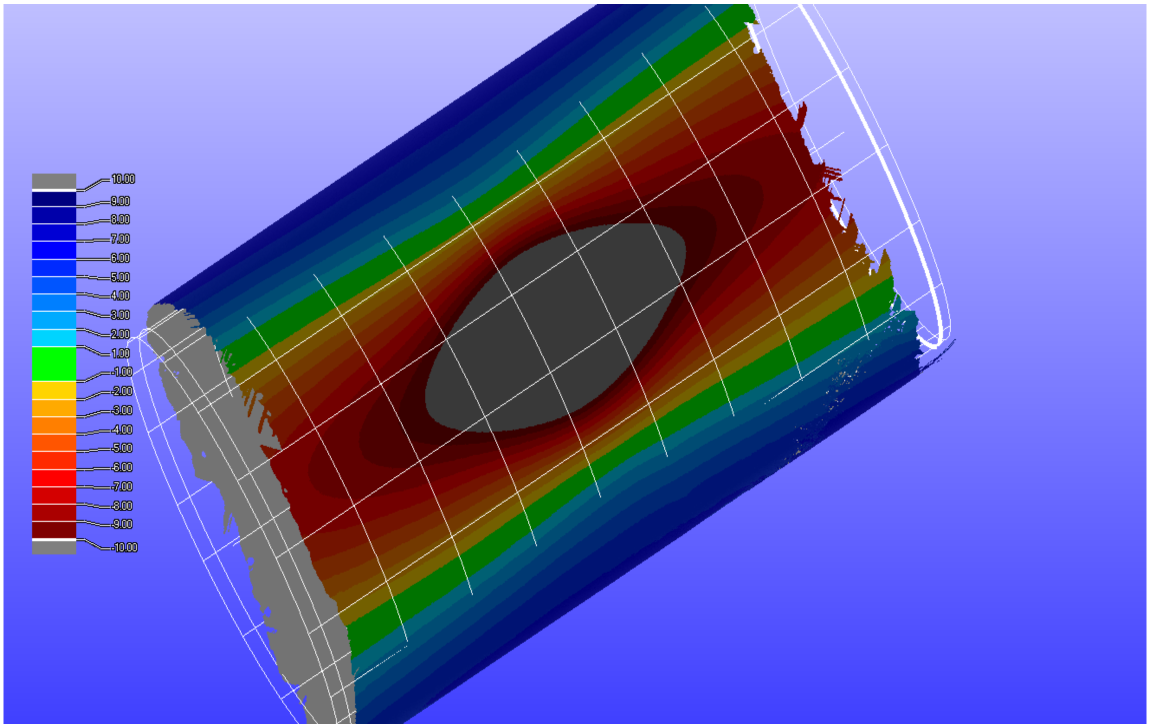

Figure B23: 15% Dent Scan

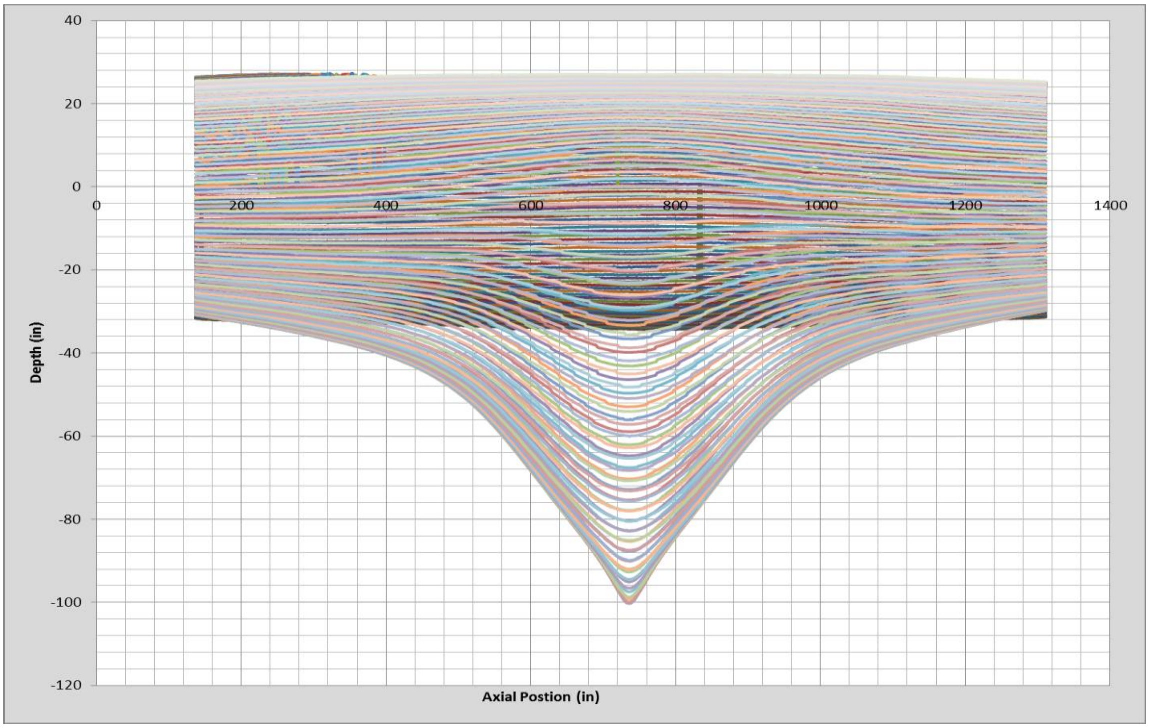

Figure B24: 15% Dent Profile

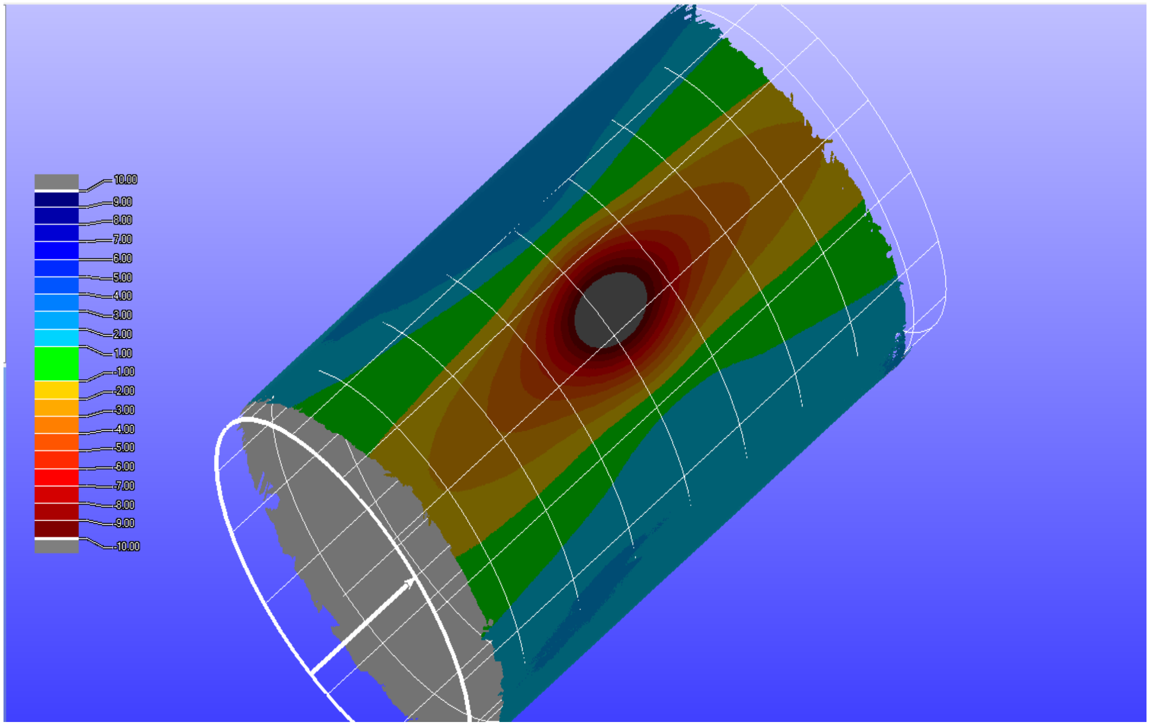

Figure B25: Reround Dent Scan

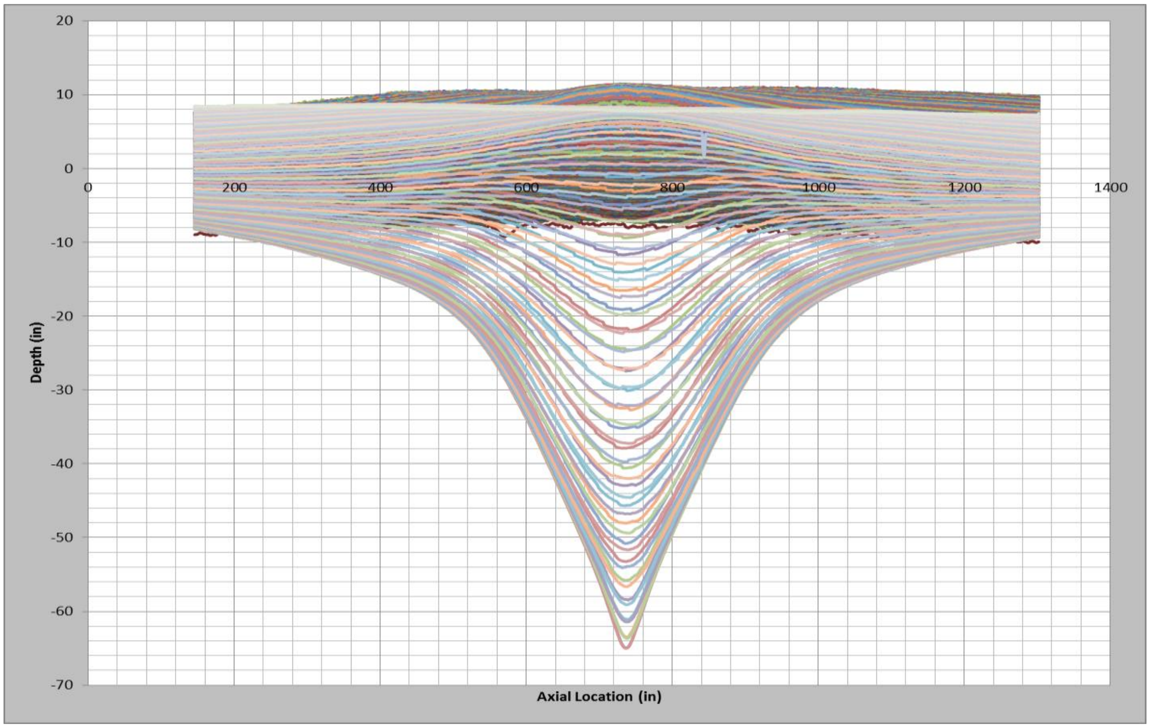

Figure B26: Reround Dent Profile

APPENDIX C

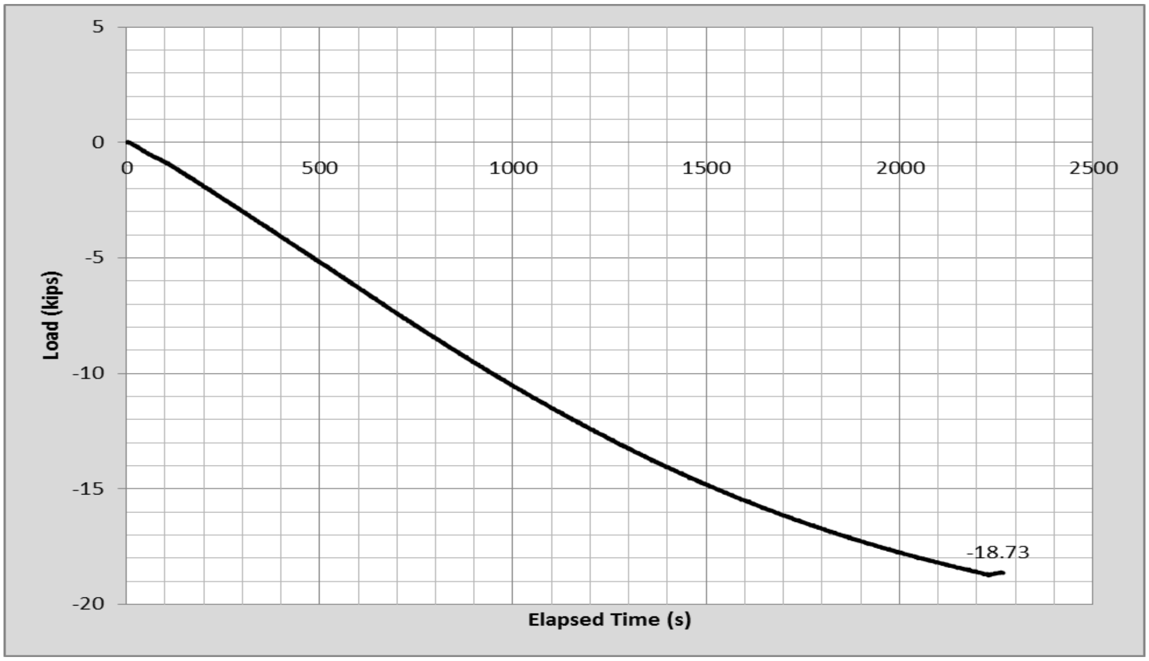

Figure C1: 3% Step Load vs. Time

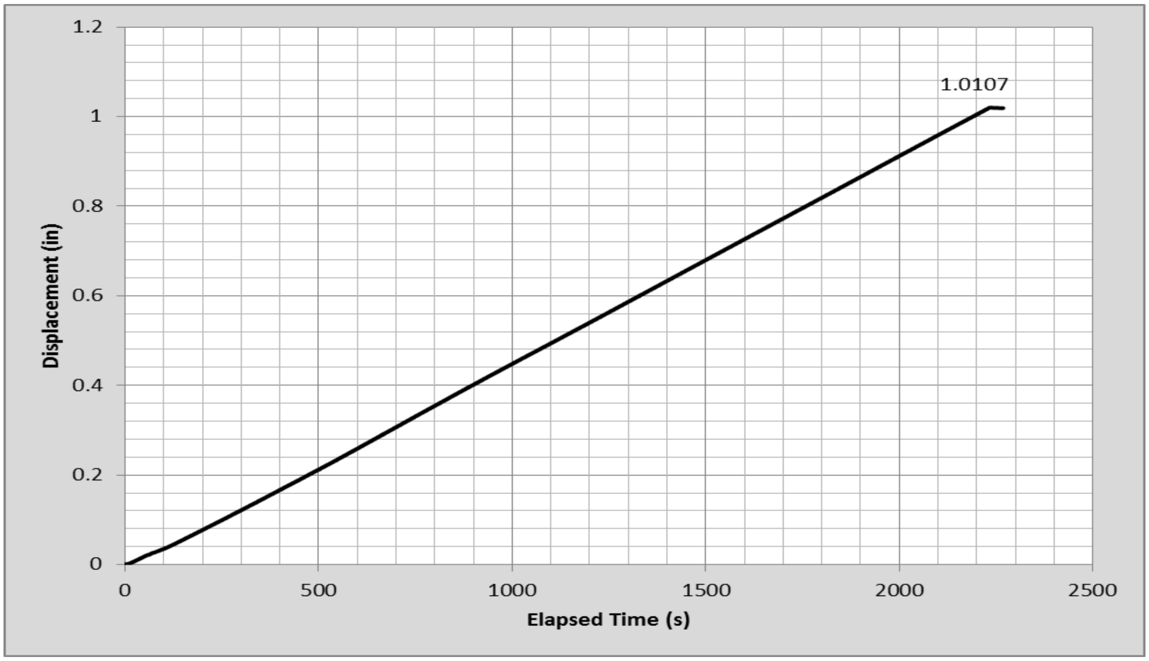

Figure C2: 3% Vertical LVDT Displacement vs. Time

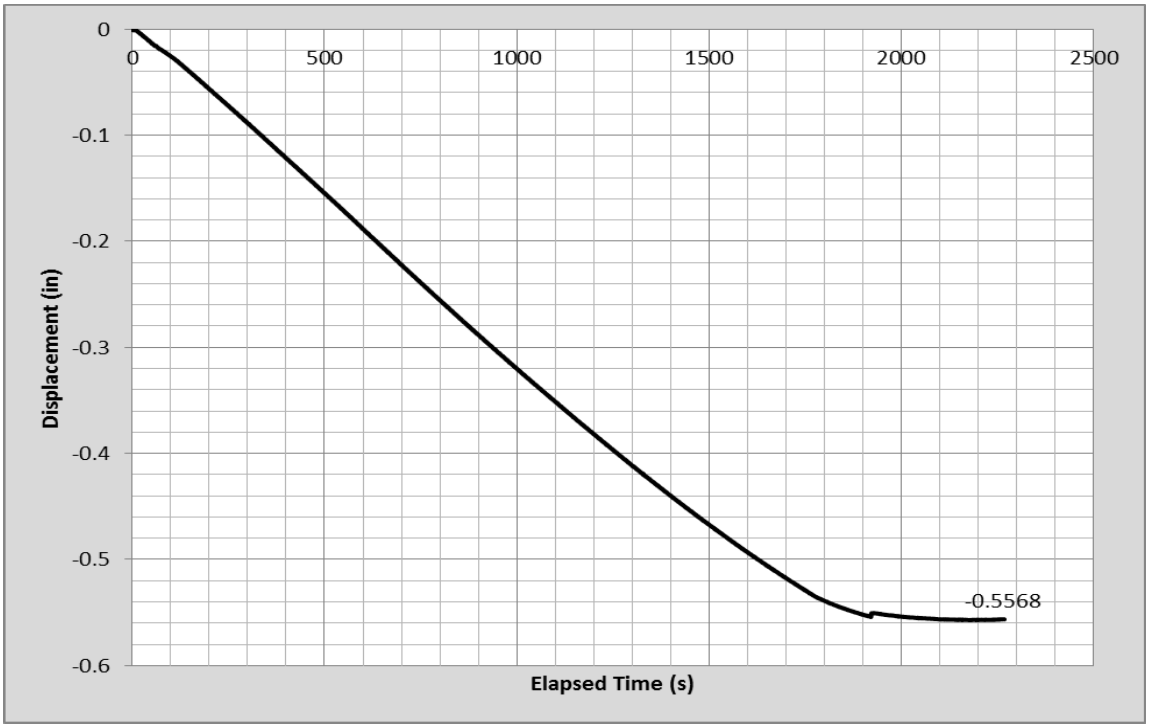

Figure C3: 3% Horizontal LVDT Displacement vs. Time

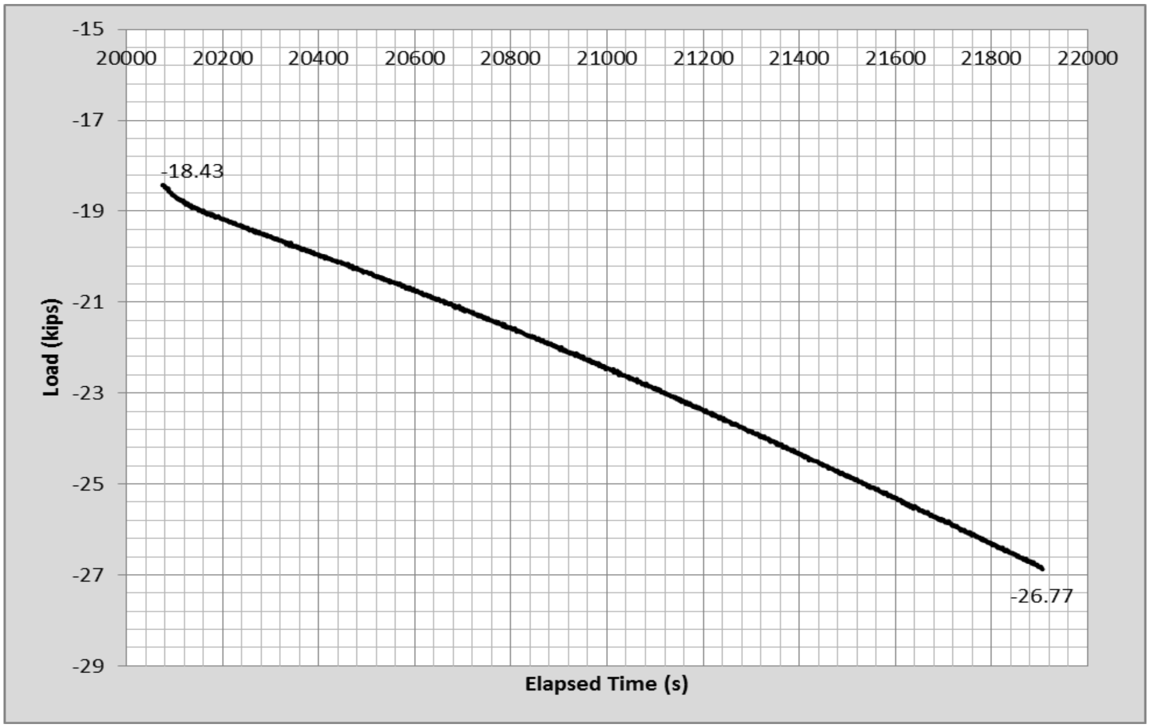

Figure C5: 6% Step Load vs. Time

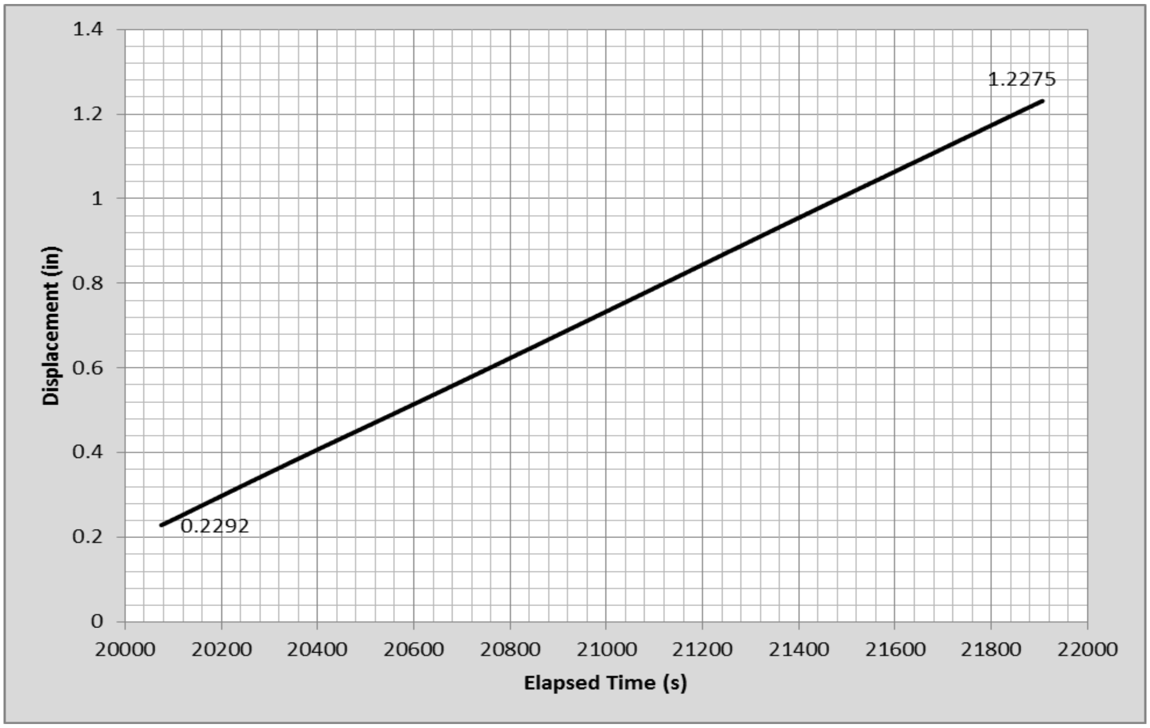

Figure C6: 6% Vertical LVDT Displacement vs. Time

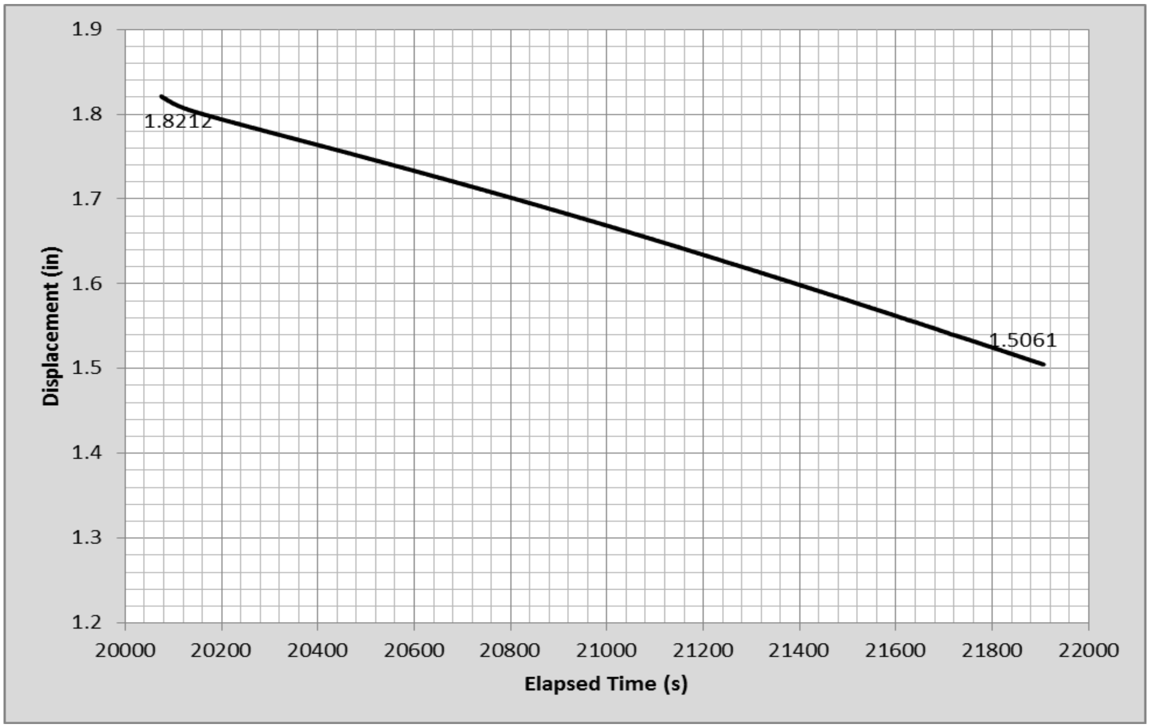

Figure C7: 6% Horizontal LVDT Displacement vs. Time

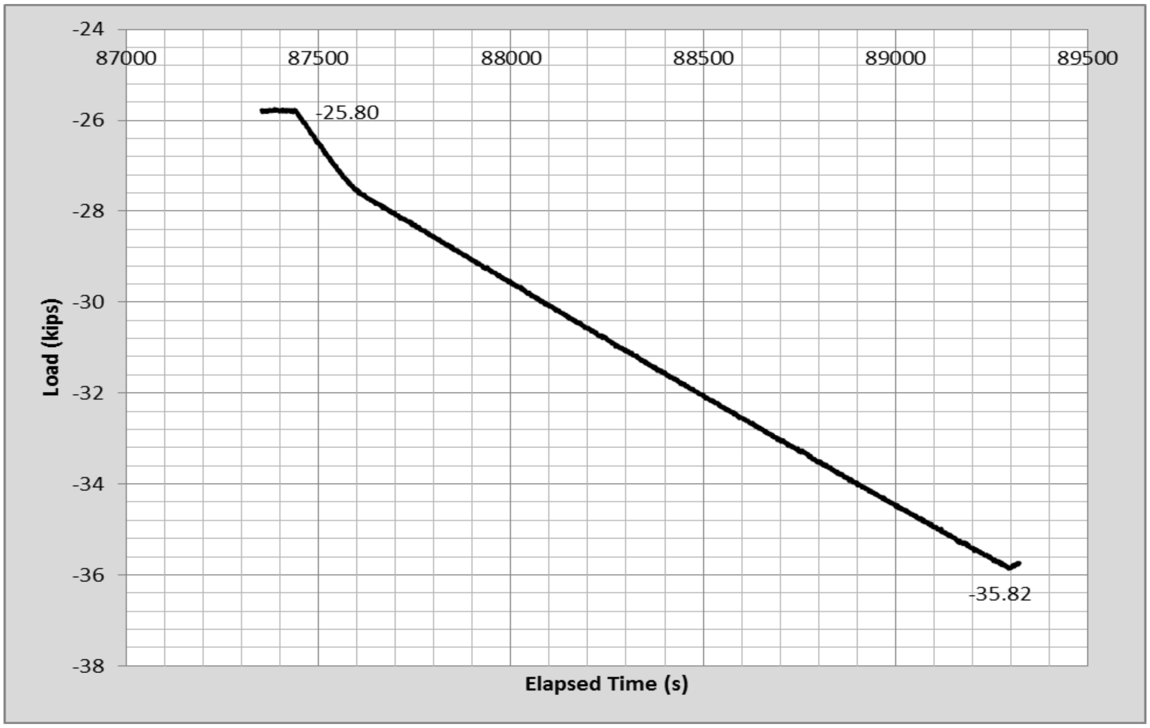

Figure C8: 9% Step Load vs. Time

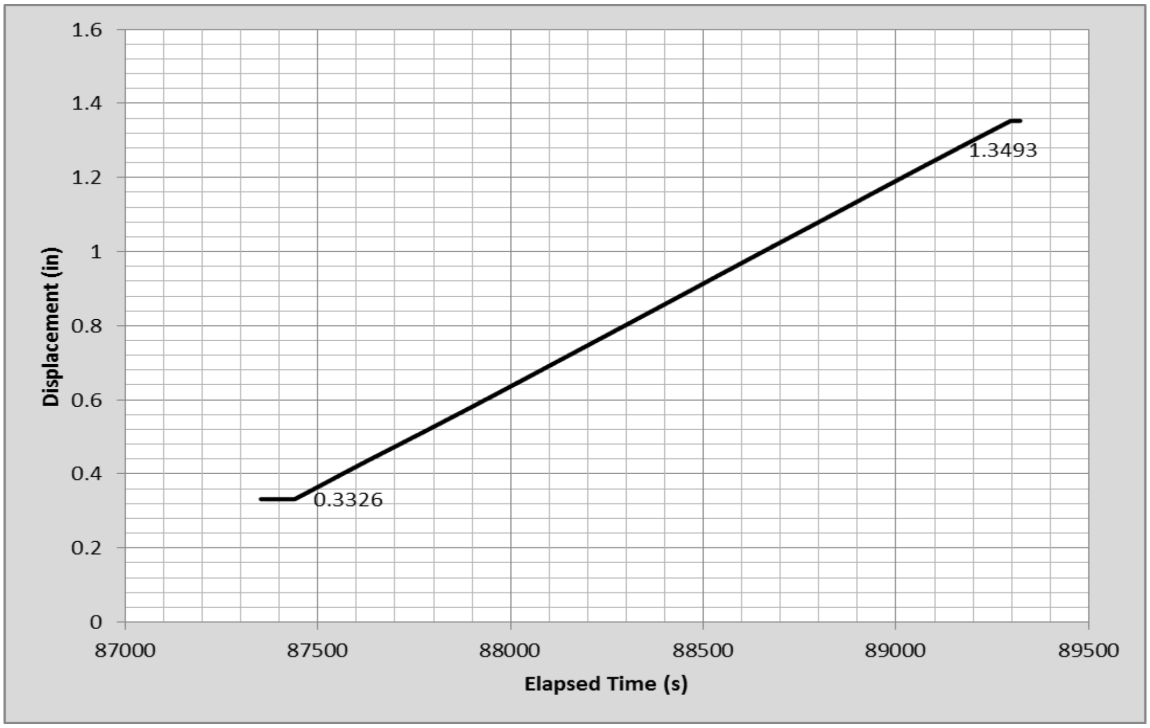

Figure C9: 9% Vertical LVDT Displacement vs. Time

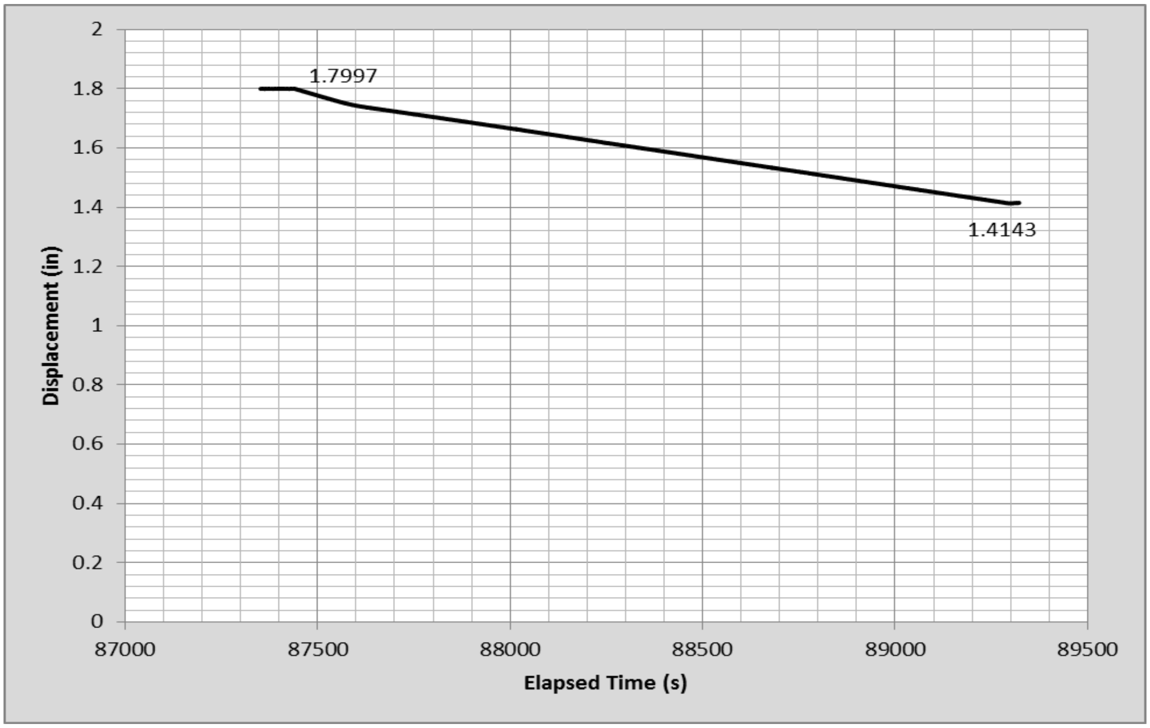

Figure C10: 9% Horizontal LVDT Displacement vs. Time

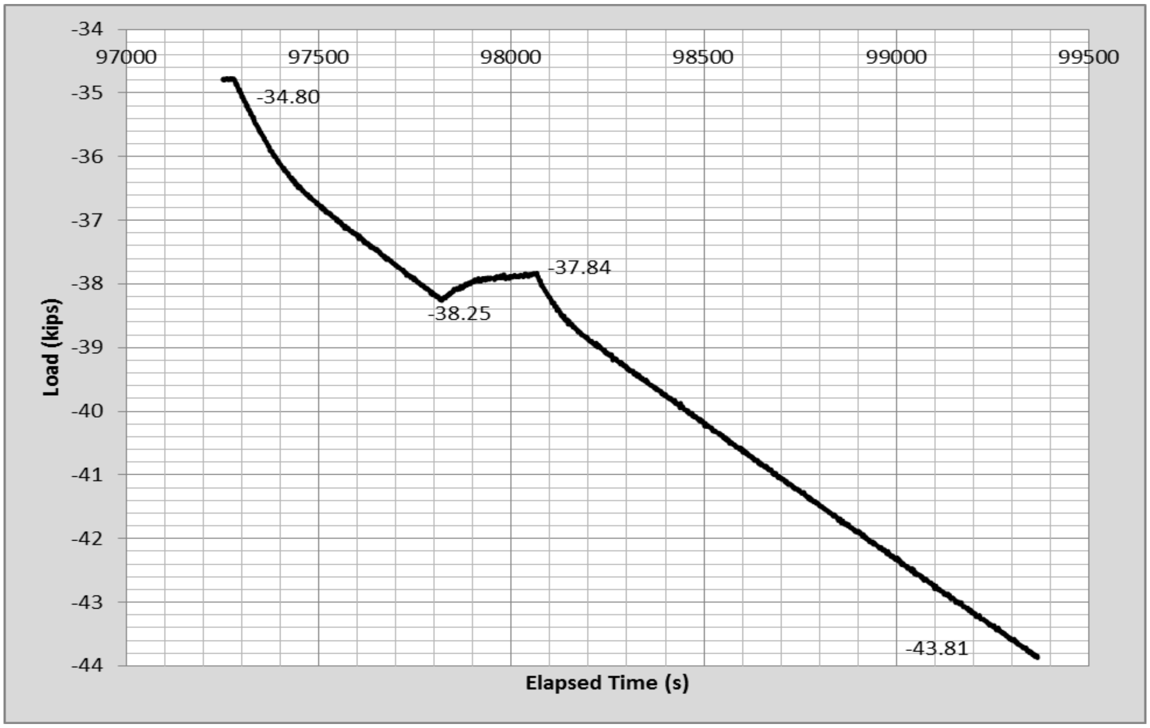

Figure C11: 12% Load vs. Time

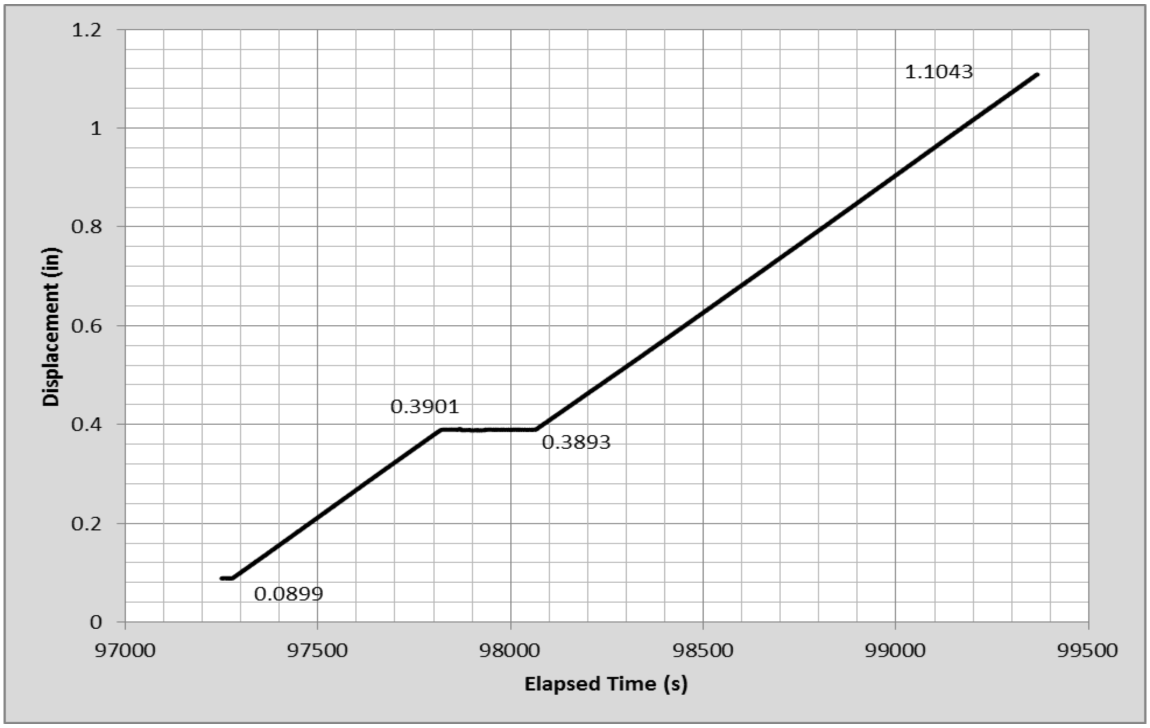

Figure C12: 12% Vertical LVDT Displacement vs. Time

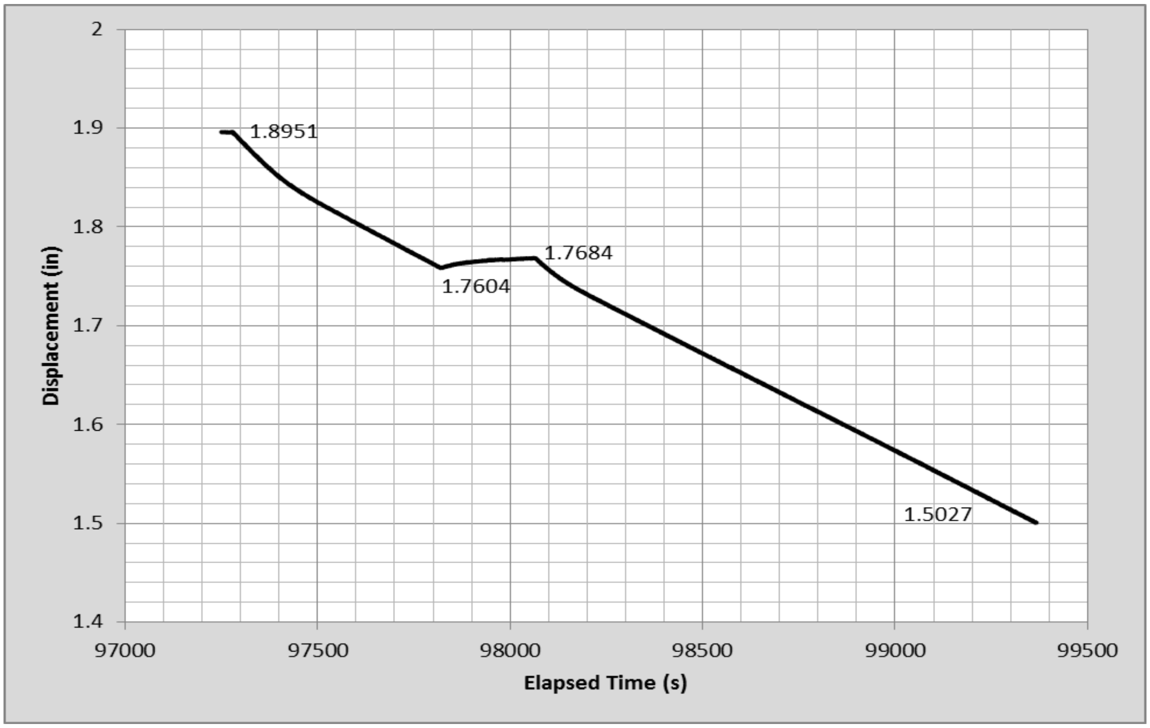

Figure C13: 12% Horizontal LVDT Displacement vs. Time

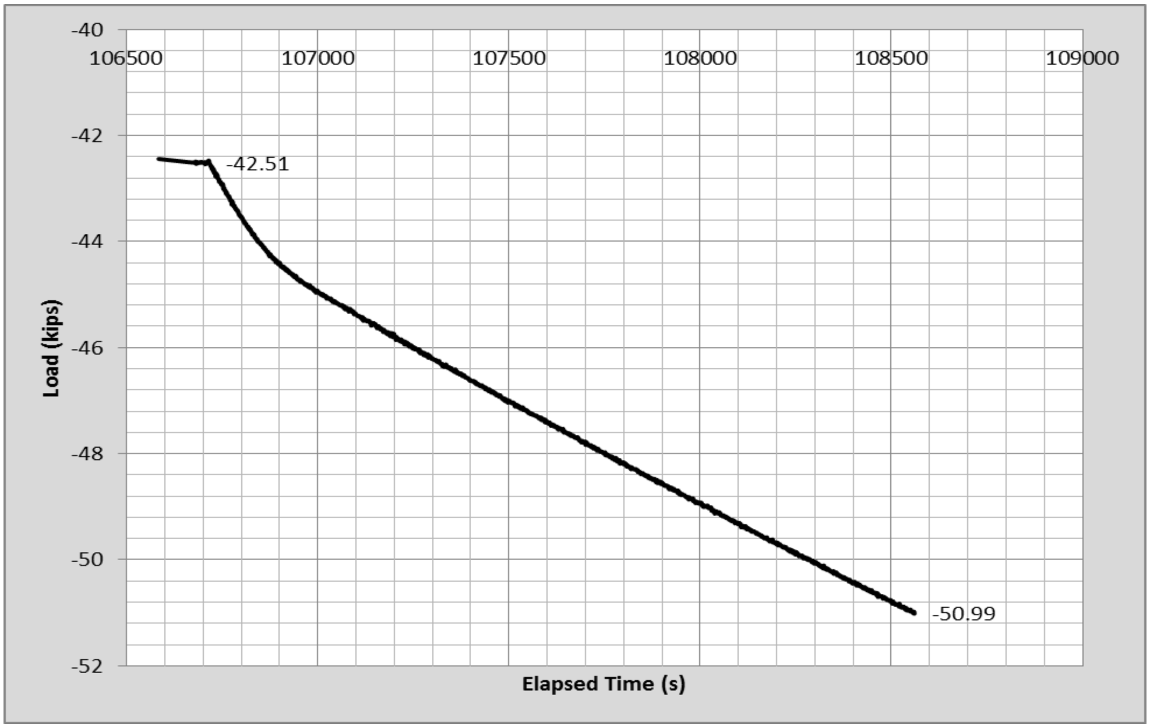

Figure C14: 15% Load vs. Time

Figure C15: 15% Vertical LVDT Displacement vs. Time

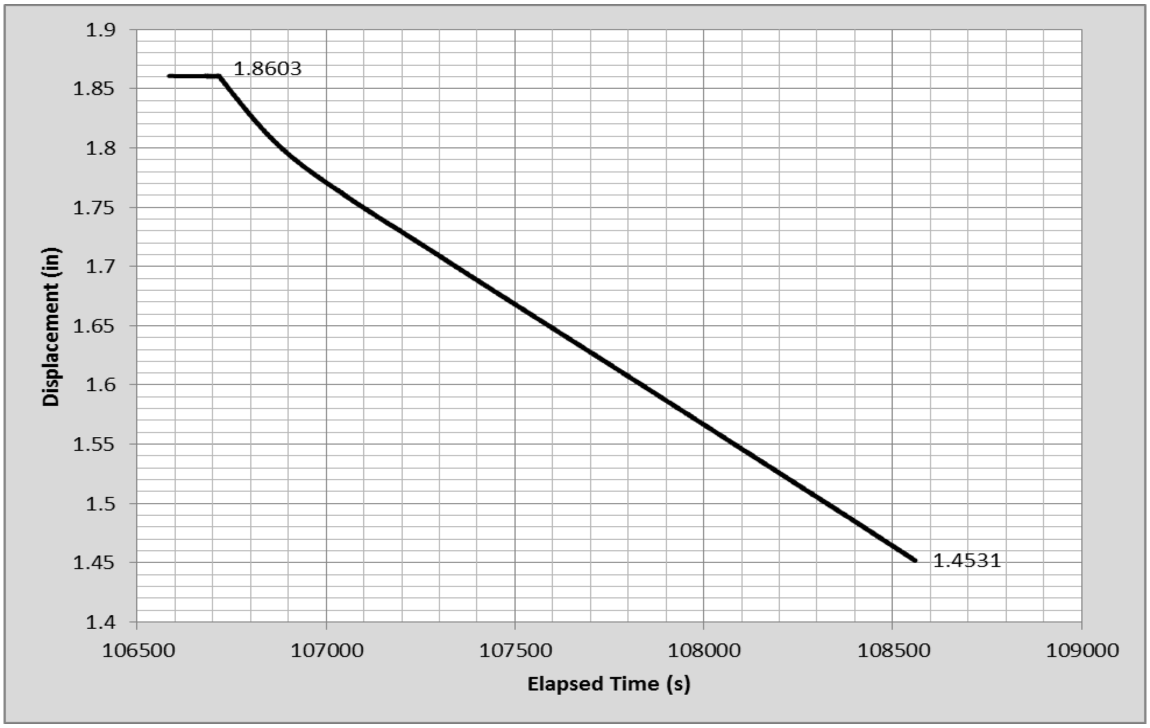

Figure C16: 15% Horizontal LVDT Displacement vs. Time

APPENDIX D

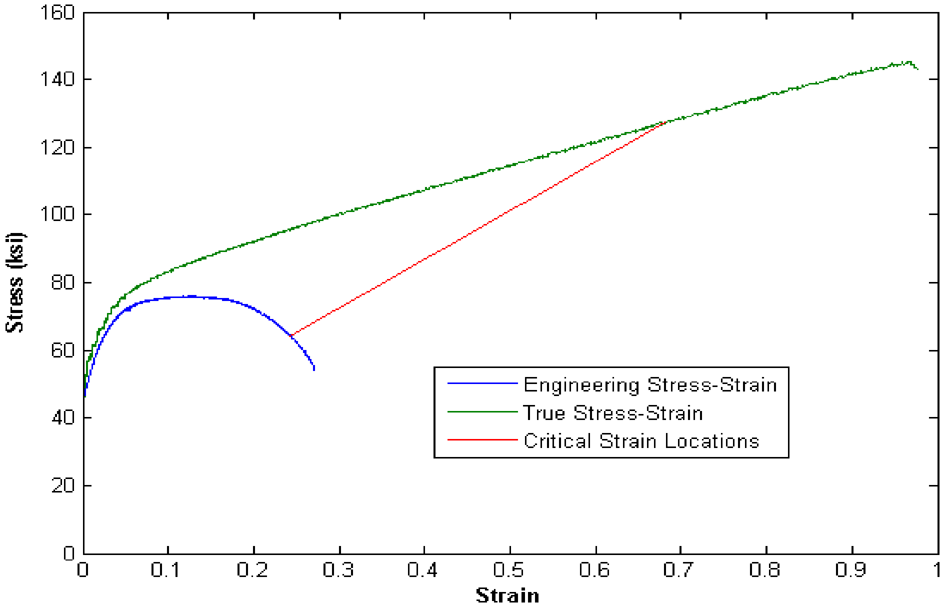

Figure D1: Critical Strain Results for Sample D1

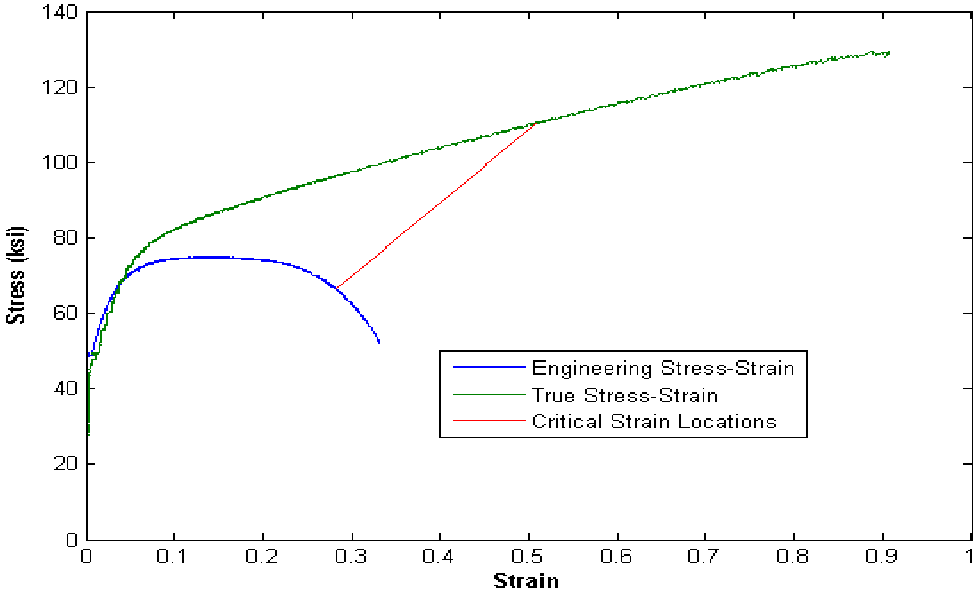

Figure D2: Critical Strain Results for Sample D2

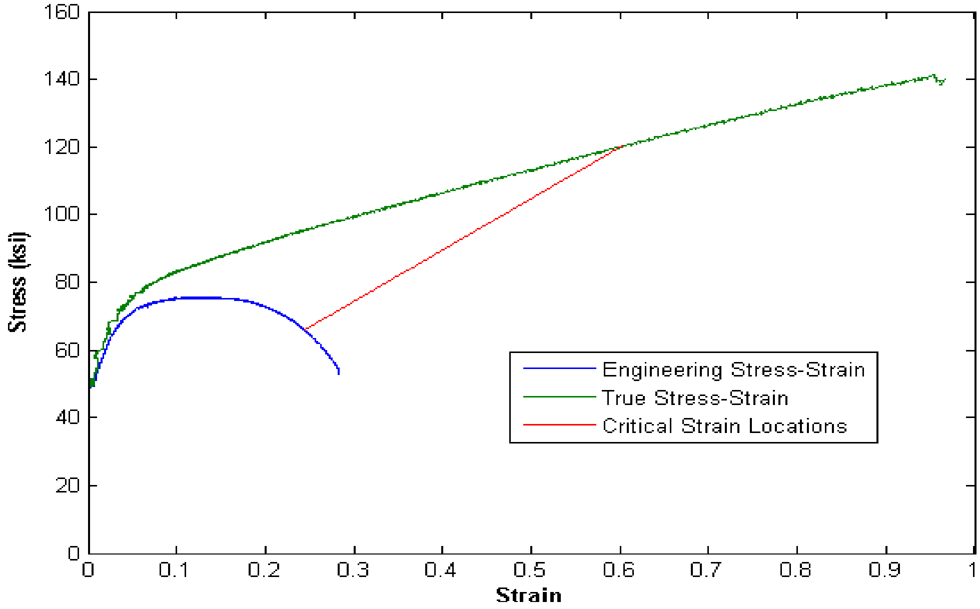

Figure D3: Critical Strain Results for Sample D3

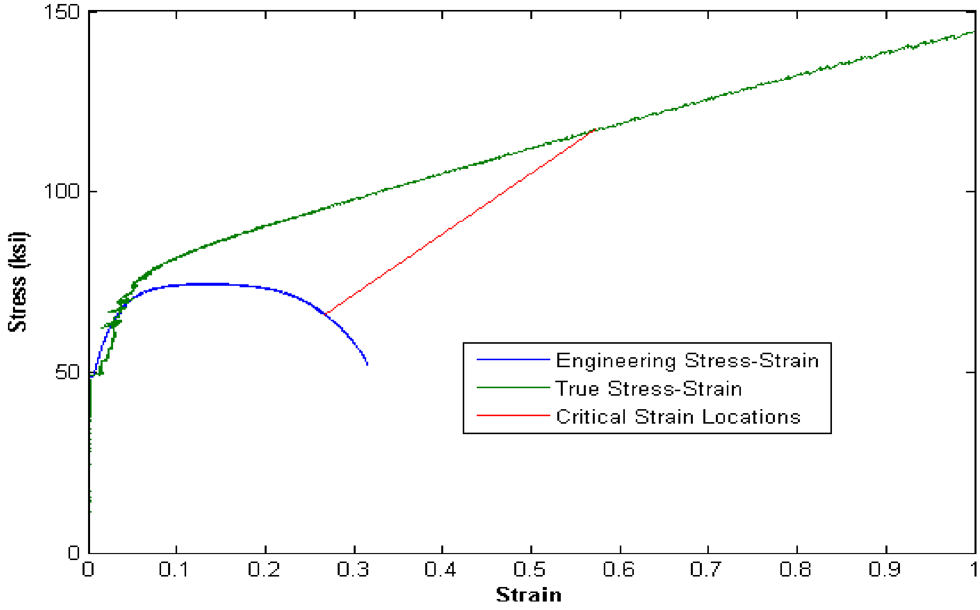

Figure D4: Critical Strain Results for Sample D4

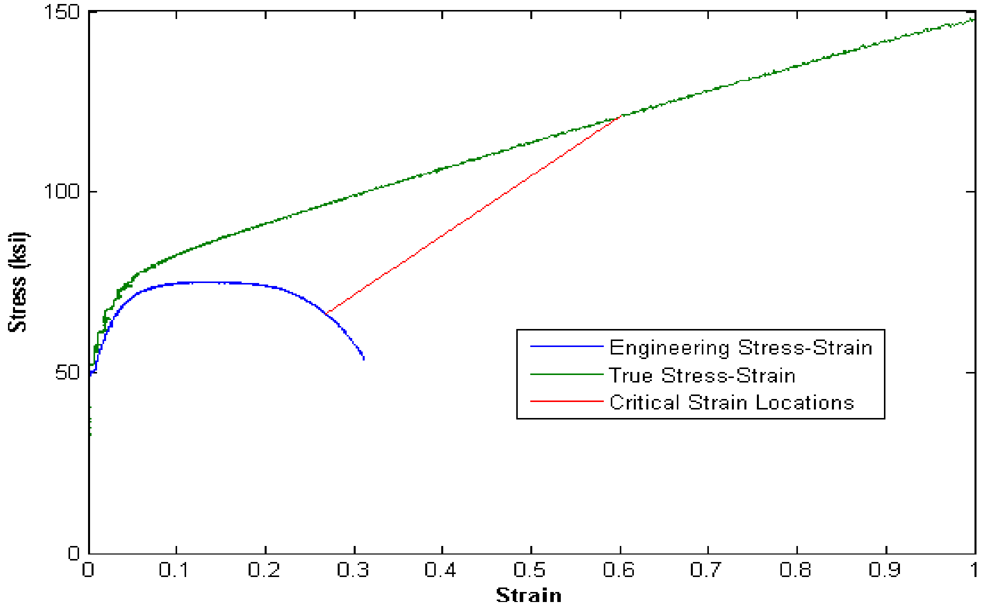

Figure D5: Critical Strain Results for Sample D5